Spring 2014

Modeling and Simulation of Shape Changes of Red Blood Cells in Shear Flow

John Gounley
Old Dominion University

Recommended Citation

Gounley, John. "Modeling and Simulation of Shape Changes of Red Blood Cells in Shear Flow" (2014). Doctor of Philosophy (PhD), dissertation, Mathematics and Statistics, Old Dominion University, DOI: 10.25777/frv3-m651
https://digitalcommons.odu.edu/mathstat_etds/16

MODELING AND SIMULATION OF SHAPE CHANGES OF RED BLOOD CELLS IN SHEAR FLOW

by

John Gounley
B.A. May 2008, Thomas Aquinas College
M.S. May 2011, Old Dominion University

A Dissertation Submitted to the Faculty of
Old Dominion University in Partial Fulfillment of the
Requirements for the Degree of

DOCTOR OF PHILOSOPHY

COMPUTATIONAL AND APPLIED MATHEMATICS

OLD DOMINION UNIVERSITY
May 2014

Approved by:

Yan Peng (Director)

Li-Shi Luo (Member)

Gordon Melrose (Member)

Shizhi Qian (Member)

Jin Wang (Member)

ABSTRACT

MODELING AND SIMULATION OF SHAPE CHANGES OF RED BLOOD CELLS IN SHEAR FLOW

John Gounley
Old Dominion University, 2014
Director: Dr. Yan Peng

A description of the biomechanical character of red blood cells is given, along with an introduction to current computational schemes which use deformable capsules to simulate red blood cell shape change. A comprehensive two- and three-dimensional framework for the fluid-structure interaction between a deformable capsule and an ambient flow is provided. This framework is based on the immersed boundary method, using lattice Boltzmann and finite element methods for the fluid and structure, respectively. The characteristic response and recovery times of viscoelastic circular and spherical capsules are compared, and their dependence on simulation parameters is shown. The shape recovery of biconcave capsules in two and three dimensions is also considered, focusing on the role of simulation parameters and steady-state behaviour in two dimensions, while studying the capsule characteristics which lead to shape recovery and shape memory in three dimensions. Finally, the notion of interpreting membrane viscosity as an additional fluid viscosity is studied and a computational scheme based on power law fluids is described.

ACKNOWLEDGMENTS

I'd like to thank my parents for their support, my advisor for her guidance, my committee for their time and expertise, and the Thomas Aquinas College community for teaching me how to think. I also owe particular debts of gratitude to Dr. Mark Dorrepaal, for bringing me to ODU; to Kristen, for teaching me coding; and to the other leaders of the Graduate Organization for Modeling, Analysis, and Simulation (GOMAS), for their efforts in a sometimes quixotic endeavour. Financial support from the ODU Modeling and Simulation Scholarship program is acknowledged.

Nomenclature

a	Equivalent radius of capsule
a_r, b_r, c_r	Coefficients of bilinear recovery time model
a_s, b_s, c_s	Coefficients of bilinear response time model
$\mathrm{a}_{\mathrm{vor}}$	Voronoi region
$\mathbf{c}$	Set of discrete velocities
c_0	Spontaneous curvature
Ca	Capillary number
$\mathbb{D}$	Rate of deformation tensor
$\mathrm{D}_{\mathrm{max}}$	Maximum value of D_{xy} during deformation
$\mathrm{D}_{\mathrm{min}}$	Minimum value of D_{xy} during recovery
$\mathrm{D}_{\mathrm{stop}}$	Value of D_{xy} when shear flow is stopped
D_{xy}	Taylor deformation parameter
dt	Time step
dx	Spatial step
E_B	Bending stiffness modulus
E_b	Bending stiffness ratio
E_m	Second shear elasticity modulus in SLS
E_s	Shear elasticity modulus
$\mathbb{F}$	Deformation gradient tensor
$\mathbf{f}$	Fluid probability distribution function
$\mathbf{f}_b$	Bending force density

$\mathbf{f}^{(\mathrm{eq})}$	Maxwellian equilibrium probability distribution function
$\mathbf{f}_{\mathrm{vol}}$	Volume penalty force
G	Ratio of shear elasticity moduli in SLS
$\mathbb{G}$	Right Cauchy-Green tensor
g_h	Smoothed delta function
H	Domain height in y-direction
h	Mesh unit
$H(d)$	Heaviside function of signed distance d
$\mathbf{j}$	Fluid momentum
K	Flow consistency index
k	Fluid shear rate
K_ν	Penalty coefficient for capsule volume
ℓ	Arc length
$\mathbf{M}$	Moment transformation matrix
$\mathbf{m}$	Velocity moments
$\mathbf{m}^{(\mathrm{eq})}$	Maxwellian equilibrium moments
$\hat{\mathbf{n}}$	Unit outward normal vector
N	Number of triangles in mesh
n	Flow behaviour index
N^i	Linear shape function
$\mathbf{P}$	Body forces on capsule
$\mathbf{p}$	Body force acting on fluid
$\mathbf{P}_{\mathrm{surf}}$	Matrix projecting to capsule surface plane

q	Transverse shear tension
Re	Reynolds number
$\mathbf{S}$	Relaxation parameter matrix
SLS	Standard linear solid viscoelastic model
$\hat{\mathbf{t}}$	Tangent vector
t_n	Time at n-th timestep
$\mathbf{U}$	Capsule velocity
$\mathbf{u}$	Fluid velocity
V	Fluid viscosity ratio
$V^\star$	Artificial fluid viscosity ratio
V_c	Capsule volume
V_{c0}	Initial capsule volume
W_b	Helfrich bending energy
W_{NH}	Neo-Hookean elastic energy
W_{SK}	Skalak elastic energy
$\mathbf{X}_c$	Position on Lagrangian capsule mesh
$\mathbf{x}_j$	Position on Eulerian fluid grid
α	Inclination angle of membrane element with respect to direction of flow
β	Phase angle
$\boldsymbol{\beta}_i$	Principal directions, $i = 1, 2$
η	Membrane viscosity ratio
Γ	Position of membrane element with respect to inclination angle of capsule
γ	Shear rate on capsule surface

κ	Curvature in two dimensions, mean curvature in three dimensions
κ_0	Initial curvature
κ_g	Gaussian curvature
λ	Membrane stretch ratio
λ_i	Principal stretches, $i = 1, 2$
Δ_{LB}	Laplace-Beltrami operator
μ	Fluid viscosity
μ_a	Ambient fluid viscosity
μ_c	Fluid viscosity inside capsule
μ_s	Membrane viscosity
μ_{mem}	Membrane viscosity in power law model
ν	Kinematic viscosity
$\boldsymbol{\sigma}$	Cauchy stress tensor
σ_i	Principal stresses, $i = 1, 2$
τ	In-plane tension
τ_e	Shear elastic timescale
τ_r	Recovery time
τ_s	Response time
τ_ν	Viscoelastic timescale
τ_{R1}	Initial recovery time
τ_{R2}	Latter recovery time
θ	Inclination angle of capsule with respect to direction of flow
ξ	Bulk viscosity

TABLE OF CONTENTS

LIST OF TABLES

LIST OF FIGURES

CHAPTER 1

INTRODUCTION

1.1 RED BLOOD CELLS

A red blood cell is an anucleate fluid-filled membrane, the cytoplasm of which contains an oxygen-transporting metalloprotein called hemoglobin. The membrane has two components: the cytoskeleton on the cytosolic (internal) side and a bilayer of lipid molecules on the external side [1]. The cytoskeleton is a protein network, a mesh of spectrin heterodimers bound to the membrane at the mesh nodes by various proteins. Lipids are fatty molecules which, having a hydrophilic head and hydrophobic tails, naturally form bilayers in fluids. The resulting bilayers are, effectively, two-dimensional fluids themselves, as the lipids readily exchange places with neighbors in their monolayer.

Red blood cells undergo substantial shape changes *in vivo*. The rest shape of a red blood cell is understood to be a biconcave discoid, with an approximately $8\mu m$ diameter and $2\mu m$ height [4]. However, the diameter of capillaries may be as small as $3-4\mu m$, passing through which requires the red blood cell to deform to a bullet-like shape [51]. These significant yet routine changes in shape are complicated by certain blood diseases, such as sickle cell anemia, in which a hemoglobin mutation stiffens red blood cell membranes, making them less able to deform and recover their shapes [10]. Better knowledge of the mechanics underlying red blood cell shape changes would be of use in understanding how they are distorted by sickle cell anemia and how this distortion might be countered by treatment [61]. Thus, an improved understanding of red blood cell deformation and recovery, and how different aspects of the cell effect these processes, is of interest.

The changes in shape during the circulation of blood are caused by the ambient fluid in blood, plasma, deforming the red blood cell. The other components of blood — white blood cells and platelets — account for less than 1% of blood volume and may be discounted for the sake of simplicity. The red blood cell membrane resists this deformation by the ambient fluid in several ways [4, 25]. First, the cytoskeleton acts like a lattice of springs, causing elastic resistance to shear deformation. Second, the bilayer resists the membrane being bent during deformation, displaying a quality denoted as bending stiffness. Third, the fluidic nature of the bilayer means that it resists frictional forces, as a viscous fluid; this property is referred to as membrane viscosity. Finally, both the cytoskeleton and bilayer have surface incompressibility, creating an isotropic elastic response to changes in surface area. Additionally, the hemoglobin inside the red blood cell adversely impacts deformation, as its viscosity (ca. 6 centipoise) is roughly five times that of plasma (ca. 1.2 centipoise). As a result, the shape changes of a red blood cell may be modeled as a fluid-structure interaction problem.

1.2 RED BLOOD CELL SHAPE

Despite red blood cell membranes being among the most studied biological membranes, two important, and related, properties of red blood cells remain without complete explanations. The first matter of uncertainty is the precise biomechanical source for the shape of mature red blood cells. While immature red blood cells, called reticulocytes, have a predictably spherical shape, mature red blood cells have a biconcave discoidal shape. From a biological perspective, a non-spherical shape is advantageous: the ratio of surface area to volume is higher and, consequently, facilitates the diffusion of oxygen across the red blood cell membrane. However, there is disagreement about whether the cytoskeleton, bilayer, or some combination of the two causes the biconcavity.

The second uncertainty is why red blood cells have shape memory. Discovered by the experiments of Fischer, shape memory means that, during recovery, an element of the membrane returns to the same (or opposite, homologous) position on the surface where it was located prior to deformation [25]. Whether shape memory is a trivial consequence of the red blood cell's biconcave shape, or a separate consideration, is unclear, since the antecedent is unresolved.

Experimental evidence inclining credence in both potential causes of biconcavity exists. Hereditary elliptocytosis, in which the cytoskeletal bonds are weakened, causes ellipsoidal red blood cells [38]. On the other hand, when the bilayer of (normal) red blood cells is removed, a spherical shape results [59]. Literature may be found which unequivocally declares one or the other to be the cause [1].

These questions are clarified by two terms from Fischer [25]: the reference shear deformation and reference curvature. To understand reference shear deformation, imagine increasing the volume of a red blood cell until it becomes spherical. Define the local shear deformation of each element of the cytoskeleton in that state to be the reference shear deformation of that element. If the reference shear deformation were uniformly zero over the entire cytoskeleton, then the cytoskeleton is unstressed in the spherical configuration and would not support shape memory. On the other hand, if the cytoskeleton were to support shape memory and be unstressed in the biconcave configuration, the reference shear deformation would be non-zero for (at least) some elements. The reference (or spontaneous) curvature describes the configuration in which the bilayer has a minimum amount of bending energy.

As Fischer notes, the fluidic, uniform nature of the bilayer is not consistent with a non-uniform reference curvature [25]. However, the bilayer does have an important internal/external phospholipid asymmetry, in terms of electrochemical potential [1], which could cause a constant non-zero reference curvature, as proposed by Helfrich [27, 47, 41]. On the other hand, there does not seem to be an *a priori* biomechanical restriction on the uniformity of the reference shear deformation.

If non-constant reference curvature were not possible, a red blood cell's hypothetically non-uniform reference shear deformation would seem to be the obvious cause of shape memory, as Fischer proposes. This non-uniform reference shear deformation may or may not also play a role in causing the biconcave shape. On the other hand, Pozrikidis has shown that a constant negative reference curvature is entirely consistent with, and perhaps even advantageous for, the biconcave shape [47]. This leads Pozrikidis to describe a comprehensive theory of the red blood cell's biconcave shape: the cytoskeleton is nearly unstressed and the biconcave shape is caused by constant negative reference curvature, the membrane's incompressibility, and the cell's volume deficiency.

1.3 MEMBRANE RESPONSE AND RECOVERY

Investigations into the shape recovery of red blood cells from deformation have largely followed experimental and theoretical avenues, as opposed to computational approaches. These studies primarily aimed at measuring the time course of shape recovery and determining the dominant mechanisms by which it occurred. Evans and Hochmuth, studying recovery from micropipette aspiration, argued that the recovery was dominated by the membrane's viscoelasticity, which they described using a Kelvin-Voigt model [21]. This model led them to characterize the recovery by an exponential decay function with relaxation time $\tau = \frac{2\mu_s}{E_s}$, in which μ_s is the membrane viscosity constant and E_s is the shear elasticity modulus [21]. Subsequent studies of red blood cell shape recovery from optical tweezing [13] and shear flow [7, 58] found similar results and employed the same model. Additionally, Sutera *et al.* suggested that the fluid viscosity ratio also influenced the shape recovery time [58]. On the other hand, Fischer's experiments of red blood cell shape recovery from tank-treading in shear flow suggest a time course of shape recovery that is $10-100$ times larger than these studies find, which might indicate the incompleteness of the Kelvin-Voigt model in describing recovery from shear flow [25].

However, recent work has challenged the applicability of Kelvin-Voigt and, perhaps, invalidated the results based on this model. Puig-de-Morales-Marinkovic *et al.*, studying the viscoelasticity of red blood cells using optical magnetic twisting cytometry (MTC), found that the dynamic response could not be explained by linear viscoelastic models [48]. Rather, they observed that the membrane displayed the viscous character of a power law fluid. Since then, power law responses have been noted by experimentalists using optical tweezing [66, 67], dynamic scattering microscopy [2], and diffraction phase microscopy [62]. As the bilayer consists of cholesterol, in addition to several types of lipids, it is perhaps not unreasonable that a collection of these diverse elements display non-Newtonian properties [1].

1.4 MEMBRANE VISCOSITY

Likewise, the viscoelasticity of red blood cells has presented one of the more challenging aspects of their modeling and simulation. Within the modeling paradigm and scale considered here, standard approaches exist for modeling the capsule's elasticity, bending stiffness, and fluid viscosity ratio. While neo-Hookean constitutive laws are adequate to describe the red blood cell's shear elasticity, Skalak has developed constitutive laws for biomechanics which integrate both shear and isotropic elasticity [23, 53]. Skalak laws have been clearly compared to their Hookean and neo-Hookean counterparts [5] and have been extensively implemented (e.g., [34, 36, 46, 64]). Similarly, Helfrich's model for the shape energy of fluid membranes has been the subject of considerable analysis [27, 41] and recent implementation [36, 64]. Finally, straightforward computational methods for smoothing the fluid viscosity ratio across the capsule interface have been developed, including solving a Poisson Equation across an index field [60] and using a smoothed Heaviside function [39, 68].

Models of membrane viscosity, however, are less settled. The pairing of the elastic cytoskeleton and viscous bilayer, subject to the same deformations, naturally suggests the Kelvin-Voigt viscoelastic model. Consequently, the vast majority of existing computational models implement Kelvin-Voigt [19, 35, 69]. More recently, Yazdani and Bagchi noted numerical instabilities when implementing Kelvin-Voigt, opting instead for the more versatile standard linear solid (SLS) model and adjusting its parameters so as to approximate Kelvin-Voigt [63]. Studies using stochastic mesoscopic methods have opted for other viscous models. For instance, Fedosov *et al.* developed a general dissipative model within the framework of dissipative particle dynamics (DPD) [24], while Noguchi and Gompper's multi-particle collision dynamics (MPCD) simulations of vesicles used bond-flipping for membrane viscosity [40]. Interestingly. Fedosov *et al.* simulated twisted torque cytometry with DPD [24] and their results agree well with Puig-de-Morales-Marinkovic *et al.* [48], though with a slightly larger power law exponent. There does not, however, appear to be a deterministic implementation of the power law proposed by experimentalists.

1.5 SCOPE & OUTLINE

This thesis has four principal aims. First, it will develop a comprehensive, extensible computational model of the fluid-structure interaction between plasma and a single red blood cell [46]. Second, it will show how the shape recovery of capsules differs from deformation, and quantify the role that the capsule's shape and parameters play in these processes. This will help to reconcile computational work, which has largely focused on deformation and dynamics, with experimental investigations, which generally considered shape recovery. Third, it will consider the potential mechanical causes of a red blood cells' biconcave shape and shape memory. Biological and theoretical studies have proposed several ideas, and the perspective of a computational study would be of interest. Fourth, in light of the recent maturation of membrane viscosity implementations, it will propose a new model for membrane viscosity, capable of describing its non-linear character. To achieve these aims, the following four chapters are organized as follows:

In Chapter 2, a complete methodology for modeling and simulation of the interaction between a fluid-filled capsule and an incompressible viscous fluid is presented in two and three dimensional settings. Based on lattice Boltzmann, immersed boundary, and finite element methods, the method is benchmarked against published results. Both the two and three dimensional versions of the structural model include the capsule's shear elasticity, bending stiffness, and membrane viscosity. Additionally, a method is presented for simulating different fluid viscosities inside and outside of the capsule.

In Chapter 3, circular and spherical capsules are placed in shear flow, deformed until reaching equilibrium, and recover their shapes after the shear flow is stopped. The response and recovery times of the capsules are measured using an exponential model and compared. The dependence of these characteristic times on various capsule parameters is considered. Additionally, differences between the two and three dimensional structural models are observed in this context.

In Chapter 4, the shape recovery of two dimensional biconcave capsules from shear flow is studied, with attention to the dependence on capsule parameters. The different courses of recovery for tank-treading and tumbling capsules are compared, and a general two-part recovery process is posited. Further, the shape recovery of a three dimensional biconcave capsule from shear flow is studied, for different preferred elastic and bending configurations. Particular attention is given to the possible mechanisms of the undeformed biconcave shape and of shape memory, in terms of the three dimensional model presented.

In Chapter 5, the idea of simulating membrane viscosity as a fluid viscosity is investigated. Considered in the context of a spherical capsule, a relationship between the effects of the fluid and membrane viscosity ratios is drawn. A proof-of-concept study is conducted, concluding that certain important aspects of shape change caused by membrane viscosity in a solid viscoelastic model may be adequately modeled using an artificial fluid viscosity ratio. The successful, albeit limited, results of this study are leveraged to posit a new model for simulating membrane viscosity as a power law fluid. A comparison of the deformation of a spherical capsule with a solid viscoelastic model and the power law fluid model is conducted, showing that the models differ little in shear flow.

CHAPTER 2

METHODOLOGIES

The general problem of a deformable fluid-filled capsule in an ambient flow requires a methodology for handling the fluid-structure interaction. Hou *et al.* divide existing fluid-structure interaction methodologies into two groups: monolithic and partitioned [29]. In the monolithic approach, a single algorithm is used to describe the fluid and structure. Conversely, partitioned methods use separate algorithms for the fluid and structure, along with an additional method to describe the interaction between them. A partitioned approach is selected for this model, configured around the immersed boundary method. Developed by Peskin for modeling blood flow in the heart, the immersed boundary method is based on transferring data between an Eulerian fluid domain and a Lagrangian structural mesh, using discrete delta functions [43]. A multiple-relaxation-time lattice Boltzmann method is employed to simulate the fluid flow, along with two and three dimensional finite element models to describe the capsule.

The case of a single capsule in simple shear flow is considered, with the Reynolds number $\mathrm{Re} = 0.05$. The Reynolds number is defined as $\mathrm{Re} = \frac{\rho k a}{\mu_a}$, in which ρ is the fluid density, k in the fluid shear rate, a is the equivalent radius of the capsule, and μ_a is the viscosity of the fluid surrounding the capsule. A capsule with equivalent radius a has, in two dimensions, the same area as a circular capsule with radius a. In three dimensions, a capsule with equivalent radius a has the same volume as a spherical capsule with radius a. The x-axis is the direction of flow, the y-axis is the direction of the velocity gradient, and (in three dimensional settings) the z-axis is the direction of undisturbed flow vorticity. The domain is theoretically infinite in the x- and z-directions. In the subsequent simulations, however, domains of $[0, 16a] \times [0, 12a]$ in two dimensions and $[0, 10a] \times [0, 10a] \times [0, 8a]$ in three dimensions are considered, in which a is the equivalent radius of the capsule. Previous analyses by Sui *et al.* [56] in two dimensions and Li and Sarkar [36] in three dimensions have shown these domains to be sufficient to avoid wall effects. The time step dt and spatial step dx are related as $h = dt = dx$, with h being set as 0.05 in two dimensions and 0.1 in three dimensions. Letting H be the size of the domain in the y-direction, the shear flow may be described in terms of shear rate k as

$$\mathbf{u} = \left[\left(y - \frac{1}{2}H\right)k, 0, 0\right]. \tag{1}$$

In all simulations, the center of capsule is centered in the domain, with respect to x-, y-, and z-axes.

2.1 LATTICE BOLTZMANN

In both the two and three dimensional models, a lattice Boltzmann method (LBM) is used to describe the fluid flow. Based on the Boltzmann Equation of statistical physics, lattice Boltzmann methods offer an alternative to traditional methods for solving the incompressible Navier-Stokes equations. Within the low Mach and Reynolds number region, LBM exhibits stability that exceeds many traditional methods [31]. Despite its statistical origins, LBM is fully deterministic, using the averaged behaviour of particles. The expression $f_i(\mathbf{x}_j, t_n)$ represents the distribution of particles at lattice node $\mathbf{x}_j$ with velocity $\mathbf{c}_i$ at time t_n. Particle velocities, like time and space, are discretized, so that a particle has one of a given finite set of velocities. In the two and three dimensional simulations, the D2Q9 and D3Q19 velocity models, respectively, are employed [31, 32]. The integers following 'D' and 'Q' denote the number of spatial dimensions and number of discrete velocities, respectively.

Using the multiple-relaxation-time approximation of the collision integral, the lattice Boltzmann Equation may be described as

$$\mathbf{f}(\mathbf{x}_j + \mathbf{c}d_t, t_n + d_t) - \mathbf{f}(\mathbf{x}_j, t_n) = -\mathbf{M}^{-1}\mathbf{S}[\mathbf{m}(\mathbf{x}_j, t_n) - \mathbf{m}^{(\mathrm{eq})}(\mathbf{x}_j, t_n)], \tag{2}$$

in which $\mathbf{f}$, $\mathbf{m}$, and $\mathbf{m}^{(\mathrm{eq})}$ represent vectors of Q-dimensions, the components of which are the distribution functions for each particle velocity $\mathbf{c}_i$, the velocity moments, and the Maxwellian equilibrium moments, respectively [18, 32].

The lattice Boltzmann method's time evolution thus consists of two steps: collision and streaming. With the MRT approximation, as represented on the right side of Equation (2), probabilities $\mathbf{f}$ at each lattice node $\mathbf{x}_j$ are mapped to their moment space by the matrix $\mathbf{M}$. Within this moment space, the non-conserved moments $\mathbf{m}(\mathbf{x}_j, t_n)$ relax toward their equilibria $\mathbf{m}^{(\mathrm{eq})}(\mathbf{x}_j, t_n)$, according to their specified relaxation parameters s_i on the diagonal of matrix $\mathbf{S}$. After this relaxation, the moments are mapped by the matrix $\mathbf{M}^{-1}$ back to probability space.

Following [18] and [31], the D2Q9 velocity discretization may be compactly formulated as

$$\mathbf{c}_i = \begin{cases} (0,0) & \text{for } i = 0 \\ (\cos[(i-1)\frac{\pi}{2}], \sin[(i-1)\frac{\pi}{2}]) & \text{for } i = 1:4 \\ (\cos[(2i-9)\frac{\pi}{4}], \sin[(2i-9)\frac{\pi}{4}])\sqrt{2} & \text{for } i = 5:8 \end{cases} \tag{3}$$

since the ratio $\frac{dx}{dt} = 1$. Likewise, the velocity discretization for D3Q19 is described as

$$\begin{bmatrix}\mathbf{c}_1 \cdots \mathbf{c}_{19}\end{bmatrix} = \tag{4}$$

$$\begin{bmatrix} 0 & 1 & -1 & 0 & 0 & 0 & 0 & 1 & 1 & -1 & -1 & 1 & -1 & 1 & -1 & 0 & 0 & 0 & 0 \\ 0 & 0 & 0 & 1 & -1 & 0 & 0 & 1 & -1 & 1 & -1 & 0 & 0 & 0 & 0 & 1 & 1 & -1 & -1 \\ 0 & 0 & 0 & 0 & 0 & 1 & -1 & 0 & 0 & 0 & 0 & 1 & 1 & -1 & -1 & 1 & -1 & 1 & -1 \end{bmatrix}$$

The Maxwellian equilibrium distribution is described in terms of the velocity discretization as

$$f_i^{eq} = \omega_i \rho \Big[1 + 3(\mathbf{c}_i \cdot \mathbf{u}) + \frac{9}{2}(\mathbf{c}_i \cdot \mathbf{u})^2 - \frac{3}{2}\mathbf{u}^2\Big] \tag{5}$$

for which the two dimensional weights are $\omega_0 = \frac{4}{9}$, $\omega_{1\cdots4} = \frac{1}{9}$, and $\omega_{5\cdots8} = \frac{1}{36}$. In three dimensions, the weights are $\omega_0 = \frac{1}{3}$, $\omega_{1\cdots6} = \frac{1}{18}$, and $\omega_{7\cdots18} = \frac{1}{36}$ [18, 31].

Unlike the Bhatnagar-Gross-Krook (BGK) approximation, in which all relaxation rates are the same, a multiple-relaxation-time scheme is optimized to ensure Galilean invariance and isotropy, while minimizing dissipation and dispersion. For D2Q9, the transformation matrix is

$$\mathbf{M} = \begin{bmatrix} 1 & 1 & 1 & 1 & 1 & 1 & 1 & 1 & 1 \\ -4 & -1 & -1 & -1 & -1 & 2 & 2 & 2 & 2 \\ 4 & -2 & -2 & -2 & -2 & 1 & 1 & 1 & 1 \\ 0 & 1 & 0 & -1 & 0 & 1 & -1 & -1 & 1 \\ 0 & -2 & 0 & 2 & 0 & 1 & -1 & -1 & 1 \\ 0 & 0 & 1 & 0 & -1 & 1 & 1 & -1 & -1 \\ 0 & 0 & -2 & 0 & 2 & 1 & 1 & -1 & -1 \\ 0 & 1 & -1 & 1 & -1 & 0 & 0 & 0 & 0 \\ 0 & 0 & 0 & 0 & 0 & 1 & -1 & 1 & -1 \end{bmatrix} \tag{6}$$

By Lallemand and Luo [31], the resulting moments are relaxed according to the relaxation parameters

$$\mathbf{S} = \begin{bmatrix} s_0 & s_1 & s_2 & s_3 & s_4 & s_5 & s_6 & s_7 & s_8 \end{bmatrix} \tag{7}$$

Parameters s_0, s_3, and s_5 are not relevant to the model, since they describe conserved moments (density ρ and momenta j_x and j_y). The kinematic viscosity ν is related to the relaxation parameters $s_7 = s_8$ for components of the pressure tensor p_{xx} and p_{xy} as

$$\nu = \frac{1}{3}\Big(\frac{1}{s_7} - \frac{1}{2}\Big). \tag{8}$$

Additionally, the parameters $s_4 = s_6$ for energy flux components q_x and q_y are related to the viscosity as

$$s_4 = 3\frac{2 - s_8}{3 - s_8}. \tag{9}$$

The bulk viscosity ξ is related to the relaxation parameter s_1 for energy e as

$$\xi = \frac{1}{6}\Big(\frac{1}{s_1} - \frac{1}{2}\Big). \tag{10}$$

Finally, the moment ϵ related to the energy square, which is relaxed by s_2, only alters the higher-order hydrodynamic terms in D2Q9; consequently, let $s_2 = 1.64$.

For D3Q19, according to [18] and [32], the transformation matrix is defined as

$$\mathbf{M} = \begin{bmatrix}
1 & 1 & 1 & 1 & 1 & 1 & 1 & 1 & 1 & 1 & 1 & 1 & 1 & 1 & 1 & 1 & 1 & 1 & 1 \\
-30 & -11 & -11 & -11 & -11 & -11 & -11 & 8 & 8 & 8 & 8 & 8 & 8 & 8 & 8 & 8 & 8 & 8 & 8 \\
12 & -4 & -4 & -4 & -4 & -4 & -4 & 1 & 1 & 1 & 1 & 1 & 1 & 1 & 1 & 1 & 1 & 1 & 1 \\
0 & 1 & -1 & 0 & 0 & 0 & 0 & 1 & -1 & 1 & -1 & 1 & -1 & 1 & -1 & 0 & 0 & 0 & 0 \\
0 & -4 & 4 & 0 & 0 & 0 & 0 & 1 & -1 & 1 & -1 & 1 & -1 & 1 & -1 & 0 & 0 & 0 & 0 \\
0 & 0 & 0 & 1 & -1 & 0 & 0 & 1 & 1 & -1 & -1 & 0 & 0 & 0 & 0 & 1 & -1 & 1 & -1 \\
0 & 0 & 0 & -4 & 4 & 0 & 0 & 1 & 1 & -1 & -1 & 0 & 0 & 0 & 0 & 1 & -1 & 1 & -1 \\
0 & 0 & 0 & 0 & 0 & 1 & -1 & 0 & 0 & 0 & 0 & 1 & 1 & -1 & -1 & 1 & 1 & -1 & -1 \\
0 & 0 & 0 & 0 & 0 & -4 & 4 & 0 & 0 & 0 & 0 & 1 & 1 & -1 & -1 & 1 & 1 & -1 & -1 \\
0 & 2 & 2 & -1 & -1 & -1 & -1 & 1 & 1 & 1 & 1 & 1 & 1 & 1 & 1 & -2 & -2 & -2 & -2 \\
0 & -4 & -4 & 2 & 2 & 2 & 2 & 1 & 1 & 1 & 1 & 1 & 1 & 1 & 1 & -2 & -2 & -2 & -2 \\
0 & 0 & 0 & 1 & 1 & -1 & -1 & 1 & 1 & 1 & 1 & -1 & -1 & -1 & -1 & 0 & 0 & 0 & 0 \\
0 & 0 & 0 & -2 & -2 & 2 & 2 & 1 & 1 & 1 & 1 & -1 & -1 & -1 & -1 & 0 & 0 & 0 & 0 \\
0 & 0 & 0 & 0 & 0 & 0 & 0 & 1 & -1 & -1 & 1 & 0 & 0 & 0 & 0 & 0 & 0 & 0 & 0 \\
0 & 0 & 0 & 0 & 0 & 0 & 0 & 0 & 0 & 0 & 0 & 0 & 0 & 0 & 0 & 1 & -1 & -1 & 1 \\
0 & 0 & 0 & 0 & 0 & 0 & 0 & 0 & 0 & 0 & 0 & 1 & -1 & -1 & 1 & 0 & 0 & 0 & 0 \\
0 & 0 & 0 & 0 & 0 & 0 & 0 & 1 & -1 & 1 & -1 & -1 & 1 & -1 & 1 & 0 & 0 & 0 & 0 \\
0 & 0 & 0 & 0 & 0 & 0 & 0 & -1 & -1 & 1 & 1 & 0 & 0 & 0 & 0 & 1 & -1 & 1 & -1 \\
0 & 0 & 0 & 0 & 0 & 0 & 0 & 0 & 0 & 0 & 0 & 1 & 1 & -1 & -1 & -1 & -1 & 1 & 1
\end{bmatrix} \tag{11}$$

The diagonal matrix of relaxation parameters is

(12)

$$\mathbf{S} = \begin{bmatrix} s_0 & s_1 & s_2 & s_3 & s_4 & s_5 & s_6 & s_7 & s_8 & s_9 & s_{10} & s_{11} & s_{12} & s_{13} & s_{14} & s_{15} & s_{16} & s_{17} & s_{18} \end{bmatrix}$$

The conserved density ρ and momenta j_x, j_y, and j_z are related to s_0, s_3, s_5, and s_7, the choices of which do not alter the model. The kinematic viscosity ν is related to the relaxation parameters $s_9 = s_{11} = s_{13} = s_{14} = s_{15}$ for components of the pressure tensor $3p_{xx}$, p_{ww}, p_{xy}, p_{yz}, and p_{yz} by the equation

$$\nu = \frac{1}{3}\left(\frac{1}{s_9} - \frac{1}{2}\right) \tag{13}$$

Similarly, the bulk viscosity ξ is related to the relaxation parameter s_1 for energy e by

$$\xi = \frac{2}{9}\left(\frac{1}{s_1} - \frac{1}{2}\right). \tag{14}$$

The relaxation parameters s_4, s_6, and s_8 for mass fluxes q_x, q_y, and q_z must be identical for the sake of isotropy; they are set equal to s_9. The remaining parameters s_2 for energy square ϵ, s_{10} and s_{12} for $3\pi_{xx}$ and π_{ww}, and s_{16}, s_{17}, and s_{18} relating to m_x, m_y, and m_z are higher-order terms which do not alter the hydrodynamics. Consequently, these remaining parameters are set equal to 1.8.

2.2 FLUID VISCOSITY

The dimensionless fluid viscosity ratio V of a capsule is defined to be the ratio of the fluid viscosity inside the capsule. μ_c, to the ambient fluid viscosity μ_a. To implement a non-unity fluid viscosity ratio over a time-dependent region, the fluid viscosity at each node must be computed every timestep, so that the relaxation parameters for that node may be appropriately adjusted. In practice, this is only necessary for nodes which are near the capsule boundary, as the others will not change from one timestep to the next. To compute the new viscosity at a node, not only whether the node lies inside or outside of the capsule must be determined, but the fluid viscosity contrast across the capsule interface must also be smoothed, for the sake of the stability of the fluid solver. In the context of multiphase flows, Tryggvason *et al.* used a Poisson Equation to determine fluid density at grid points near the interface [60]. Alternatively, N'Dri *et al.* employed and Zhang *et al.* refined a method using a Heaviside function and based on the shortest normal distance from the fluid node to the membrane [39, 68]. For this consideration, the approach of Zhang *et al.* is adopted.

To determine the viscosity of a fluid node at a given timestep, the Lagrangian node nearest to the fluid node is selected. The dot product of the vector between these two nodes and the unit outward normal from the Lagrangian node is calculated. The sign of this dot product produces a reliable indication of whether the fluid node under consideration is inside or outside of the capsule. Next, the shortest (normal) distance d from the fluid node to the capsule boundary is approximated. The sign of d for a fluid node is set to be positive if located outside of the capsule, or negative if inside of the capsule.

With the signed distance d having been determined, a smoothed Heaviside function of d from [68] is defined, as

$$H(d) = \begin{cases} 0 & d < -2h; \\ \frac{1}{2}(1 + \frac{d}{2h} + \frac{1}{\pi}\sin\frac{\pi d}{2h}) & -2h \leq d \leq 2h; \\ 1 & d > 2h. \end{cases} \tag{15}$$

Finally, the viscosity μ at the node is determined using $H(d)$, by the equation

$$\mu(\mathbf{x}) = \mu_c + (\mu_a - \mu_c)H[d(\mathbf{x})]. \tag{16}$$

in terms of viscosity μ_c inside the capsule and ambient viscosity μ_a.

2.3 IMMERSED BOUNDARY

In the immersed boundary method, the fluid is simulated across the entire simulation domain and the structural mesh moves without altering the Eulerian mesh. The fluid velocity near the capsule boundary is used to determine the velocity of the capsule; the capsule's velocity may then be used to update the position of the capsule. The fluid-structure interaction requires that a no-slip condition be maintained at the capsule boundary [29], which deforms the capsule and leads to body forces. The incompressible Navier-Stokes Equations are solved, using LBM, with the addition of these forces to determine the fluid velocity.

A smoothed Dirac delta function is used to transfer the necessary data between the two grids. The smoothed Dirac delta function in d-dimensional space is defined by

$$\delta_h(\mathbf{x}) = \delta_h(x_1)\delta_h(x_2)\cdots\delta_h(x_d), \mathbf{x} \in R^d \tag{17}$$

in which the one dimensional discrete delta function is given as

$$\delta_h(x) = \begin{cases} \frac{1}{4h}\left[1+\cos(\frac{\pi x}{2h})\right] & |x| \leq 2h \\ 0 & |x| > 2h \end{cases} \tag{18}$$

The smoothed delta function is employed to determine the fluid velocity at capsule gridpoints, based on the local fluid velocity, and to spread the body forces created by capsule deformation to the nearby fluid. The capsule velocity $\mathbf{U}$ is determined at Lagrangian node $\mathbf{X}_c$ by

$$\mathbf{U}(\mathbf{X}_c) = \sum_j \delta(\mathbf{X}_c - \mathbf{x}_j)\mathbf{u}(\mathbf{x}_j)h^d \tag{19}$$

in which $\mathbf{x}_j$ and $\mathbf{u}$ denote Eulerian fluid node position and velocity, respectively. Subsequently, this velocity is used to update the position of the Lagrangian grid by the forward Euler method:

$$\mathbf{X}_c(t_n + dt) = \mathbf{X}_c(t_n) + \mathbf{U}(\mathbf{X}_c)dt \tag{20}$$

Similarly, body forces $\mathbf{P}$ at $\mathbf{X}_c$, which result from the deformation of the capsule, are distributed to the fluid grid points by

$$\mathbf{p}(\mathbf{x}_j) = \sum_c \delta(\mathbf{X_c} - \mathbf{x}_j)\mathbf{P}(\mathbf{X}_c), \tag{21}$$

as the area of the elements has already been incorporated into calculation of $\mathbf{P}$ at $\mathbf{X}_c$. Subsequently, the forces exerted on the fluid are incorporated into the fluid simulation according to the update method described in [33] and [42]. In the collision phase of LBM, after computing the hydrodynamic moments, momenta $\mathbf{j} = \left(j_x,\ j_y,\ j_z\right)$ at gridpoint $\mathbf{x}_j$ are updated to according to the forces $\mathbf{p}$, as

$$\mathbf{j}'(\mathbf{x}_j) = \mathbf{j}(\mathbf{x}_j) + \frac{dt}{2}\mathbf{p}(\mathbf{x}_j). \tag{22}$$

After using $\mathbf{j}'$ to find the equilibrium moments $\mathbf{m}^{(\mathrm{eq})}$, the momentum is updated again, as

$$\mathbf{j}''(\mathbf{x}_j) = \mathbf{j}'(\mathbf{x}_j) + \frac{dt}{2}\mathbf{p}(\mathbf{x}_j) \tag{23}$$

and $\mathbf{j}''$ is used to compute the probability distribution after the collision phase. The advection step of LBM is not altered by the addition of forces acting on the fluid.

2.4 TWO DIMENSIONAL STRUCTURAL ALGORITHM

In two dimensional simulations, capsules which are either initially circular or biconcave are considered. Each capsule is discretized into 140 line segments, which are initially equally-sized. The configuration of the biconcave capsule in the xy-plane is described by

$$x = a\alpha \sin\chi \tag{24}$$

$$y = a\frac{\alpha}{2}(0.207 + 2.003\sin^2\chi - 1.123\sin^4\chi)\cos\chi \tag{25}$$

for cell radius ratio $\alpha = 1.39$, equivalent radius $a = 0.5$, characteristic length $1.48a$, and angle χ ranging from -0.5π to 1.5π [56]. The biconcave capsule is also inclined by a 45° angle to the positive x-axis.

2.4.1 METHODOLOGY

The capsule is assumed to be massless and initially unstressed. Due to this algorithm's use of the immersed boundary method, velocity is continuous across the membrane. However, a jump in interfacial tension across the interface does exist. Consequently, using Gauss' divergence theorem, Pozrikidis [45] derives the force equilibrium Equation for complete tension $\mathbf{T} = \tau\hat{\mathbf{t}} + q\hat{\mathbf{n}}$ as

$$\mathbf{f} = -(\mathbf{P}_{\text{surf}}\cdot\nabla)\cdot(\tau\hat{\mathbf{t}} + q\hat{\mathbf{n}}) \tag{26}$$

for in-plane tension τ, transverse shear tension q, tanget vector $\hat{\mathbf{t}}$, and outward normal vector $\hat{\mathbf{n}}$. The projection matrix $\mathbf{P}_{\text{surf}} = \mathbf{I} - \mathbf{nn}$ projects the gradient to the capsule surface, so that $\mathbf{P}_{\text{surf}}\cdot\nabla$ is the surface gradient. In two dimensions, the Equation may be simplified by the Frenet-Serret formulae to

$$\mathbf{f} = -\frac{\partial}{\partial\ell}(\tau\hat{\mathbf{t}} + q\hat{\mathbf{n}}) = \left[\kappa\tau - \frac{\partial q}{\partial\ell}\right]\hat{\mathbf{n}} - \left[\frac{\partial\tau}{\partial\ell} + \kappa q\right]\hat{\mathbf{t}} \tag{27}$$

for capsule curvature κ and derivatives taken with respect to capsule arc length ℓ. Further, the transverse shear tension q is simply the derivative of bending moment m with respect to arc length, as $q = \frac{\partial m}{\partial\ell}$. The necessary first and second derivatives with respect to arc length are performed with five-point centered difference methods for arbitrarily spaced abcissae.

The viscoelastic character of the capsule membrane is described using the Kelvin-Voigt viscoelastic model, with a viscous dashpot in parallel with an elastic spring (see

Figure 4). For Kelvin-Voigt, in-plane tension is simply the sum of the elastic and viscous contributions, as

$$\tau = \tau_e + \tau_\nu. \tag{28}$$

Strain for each element of the capsule is given in terms of the stretch ratio λ, which is defined by the ratio of a line element's current length ℓ and initial length ℓ_0, as

$$\lambda(t) = \frac{\ell(t)}{\ell_0}. \tag{29}$$

For the sake of simplicity, Hooke's law is employed to describe the capsule's shear elasticity and determine the elastic tension τ_e. This model takes the form

$$\tau_e = E_s(\lambda - 1), \tag{30}$$

in which E_s is the shear elasticity modulus [56]. The tension due to membrane viscosity is defined by

$$\tau_\nu = \mu_s \frac{1}{\lambda}\frac{\partial \lambda}{\partial t}, \tag{31}$$

in which μ_s is the membrane viscosity coefficient [69]. The time derivative of λ is calculated by a one-sided second order finite difference method. The capsule's isotropic elasticity is not explicitly included in the two dimensional algorithm. Transverse shear tension is the result of bending stiffness and defined as

$$q = \frac{\partial m}{\partial \ell} = E_B \frac{\partial}{\partial \ell}(\kappa - \kappa_0), \tag{32}$$

in which E_B is the bending stiffness modulus, κ is the curvature, and κ_0 is the preferred curvature [46, 56]. As noted by Pozrikidis, Equation (32) is, strictly speaking, only correct for small deviations from the preferred curvature, but is sufficient to account for the qualitative role of bending stiffness here [46]. For both circular and biconcave capsules, κ_0 is set equal to the initial curvature. Curvature κ is calculated with periodic cubic spline interpolation; if the capsule surface is defined by the function $\sigma = F(x)$, then

$$\kappa = \frac{\pm F''}{(1 + F'^2)^{3/2}}. \tag{33}$$

Thus, the two dimensional capsule is unstressed, by either viscoelastic tension or bending moments, at the initial shape configuration.

Three structural non-dimensional parameters may now be defined, in addition to the aforementioned non-dimensional fluid viscosity ratio V. The capillary number Ca is defined as

$$\text{Ca} = \frac{\mu_a k a}{E_s} \tag{34}$$

in terms of ambient fluid viscosity μ_a, shear rate k, equivalent capsule radius a, and shear elasticity modulus E_s. The capillary number Ca represents the ratio of viscous fluid shear to solid elastic force, and is also referred to as the dimensionless shear rate in the literature. The bending stiffness E_b is defined as

$$E_b = \frac{E_B}{aE_s} \tag{35}$$

for bending stiffness modulus E_B and represents the ratio of bending to shear resistance. Finally, the membrane viscosity ratio η is defined as

$$\eta = \frac{\mu_s}{a\mu_a} \tag{36}$$

for membrane viscosity coefficient μ_s and equivalent radius a; thus, η is the ratio of membrane to ambient fluid viscosity.

2.4.2 VALIDATION

The standard parameter for describing the deformation of a capsule is the Taylor deformation parameter,

$$D_{xy} = \frac{L - W}{L + W}. \tag{37}$$

In two dimension simulations, L and W are defined to be the capsule length and width, respectively. Due to the discrete nature of the capsule model from which L and W are measured, graphs of D_{xy} in two dimensions are not perfectly smooth, but this does not reflect a corresponding lack of smoothness in the capsule geometry. In three dimensions, however, L and W are defined to be the major and minor axes of an ellipsoid in the xy-plane with the same moment of inertia as the capsule, as stated by Clausen and Aidun [12]. The formula for the moment of inertia is

$$I_{ij} = \int_V \Big(r_k r_k \delta_{ij} - r_i r_j\Big) dV = \frac{1}{5}\int_A \Big(r_l r_l r_k n_k \delta_{ij} - r_i r_j r_k n_k\Big) dA, \tag{38}$$

in terms of node position vector $\mathbf{r}$ and unit outward normal $\hat{\mathbf{n}}$. From the eigenvalues of the moment of inertia matrix, the ellipsoid's major and minor axes may be calculated.

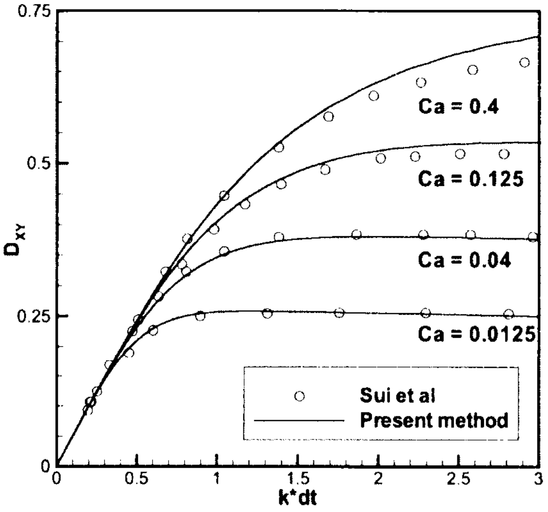

Figure 1. Comparison with Sui *et al.* for shear elasticity. Ca varies for $E_b = 0$, for $V = 1$ and $\eta = 0$.

In all subsequent results, shape deformation and recovery will be quantified in terms of D_{xy}.

The results from the two dimensional algorithm are compared with a similar approach by Sui *et al.*, in which immersed boundary and BGK lattice Boltzmann methods were used [56]. Figure 1 considers the deformation of an elastic capsule, with respect to the Taylor deformation parameter, for different capillary numbers Ca. The results agree well, though this approach overshoots the equilibrium value somewhat for Ca = 0.4. This difference may be the result of the very fine multiblock fluid grid used in the neighborhood of the capsule in [56]. Similarly acceptable agreement is observed in Figure 2 for different values of the bending stiffness E_b. Once again, slight deviations in the equilibrium values are observed, which are acceptable in light of the coarser grid here. Similar comparisons for fluid and membrane viscosity ratios are omitted, due to a lack of published data.

2.5 THREE DIMENSIONAL STRUCTURAL ALGORITHM

The three dimensional capsule surface is discretized into triangular elements.

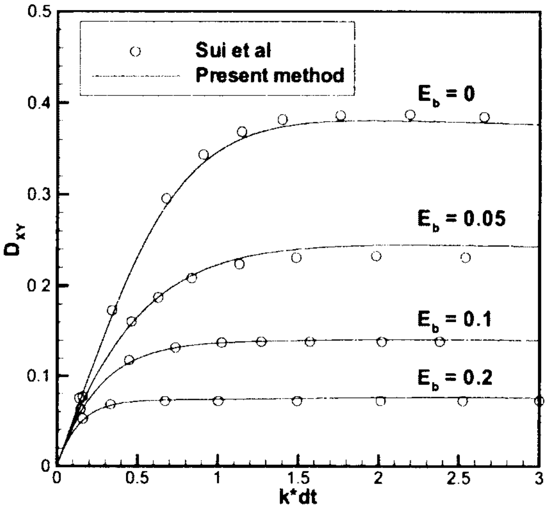

Figure 2. Comparison with Sui *et al.* for bending stiffness. E_b varies for Ca = 0.04, for $V = 1$ and $\eta = 0$.

Meshes for spherical and biconcave capsules are produced by generating an icosahedron. Using the approach of Ramanujan and Pozrikidis for an octahedron, each edge of the icosahedron is bisected and these points are used to split each face of the icosahedron into four equal triangles [49]. This process is repeated until the mesh is sufficiently fine. A mesh with 2562 vertices and 5120 triangles results is considered sufficient, based on the fluid grid and Yazdani's convergence analysis [65]. Then, each triangle in the mesh is projected onto a circle or biconcave capsule. Spherical capsules have a radius $a = 1$. The shape of the biconcave capsule is given by the definition

$$x = a\alpha \sin\chi \cos\phi \tag{39}$$

$$y = \frac{a\alpha}{2}(0.207 + 2.003\sin^2\chi - 1.123\sin^4\chi)\cos\chi \tag{40}$$

$$z = a\alpha \sin\chi \sin\phi \tag{41}$$

for equivalent radius $a = 1$, $\alpha = 1.3858$, and angles χ, ϕ from 0 to 2π [46]. Additionally, the resulting biconcave capsule is inclined at a 45° angle with respect to the horizontal in the xy-plane.

2.5.1 CAPSULE MODEL

The capsule's elastic character is described by a finite element model. The capsule itself is considered to be massless and composed of a network of zero-thickness triangles, surrounding the interior fluid. By comparing a given triangle to its initial (undeformed) configuration, the strains and corresponding stress resultants on each triangle may be computed. However, a deformed triangle is often no longer in the plane of the undeformed triangle. While this rotation does not contribute to the stress on the element, it does complicate the comparison between deformed and undeformed triangles. Consequently, for the purpose of calculating strains, the approach of Charrier *et al.* is adopted [9, 52], mapping the undeformed and deformed triangular elements to the common $z = 0$ plane. Figure 3 shows the result of this mapping for undeformed triangle $\mathbf{x}_i\mathbf{x}_j\mathbf{x}_k$ and deformed triangle $\mathbf{X}_i\mathbf{X}_j\mathbf{X}_k$. In this way, triangle deformation has been reduced to plane stretching and the displacement vector $\mathbf{u} = \mathbf{X} - \mathbf{x}$ and the deformation gradient matrix $F_{ij} = \frac{\partial X_i}{\partial x_j} = \delta_{ij} + \frac{\partial u_i}{\partial x_j}$, for $i, j = 1, 2$, may be calculated.

In the absence of body forces and acceleration, the principle of virtual work is

$$\int_V \Big(\frac{\partial \sigma_{ij}}{\partial X_i}\Big)\delta u_j dV = 0 \tag{42}$$

in terms of Cauchy stress tensor components σ_{ij} and virtual displacements δu_j, being integrated over volume V. While the determination of the stress tensor for elastic and viscoelastic membranes will be discussed in the two subsequent sections, the derivation of the finite element model is presented here. Since

$$\frac{\partial}{\partial X_i}\Big(\sigma_{ij}\delta u_j\Big) = \Big(\frac{\partial}{\partial X_i}\sigma_{ij}\Big)\delta u_j + \sigma_{ij}\frac{\partial}{\partial X_i}\Big(\delta u_j\Big), \tag{43}$$

the principle may be written as

$$\int_V \frac{\partial}{\partial X_i}\Big(\sigma_{ij}\delta u_j\Big)dV = \int_V \sigma_{ij}\frac{\partial}{\partial X_i}\Big(\delta u_j\Big)dV. \tag{44}$$

Replacing $\frac{\partial \delta u_j}{\partial X_i} = \frac{\partial \delta u_j}{\partial x_k}\frac{\partial x_k}{\partial X_i} = \frac{\partial \delta u_j}{\partial x_k}F_{ki}^{-1}$ on the right side of Equation (44) and using the divergence theorem on its left side, this may be written as

$$\int_A n_i \sigma_{ij}\delta u_j dA = \int_V \sigma_{ij}\frac{\partial \delta u_j}{\partial x_k}F_{ki}^{-1}dV \tag{45}$$

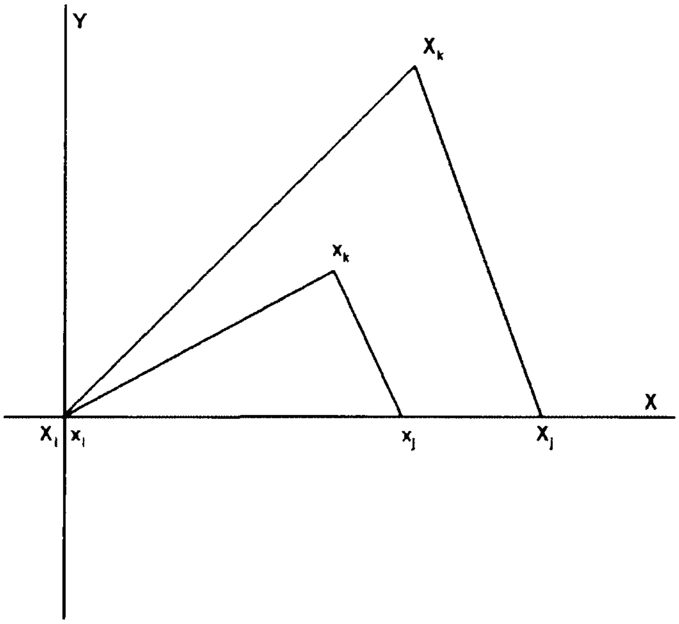

Figure 3. Undeformed triangle $\mathbf{x}_i\mathbf{x}_j\mathbf{x}_k$ and deformed triangle $\mathbf{X}_i\mathbf{X}_j\mathbf{X}_k$. For the sake of simplicity, x_i and X_i are mapped to the origin, while the edges x_ix_j and X_iX_j are mapped to the x-axis.

for components n_i of the outward normal vector. Expanding arbitrary displacements δu_j in terms of linear shape function N^l, as $\delta u_j = N^l \delta u_j^l$, the result is

$$\int_A n_i \sigma_{ij} N^l \delta u_j^l dA = \int_V \sigma_{ij} \delta u_j^l \frac{\partial N^l}{\partial x_k} F_{ki}^{-1} dV. \tag{46}$$

Contracting the surface traction force $P_j^l = \int_A n_i \sigma_{ij} N^l dA$, the Equation simplifies to

$$P_j^l \delta u_j^l = \int_V \delta u_j^l \frac{\partial N^l}{\partial x_k} F_{ki}^{-1} \sigma_{ij} dV. \tag{47}$$

Assuming linearity of the linear shape function over the triangle, this simplifies to

$$P_j^l \delta u_j^l = \delta u_j^l \frac{\partial N^l}{\partial x_k} F_{ki}^{-1} \sigma_{ij} V. \tag{48}$$

Since displacement δu_j^l is arbitrary, one may reduce and transpose:

$$P_j^l = \sigma_{ji} F_{ik}^{-1} \frac{\partial N^i}{\partial x_k} V. \tag{49}$$

The linear shape functions N^l and their coefficients are defined as

$$a_i = y_j - y_k \tag{50}$$

$$b_i = x_k - x_j \tag{51}$$

$$c_i = x_j y_k - x_k y_j \tag{52}$$

$$2A_0 = a_i x_i + b_i y_i + c_i \tag{53}$$

$$N^i = \frac{a_i x + b_i y + c_i}{2A_0} \tag{54}$$

and N^j and N^k are derived by cycling $i \to j \to k \to i$ [52]. As a result, Equation (49) may be more clearly expressed as

$$\begin{bmatrix} P_{xi} & P_{xj} & P_{xk} \\ P_{yi} & P_{yj} & P_{yk} \end{bmatrix} = \frac{V}{2A_0} \boldsymbol{\sigma}\, \mathbb{F}^{-T} \begin{bmatrix} a_i & a_j & a_k \\ b_i & b_j & b_k \end{bmatrix} = \frac{\lambda_1\lambda_2}{2} \boldsymbol{\sigma}\, \mathbb{F}^{-T} \begin{bmatrix} a_i & a_j & a_k \\ b_i & b_j & b_k \end{bmatrix} \tag{55}$$

in which P_{xi} represents the force in the x-direction at vertex i of the triangle, $\boldsymbol{\sigma}$ is the Cauchy stress tensor, and $\mathbb{F}$ is the deformation gradient tensor. The element volume V is related to the undeformed area A_0 of the triangle as $V = \lambda_1\lambda_2 A_0$, for principal stretches λ_1, λ_2. With the forces thusly calculated, they are mapped from the xy-plane back to global coordinates and summed over every triangle constituting the membrane surface.

2.5.2 ELASTIC STRESS

For a purely elastic capsule, the Cauchy stress caused by deformation is determined using a two-dimensional constitutive law. Comprehensively discussed by Barthes-Biesel *et al.* [5], there are two hyperelastic constitutive laws of particular interest here. First, a Mooney-Rivlin law, such as the neo-Hookean law, has purely shear elasticity and, consequently, does not enforce surface area conservation. The neo-Hookean constitutive law may be expressed by the energy-strain relation

$$\mathrm{W}_{\mathrm{NH}} = \frac{E_s}{2}(\lambda_1^2 + \lambda_2^2 + \lambda_1^{-2}\lambda_2^{-2} - 3). \tag{56}$$

for shear elasticity modulus E_s and principal stretches λ_1, λ_2 [9]. The principal stretches are the positive square roots of the eigenvalues of the right Cauchy-Green tensor $\mathbb{G} = \mathbb{F}^T\mathbb{F}$. Second, a Skalak constitutive law includes both shear elasticity and the local conservation of surface area. The energy-strain relation for the Skalak constitutive law considered here is

$$\mathrm{W}_{\mathrm{SK}} = \frac{E_s}{4}\Big((\lambda_1 + \lambda_2 - 2)^2 + 2(\lambda_1 + \lambda_2 - 2) - 2(\lambda_1^2\lambda_2^2 - 1) + C(\lambda_1^2\lambda_2^2 - 1)^2\Big) \tag{57}$$

with the additional parameter C representing the ratio of the area dilation modulus to the shear modulus [5]. Measures of C for red blood cells are on the order of 10^5, but setting C this large requires an impracticably small timestep [64]. This consideration uses $C = 15$, which permits some change in capsule surface area, while preventing significant dilation or compression. Spherical capsules may be adequately described by a neo-Hookean constitutive law; indeed, some dilation of a sphere is necessary for any sort of deformation. For biconcave capsules, however, the incompressibility of the membrane is a significant factor. Consequently, in subsequent results, spherical and biconcave capsules are described by neo-Hookean and Skalak constitutive laws, respectively. From these constitutive laws, the principal stresses may be derived for the Neo-Hookean law as

$$\sigma_1 = \frac{1}{\lambda_2}\frac{\partial \mathrm{W_{NH}}}{\partial \lambda_1} = \frac{E_s}{\lambda_1\lambda_2}\Big(\lambda_1^2 - \frac{1}{\lambda_1^2\lambda_2^2}\Big) \tag{58}$$

$$\sigma_2 = \frac{1}{\lambda_1}\frac{\partial \mathrm{W_{NH}}}{\partial \lambda_2} = \frac{E_s}{\lambda_1\lambda_2}\Big(\lambda_2^2 - \frac{1}{\lambda_1^2\lambda_2^2}\Big) \tag{59}$$

and for the Skalak law as

$$\sigma_1 = \frac{1}{\lambda_2}\frac{\partial \mathrm{W_{SK}}}{\partial \lambda_1} = \frac{E_s}{\lambda_1\lambda_2}\Big(\lambda_1^2(\lambda_1^2 - 1) + C(\lambda_1\lambda_2)^2(\lambda_1^2\lambda_2^2 - 1)\Big) \tag{60}$$

$$\sigma_2 = \frac{1}{\lambda_1}\frac{\partial \mathrm{W_{SK}}}{\partial \lambda_2} = \frac{E_s}{\lambda_1\lambda_2}\Big(\lambda_2^2(\lambda_2^2 - 1) + C(\lambda_1\lambda_2)^2(\lambda_1^2\lambda_2^2 - 1)\Big). \tag{61}$$

In concert with principal directions $\hat{\boldsymbol{\beta}}_1, \hat{\boldsymbol{\beta}}_2$ of the principal stretches λ_1, λ_2, the principal stresses may be used to compose the stress tensor

$$\boldsymbol{\sigma} = \sigma_1\hat{\boldsymbol{\beta}}_1\hat{\boldsymbol{\beta}}_1 + \sigma_2\hat{\boldsymbol{\beta}}_2\hat{\boldsymbol{\beta}}_2 \tag{62}$$

With $\boldsymbol{\sigma}$ known, the forces caused by the deformation may be calculated using Equation (55).

2.5.3 VISCOELASTIC STRESS

If the capsule has both shear elasticity and membrane viscosity, the relation between stress and strain may instead be described by a solid viscoelastic model. In the Kelvin-Voigt (KV) model, also used in the preceding two-dimensional model, membrane stress is computed as the sum of elastic and viscous stress resultants. Schematically, this may be represented by a spring and dashpot in parallel (see Figure 4). In response to the instability caused by Kelvin-Voigt, observed for the preceding two

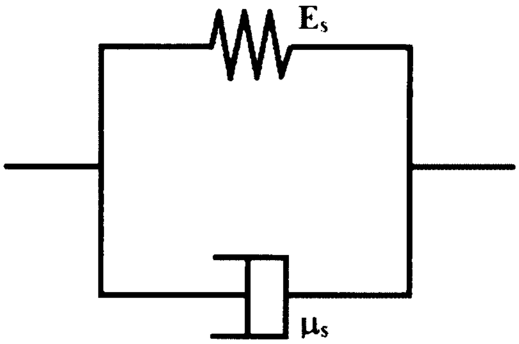

Figure 4. Schematic of the Kelvin-Voigt solid viscoelasticity model

dimensional model and noted by Bagchi and Yazdani for a three dimensional model, the standard linear solid (SLS) model is an attractive alternative. SLS considers a Maxwell element (which has a spring and dashpot in sequence) in parallel with a spring, as in Figure 5. Consequently, SLS approximates Kelvin-Voigt as the spring in the Maxwell element becomes sufficiently stiff. Approximating Kelvin-Voigt with SLS has the advantage of combining the improved stability of the SLS model with the time-independent elastic modulus of Kelvin-Voigt. Following Yazdani and Bagchi [63] and a convergence analysis (see Figure 12), the ratio of shear elasticity moduli $G = \frac{E_m}{E_s} = 50$ is considered to be sufficiently large to describe Kelvin-Voigt. All subsequent viscoelastic simulations using SLS are conducted with this approximation of the Kelvin-Voigt model.

To determine the stress resultant $\boldsymbol{\sigma}$, the non-linear theory of viscoelasticity is employed, which describes the standard linear solid model, with neo-Hookean elasticity. The resulting constitutive stress-strain relation is

$$\sigma_{ij} = -p\delta_{ij} + g_0 F_{ik} F_{jk} + \frac{1}{2} F_{ik} F_{jl} \int_0^t g_1(t-\tau) \frac{\partial G_{kl}(\tau)}{\partial \tau} d\tau \tag{63}$$

for deformation gradient $\mathbb{F}$, right Cauchy-Green tensor $\mathbb{G} = \mathbb{F}^T \mathbb{F}$, shear modulus $g_0 = \frac{E_s}{3}$, and relaxation function $g_1(t) = \frac{2}{3} E_m e^{-t/\tau_m}$ [11, 52]. Here, E_m is the shear modulus of the Maxwell element and the relaxation time constant $\tau_m = \frac{E_m}{\mu_s}$ is given in terms of membrane viscosity μ_s. This computational model can be adapted to several viscoelastic paradigms. Since a two dimensional membrane is considered,

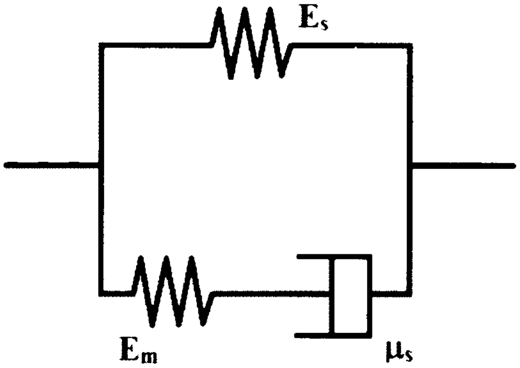

Figure 5. Schematic of the standard linear solid (SLS) viscoelasticity model

incompressibility requires that hydrostatic pressure p is

$$p = g_0|\mathbb{F}|^{-2} + \frac{1}{2}\int_0^t g_1(t-\tau)\frac{\partial|\mathbb{F}|^{-2}}{\partial\tau}d\tau \tag{64}$$

In the interest of computational efficiency, the time integrals in Equations (63) and (64) are approximated by assuming that $\mathbb{G}$ and $|\mathbb{F}|^{-2}$ vary linearly over a single timestep [52]. With this assumption, one may define the integral in Equation (63) at time t_n as

$$\mathbf{I}(t_n) = \int_0^{t_n} e^{-(t_n-\tau)/\tau_R}\frac{\partial\mathbb{G}}{\partial\tau}d\tau. \tag{65}$$

Knowing this integral at time t_n, $\mathbf{I}(t_{n+1})$ may be simplified as

$$\begin{aligned}\mathbf{I}(t_{n+1}) &= \int_0^{t_{n+1}} e^{-(t_{n+1}-\tau)/\tau_R}\frac{\partial\mathbb{G}}{\partial\tau}d\tau \\ &= \int_0^{t_n} e^{-(t_{n+1}-\tau)/\tau_R}\frac{\partial\mathbb{G}}{\partial\tau}d\tau + \int_{t_n}^{t_{n+1}} e^{-(t_{n+1}-\tau)/\tau_R}\frac{\partial\mathbb{G}}{\partial\tau}d\tau\end{aligned} \tag{66}$$

and

$$\mathbf{I}(t_{n+1}) = e^{-dt/\tau_R}\mathbf{I}(t_n) + \tau_R\frac{\mathbb{G}(t_{n+1}) - \mathbb{G}(t_n)}{dt}(1-e^{-dt/\tau_R}) \tag{67}$$

The same procedure is followed for the integral involving $|\mathbb{F}|^{-2}$ in Equation (64). As a result, the incorporation of membrane viscosity does not appreciably increase the computational cost of the algorithm.

However, the SLS method proposed here has a significant limitation: it is restricted to the neo-Hookean constitutive law and, consequently, cannot be used for a Skalak-like constitutive law. Consequently, for the remainder of this work, the viscoelastic model is only used with spherical capsules. To overcome this limitation, the more general and powerful approach developed by Yazdani and Bagchi is necessary, of which the previous algorithm is a felicitous special case [63]. A very brief depiction of their model follows:

The elastic stress in Equation (62) is decomposed into its deviatoric and volumetric parts, as

$$\boldsymbol{\sigma}_e = \boldsymbol{\sigma}^{dev} + \sigma^{vol}\mathbf{I} \tag{68}$$

and calculated using the shear elasticity modulus $E(0) = E_s + E_m$. Additionally, the time-dependent shear modulus is written as a Prony series, as

$$E(t) = E_s + E_m e^{-t/\tau_m}, \tag{69}$$

a formalism that may be extended to an arbitrary number of Maxwell elements by the addition of the corresponding exponential decay functions. With these definitions, the viscoelastic stress-strain relation may be written as

$$\boldsymbol{\sigma}_{ve} = \boldsymbol{\sigma}^{dev} + \mathrm{SYM}\Big(\int_0^t \frac{1}{E(0)}\frac{dE(s)}{ds}\,\mathbb{F}_t^{-1}(t-s)\cdot\boldsymbol{\sigma}^{dev}(t-s)\cdot\mathbb{F}_t(t-s)ds\Big) + \sigma^{vol}\mathbf{I} \tag{70}$$

in which $\mathbb{F}_t(t-s) = \frac{\partial \mathbf{x}(t-s)}{\partial \mathbf{x}(t)}$ is the deformation gradient between times $t-s$ and t. The operator SYM enforces the theoretical symmetry of the integral. In the interest of simplicity, the volumetric stress has not been transformed, although a similar process suffices to do so. The numerical analysis necessary to efficiently compute this Equation is non-trivial, and has been clearly worked out in Dassault's ABAQUS Theory Manual [14].

2.5.4 BENDING STIFFNESS

Helfrich's formulation of the bending energy of a zero-thickness membrane is given as

$$W_b = \frac{E_B}{2}\int_S (2\kappa - c_0)^2 dS + E_g \int_S \kappa_g dS \tag{71}$$

for the bending stiffness modulus E_B of mean curvature, the bending stiffness modulus E_g of Gaussian curvature, capsule surface area S, mean curvature κ, Gaussian curvature κ_g, and spontaneous curvature c_0 [64]. For a closed surface, $\int_S \kappa_g dS$ is invariant, according to the Gauss-Bonnet theorem and, consequently, may be omitted. For the first integral in Equation (71), on the other hand, Ou-Yang and Helfrich [41] take the first variation and derive the bending force density at a node as

$$\mathbf{f}_b = E_B\Big[(2\kappa + c_0)(2\kappa^2 - 2\kappa_g - c_0\kappa) + 2\,\Delta_{\mathrm{LB}}\,\kappa\Big]\hat{\mathbf{n}}, \tag{72}$$

in which Δ_{LB} is the Laplace-Beltrami operator. Spontaneous curvature c_0 is not simply the three dimensional analogue of the two dimensional preferred curvature k_0. For spherical capsules, the choice of spontaneous curvature is $c_0 = 0$, which indicates that the membrane does not have an internal/external asymmetry and leads to $\mathbf{f}_b = 0$ for the undeformed sphere. Several spontaneous curvatures are considered for biconcave capsules and discussed in more detail in Chapter 4.

The curvature of the capsule at each node was calculated using the quadratic surface fitting approach described by Garimella and Schwartz [26]. For each node $\mathbf{X}_p$, the outward unit normal vector for each triangle surrounding $\mathbf{X}_p$ is calculated and an unweighted average of these vectors is used as an approximate outward unit normal vector $\hat{\mathbf{n}}$ to $\mathbf{X}_p$. Based on this normal vector, the rotation matrix $\mathbf{R} = [\mathbf{r}_1, \mathbf{r}_2, \mathbf{r}_3]^T$ may be constructed, in which

$$\mathbf{r}_1 = \frac{(\mathbf{I} - \hat{\mathbf{n}}\hat{\mathbf{n}}^T)\hat{\mathbf{i}}}{\|(\mathbf{I} - \hat{\mathbf{n}}\hat{\mathbf{n}}^T\|} \tag{73}$$

$$\mathbf{r}_2 = \mathbf{r}_3 \times \mathbf{r}_1 \tag{74}$$

$$\mathbf{r}_3 = \hat{\mathbf{n}} \tag{75}$$

for $\hat{\mathbf{i}} = \hat{\mathbf{x}}$. This rotation matrix is used to map each neighboring node $\mathbf{X}_j$ of node $\mathbf{X}_p$, according to the equation

$$\mathbf{x}' = \mathbf{R}(\mathbf{X}_j - \mathbf{X}_p) \tag{76}$$

Using these n neighboring nodes (between 5 and 6, depending on the particular node), a system of Equations is constructed, as

$$\begin{bmatrix} x_1^2 & x_1y_1 & y_1^2 & x_1 & y_1 \\ \vdots & \vdots & \vdots & \vdots & \vdots \\ x_n^2 & x_ny_n & y_n^2 & x_n & y_n \end{bmatrix} \begin{bmatrix} a \\ b \\ c \\ d \\ e \end{bmatrix} = \begin{bmatrix} z_1 \\ \vdots \\ z_n \end{bmatrix} \tag{77}$$

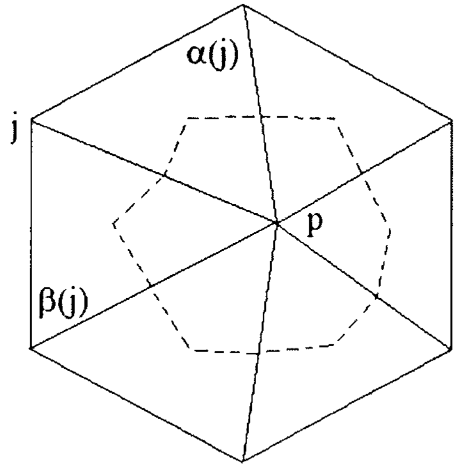

Figure 6. Neighborhood of vertex point P on the spherical surface. The dashed lines enclose the Voronoi region about P, based on the circumcenters of the triangular elements.

The icosahedron-based mesh has 12 nodes with $n = 5$, while the remainder have $n = 6$. If $n = 5$, the system of Equations is determined and is solved with LAPACK's DGESV routine [3]. For $n = 6$, the system is over-determined and a least-squared solution is found using LAPACK's DGELS routine [3]. From the solution, calculations may be made for Gaussian curvature κ_g,

$$\kappa_g = \frac{4ac - b^2}{(1 + d^2 + e^2)^2} \tag{78}$$

mean curvature κ,

$$\kappa = \frac{a + c + ae^2 + cd^2 - bde}{(1 + d^2 + e^2)^{3/2}} \tag{79}$$

and an improved unit outward normal vector $\hat{\mathbf{n}}$

$$\hat{\mathbf{n}} = \frac{1}{(1 + d^2 + e^2)^{1/2}} \mathbf{R}^{-1} \begin{bmatrix} -d \\ -e \\ 1 \end{bmatrix} \tag{80}$$

The discrete Laplace-Beltrami operator, acting on mean curvature κ at node $\mathbf{X}_p$

, may be represented as

$$\Delta_{\text{LB}}\,\kappa(\mathbf{X}_p) = \frac{1}{d}\sum_{j\in N(\mathbf{X}_p)} \omega_j\left[\kappa(\mathbf{X}_p) - \kappa(\mathbf{X}_\mathrm{j})\right] \tag{81}$$

for nodes $\mathbf{X}_\mathrm{j}$ belonging to the set $N(\mathbf{X}_p)$ of nodes which neighbor $\mathbf{X}_p$ [50]. The approach of [44] is followed, in setting the weights ω_j as

$$\omega_j = \frac{\cot(\alpha_j) + \cot(\beta_j)}{2} \tag{82}$$

in which α_j and β_j are defined as in Figure 6. Similarly, the normalization factor d is defined with the Voronoi region $\mathrm{a}_{\mathrm{vor}}$,

$$d = \mathrm{a}_{\mathrm{vor}} = \frac{1}{8}\sum_{j\in N(\mathbf{p})} [\cot(\alpha_j) + \cot(\beta_j)]\|\mathbf{X}_p - \mathbf{X}_j\|^2 \tag{83}$$

as given by [37] and depicted by area enclosed by the dashed line in Figure 6.

For biconcave capsules, net compressive or dilatory bending forces can lead to changes in the capsule volume. To maintain an approximately constant volume of the capsule, a penalty function is employed, which produces an isotropic force to counter the change in volume. Borrowed from Yazdani, the definition of the penalty function is

$$\mathbf{f}_{\text{vol}} = K_v \frac{V_c - V_{c0}}{V_{c0}} \tag{84}$$

for capsule volume V_c, initial capsule volume V_{c0}, and penalty coefficient K_v [65]. This force is then added to bending and elastic (or viscoelastic) forces, which are distributed to the fluid by Equation (21).

2.5.5 VALIDATION

The results from this algorithm are compared with published data for the deformation of spherical capsules in shear flow. First, an elastic capsule at different capillary numbers is considered in Figure 7, against the results of Sui *et al.* [57] using a front-tracking lattice Boltzmann method, and Ramanujan and Pozrikidis [49] using a boundary element method. The algorithm proposed here slightly outperforms Sui *et al.* at larger Ca, being closer to the higher-order method of Ramanujan and Pozrikidis. Second, a comparison with Le [34] is made for different levels of bending stiffness. The results compare well, except for $E_b = 0$, where Le's method overshoots the results of the method proposed here. This is somewhat surprising, given

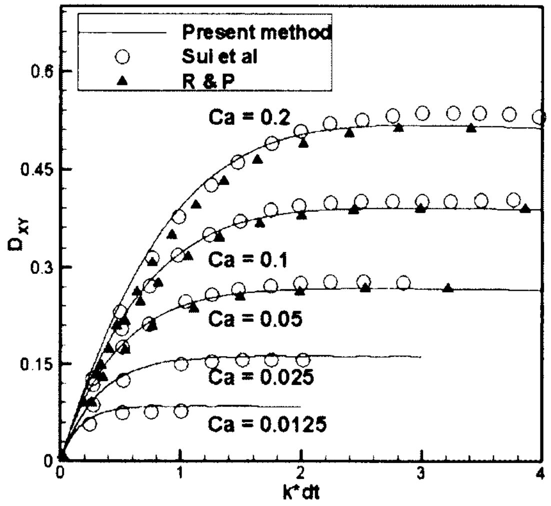

Figure 7. Comparisons for different capillary numbers Ca at $V = 1$, with $E_b = 0$ and $\eta = 0$. Open circles are from Sui *et al.* [57] and filled triangles are from Ramanujan and Pozrikidis [49].

the general robustness of Le's thin-shell method; due to the excellent agreement with Ramanujan and Pozrikidis for these parameters in Figure 7, the deviation here seems acceptable. Third, an additional comparison with [57] and [49] is conducted in Figure 9 for a fluid viscosity ratio $V = 5$, to evaluate the Heaviside approach for smoothing the viscosity jump across the capsule interface. This algorithm performs well, in terms of approaching the results from the boundary element method. Though the algorithm still overshoots Ramanujan and Pozrikidis as the capsule enters steady-state behaviour, particularly for Ca = 0.2, it clearly outperforms Sui *et al.* in steady-state. This last result is a pleasant surprise, since Sui *et al.* used somewhat finer Eulerian and Lagrangian meshes than are employed here.

Additionally, while there is not extensive published data with which the viscoelastic algorithm may be compared, its general behaviour may be evaluated. The convergence of the viscoelastic algorithm is considered in Figure 10 for increasingly fine meshes and is seen to converge nicely. Figure 11 considers the initial deformation of a spherical capsule with a viscoelastic membrane and varied η. The shear elasticity ratio $G = 50$ is fixed for each η, so that the model approximates the behaviour of

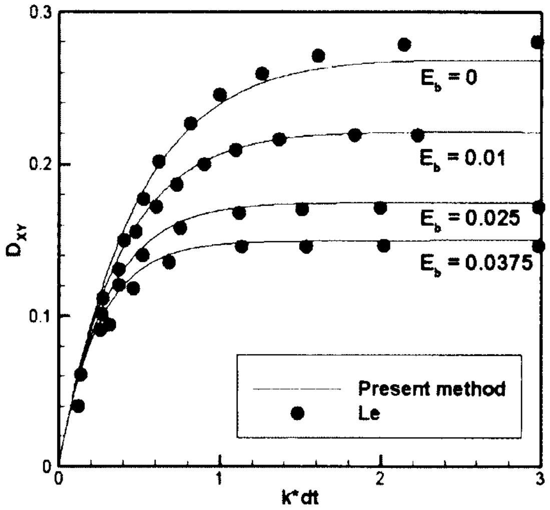

Figure 8. Comparisons for different bending stiffness E_b, with Ca $= 0.05$, $V = 1$, and $\eta = 0$. Filled circles are from Le [34].

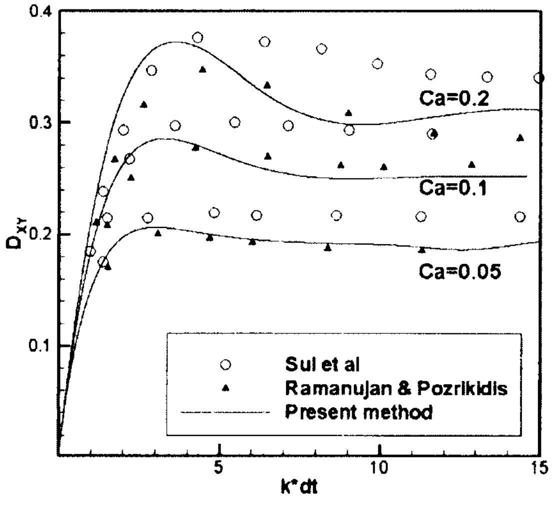

Figure 9. Comparisons for different capillary numbers Ca at $V = 5$, with $E_b = 0$ and $\eta = 0$. Open circles are from Sui *et al.* [57] and filled triangles are from Ramanujan and Pozrikidis [49].

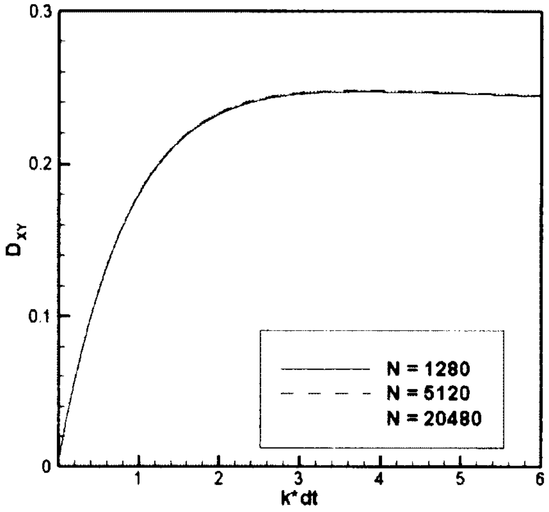

Figure 10. Convergence analysis of the viscoelastic model with capsule meshes having N = 1280, 5120, and 20480 triangles. Capsule parameters are Ca = 0.05, $E_b = 0$, $V = 1$, $\eta = 10$, and $G = 50$.

Kelvin-Voigt. To consider the convergence of the model to Kelvin-Voigt as G becomes large, Figure 12 compares G values for a given η. As the difference between the deformation for $G = 10$ and $G = 25$ is almost indiscernible, using $G = 50$ certainly seems sufficient to approximate Kelvin-Voigt.

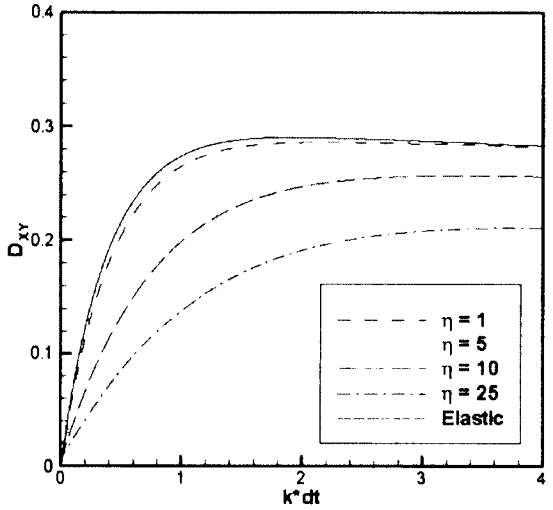

Figure 11. Comparison for different membrane viscosity ratios η for $G = 50$. Other parameters are $\text{Ca} = 0.05$, $E_b = 0$, and $V = 1$.

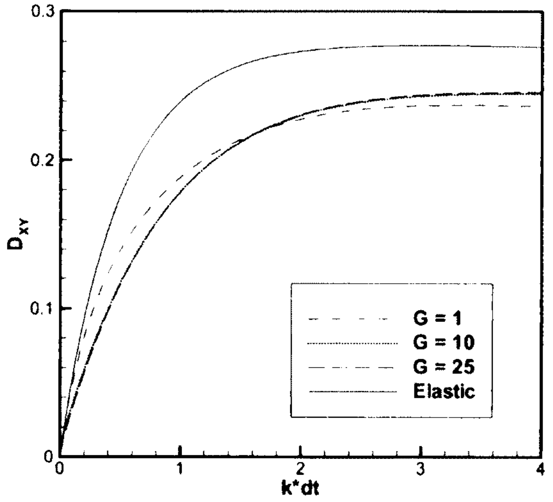

Figure 12. Comparison for different shear elasticity ratios G for $\eta = 10$. Other parameters are $\text{Ca} = 0.1$, $E_b = 0$, and $V = 1$.

CHAPTER 3

RESPONSE AND RECOVERY OF CIRCULAR AND SPHERICAL CAPSULES

Diaz and coworkers [20] considered the response and recovery of an elastic capsule in elongational flow. Finding that the capsule's response and recovery times could be determined by an exponential fitting of the Taylor deformation parameter, they investigated how these characteristic times depended on simulation parameters such as the fluid viscosity ratio and the capillary number. The response and recovery times of a capsule are important to understanding how a capsule will react in more complicated, time-dependent flows, as arise in medical and industrial applications [22]. Diaz *et al.* [19] extended their consideration to the response of a viscoelastic capsule in elongational flow and compared the respective impacts of different fluid and membrane viscosity ratios.

However, many of the attractive aspects of elongational flow, such as simpler computation due to axisymmetry, may also potentially restrict the applicability of its results. For instance, fluid and membrane viscosity ratios do not affect the steady-state shape of a capsule in elongational flow, and the capsule's membrane does not rotate around the capsule [8]. In contrast, the deformation of a capsule in shear flow has dynamical and angular aspects which do not occur in elongational flow. Additionally, the steady-state shape of a capsule in shear flow depends on a range of parameters — capillary number, bending stiffness, membrane and fluid viscosity ratios — as do the capsule's angle of inclination and tank-treading frequency.

Nonetheless, Diaz and coworkers [20] applied their exponential-fitting methodology to the results of Ramanujan and Pozrikidis [49] for the deformation of a spherical capsule in shear flow. They found instructive parallels between their results, including a near constant ratio between response times in elongational and shear flows, for capsules with equal steady-state deformation, as measured by the Taylor deformation parameter. This striking comparison, however, is limited because Ramanujan and Pozrikidis did not model the membrane viscosity, and neither study incorporated bending stiffness. This chapter considers the analogy in more complete two and three dimensional settings, with elastic and viscoelastic capsules that may resist bending and have a non-unity fluid viscosity ratio.

3.1 SETUP

An initially unstressed circular or spherical capsule was positioned in the center of the shear flow domain. Shear flow deformed the capsule until the system had reached its equilibrium behavior. During this process, the Taylor deformation parameter D_{xy} increases from 0 to a maximum value $\mathrm{D_{max}}$ at time t_{max}. Subsequently, at equilibrium, D_{xy} either maintains a near-constant value or undergoes a damped oscillation, depending on the steady-state behaviour. The shear flow was then stopped, by adjusting the boundary conditions. Denote this stopping time as t_{stop} and let $\mathrm{D_{stop}} = D_{xy}(t_{stop})$, after which the system was allowed to relax. As a result, the capsule gradually recovered its initial circular shape and $D_{xy} \to 0$. An instance of deformation and recovery is displayed in Figure 13, with $A = t_{max}$ and $B = t_{stop}$. Though it often is the case that $\mathrm{D_{max}} \approx \mathrm{D_{stop}}$, this is not necessary, and does not occur for large V and/or η.

Previous experimental and theoretical studies have generally measured the recovery process with respect to the membrane stretch ratio λ (or an equivalent parameter) [13, 21], or the width-to-length ratio $\frac{W}{L}$ [7]. The Taylor deformation parameter has been chosen here for two reasons. First, it is currently the standard metric for measuring the shape changes of capsules and was used by Diaz's group [19, 20]. Second, it reflects, however imperfectly, the entire capsule shape, rather than the focusing on a particular segment of the shape. It does not uniquely represent the capsule's shape, but neither do the other metrics.

Both the deformation and decay curves of the Taylor deformation parameter were found to be approximately exponential, as Diaz and colleagues had proposed [19, 20]. A least squares method is used to determine the capsule's response and recovery times by fitting exponential functions to D_{xy}. First, the response time τ_s is determined with the model

$$D_{xy}(t) = \mathrm{D_{max}}[1 - e^{-t/(k\tau_s)}], \tag{85}$$

fitted to D_{xy} over the interval $t = [0, t_{max}]$, where k is the fluid shear rate. Second, the function

$$D_{xy}(t) = \mathrm{D_{stop}}[e^{-t/(k\tau_R)}] \tag{86}$$

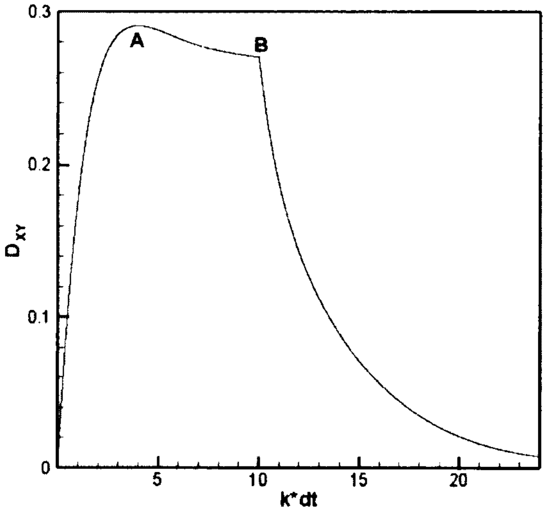

Figure 13. Example of spherical capsule shape deformation and recovery. Points A and B indicate times t_{max} and t_{stop}, respectively. Simulation parameters are Ca = 0.1, $E_b = 0$, $V = 5$, and $\eta = 1$.

is fitted to D_{xy} for $t = [t_{stop}, \infty]$ to define the recovery time τ_r. Since $\mathrm{D_{max}}$ and $\mathrm{D_{stop}}$ are factored out, the response and recovery times characterize how quickly the capsule arrives at the steady-state deformation and recovers the original shape, respectively, independent on the extent of deformation or recovery. A large response or recovery time indicates a slower response or recovery process, since it describes a slow exponential decay in the models. Figure 14 shows an example of a D_{xy} curve compared with data points from the best fitting response and recovery exponential curves; the exponential curves provide sufficient, if imperfect, description of the simulation results.

In general, exponential fittings for the response and recovery models had a correlation coefficients $R^2 > 0.99$. However, this failed to be the case in two sets of instances. For larger E_b, the recovery model was less accurate, with R^2 as low as 0.92. Also, for high V or η, the response model only had correlation coefficients $R^2 > 0.97$. In contrast, Diaz *et al.*'s fitting for response times in elongational flow had correlation coefficients in excess of 0.98 in all instances [19].

This simulation and analysis was performed for circular and spherical capsules in

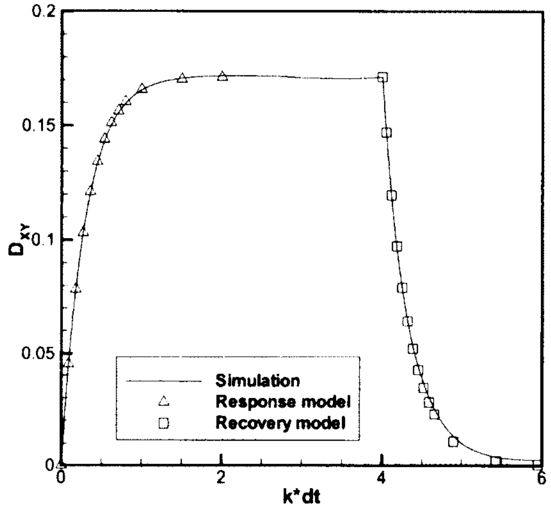

Figure 14. Example of exponential fitting for sphere with Ca = 0.05, E_b = 0.025, $V = 1$, and $\eta = 0$

two and three dimensions, respectively. For both settings, simulations are conducted for a variety of the four dimensionless parameters: Ca, E_b, V, and η. In this way, the roles of each parameter in determining the characteristic times of capsule shape change can be isolated. In the following graphics, the parameter being varied is placed on the x-axis, with the dimensionless response time $k\tau_s$ and recovery time $k\tau_r$ on the y−xis. Additionally, when useful, the characteristic times are considered in the context of their respective timescales, using the notation and definitions of Yazdani and Bagchi [63].

3.2 CAPILLARY NUMBER

Figure 15 shows response and recovery times over a range of capillary numbers for circular and spherical capsules. The constant parameters in the two and three dimensional settings are comparable, but not identical. The relationships between the characteristic times and the capillary number are quite similar for the circle and sphere: recovery time $k\tau_r$ is almost directly proportional with Ca, while response

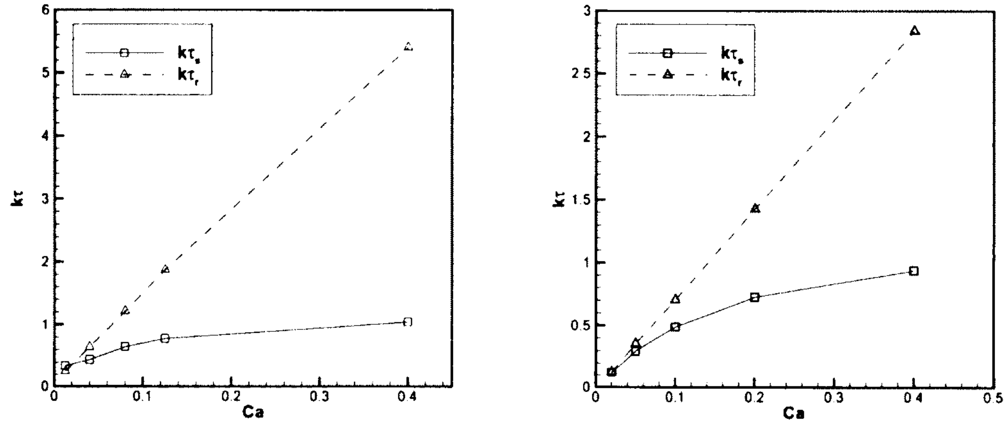

Figure 15. For circular (left) and spherical (right) capsules, response times τ_s (solid lines and rectangles) and recovery times τ_r (dotted lines and triangles) from simulations varying capillary numbers Ca. Unvaried parameters for circular capsules are $E_b = 0.05$, $V = 1$, and $\eta = 0$. Unvaried parameters for spherical capsules are $E_b = 0.025$, $V = 1$, and $\eta = 0$.

time $k\tau_s$ rises linearly but modestly with Ca. The basic result is intuitive, as increasing Ca means that the capsule's reaction to deforming fluid forces or the lack thereof is decreased. Thus, it takes longer for the capsule to either reach steady-state deformation or recover the initial shape.

To understand the sharp difference in how strongly the characteristic times depend on Ca, it is worthwhile to consider the characteristic times normalized by the elastic timescale $\tau_e = \frac{V\mu_a a}{E_s}$. Plotted in Figure 16, the normalized recovery time τ_r/τ_e is nearly constant for Ca ≥ 0.1. Conversely, the normalized response time τ_s/τ_e continues to decrease as Ca rises. This contrast between response and recovery seems reasonable, as the recovery is driven (in part) by the stored elastic energy in the capsule, which is proportional to E_s, and it would be plausible to expect the recovery time to be inversely proportional to the stored elastic energy. Thus, normalizing the recovery time by a timescale that is also inversely proportional to E_s naturally produces an approximately constant value. For very small Ca with circular capsules, $k\tau_r$ is too large for this relationship to hold. One possible explanation is that, when shear flow is stopped at the boundaries, it takes a small amount of time for the flow

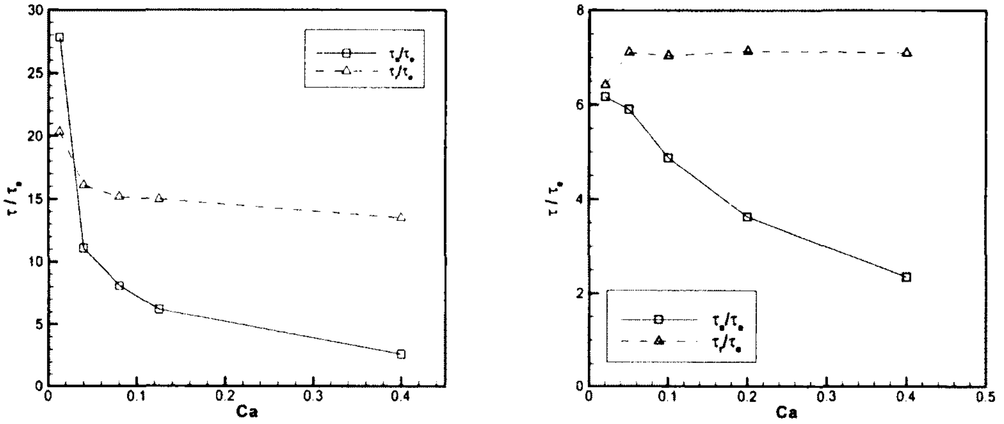

Figure 16. For circular (left) and spherical (right) capsules, normalized response (solid lines and rectangles) and recovery times (dotted lines and triangles) from the simulations in Figure 15. Characteristic times are normalized by the shear timescale τ_e.

nearer to the capsule to slow. While this delay is too small to alter the relationship for the longer times that a larger Ca requires, it may account for the deviation shown here. On the other hand, capsule deformation is driven by a continual flow adding energy to the fluid-structure interaction system. As a result, increasing the capillary number leads only to a small increase in $k\tau_s$, with the rate of increase declining as Ca rises.

Diaz and coworkers [20] generally observed the same relationships seen in Figure 16 during their simulations using elongational flow, including the near constant normalized recovery time τ_r/τ_e. However, one significant difference is observed: in elongational flow, τ_s/τ_e starts to increase when Ca is very large. The reason for this discrepancy seems to be the difference between what constitutes a large capillary number in elongational and shear flows. For Diaz and coworkers, the increase is observed for Ca in the range of 0.06 – 0.08, while capsule breakup (due to excessive deformation) in their elongational flow occurs near Ca = 0.09. On the other hand, the maximum value of Ca = 0.4 considered in the two and three dimensional models of shear flow does not approach the value at which breakup occurs.

Ultimately, two general observations may be made, based on these results. First, the capsule's elastic character has substantially different effects on the shape deformation and recovery of circular and spherical capsules; one process is not simply the reverse of the other. Second, the two and three dimensional models produce nearly equivalent qualitative results, though the constant ratio τ_r/τ_e is cleaner for the spherical capsule. This similarity occurs despite a Hookean law being used for the circular capsule and a neo-Hookean law for the spherical capsule.

3.3 BENDING STIFFNESS

Bending stiffness is modeled rather differently in the two and three dimensional versions of the algorithm. In two dimensions, bending stiffness is associated with a specific preferred curvature for each element of the capsule. As elements of the capsule deviate from that curvature, bending moments result. For an undeformed circular capsule, no bending moment exists in Equation (32) and, as a result, no bending forces result. On the other hand, in three dimensions, bending energy depends on spontaneous curvature c_0. For a sphere, $c_0 = 0$ makes the resultant force in Equation (72) equal to zero. Thus, it is the first variation that is minimized by the spontaneous curvature, and not the bending energy in Equation (71).

A comparison of the response and recovery times of circular and spherical capsules over a range of bending stiffnesses E_b is shown in Figure 17. A clear inverse relationship between $k\tau_r$ and E_b may be observed for both the circular and spherical capsules. In both settings, a capsule with $E_b = 0$ still recovers its shape, thanks to the hydrodynamics, and $k\tau_r \to 0$ as E_b becomes large. Thus, increased bending stiffness causes the capsules to recover their initial shapes more quickly, independent of the extent of the deformation from which they must recover.

This similarity, however, does not extend to the response times: while the spherical capsules' $k\tau_s$ has the same inverse relationship with E_b that $k\tau_r$ has, this is not the case for circular capsules. Instead, $k\tau_s$ undergoes only a slight, almost linear decline as E_b rises for circular capsules. Thus, in addition to decreasing the extent of the capsule deformation, as was clear in Figures 2 and 8, bending stiffness also decreases the time that it takes for the capsule to reach steady-state. However, this decrease is much less for circular capsules than spherical capsules.

Thus, a meaningful difference exists here between response and recovery times, in the two and three dimensional models. In the three dimensional mode, the role of bending stiffness in altering the time necessary for shape change is qualitatively

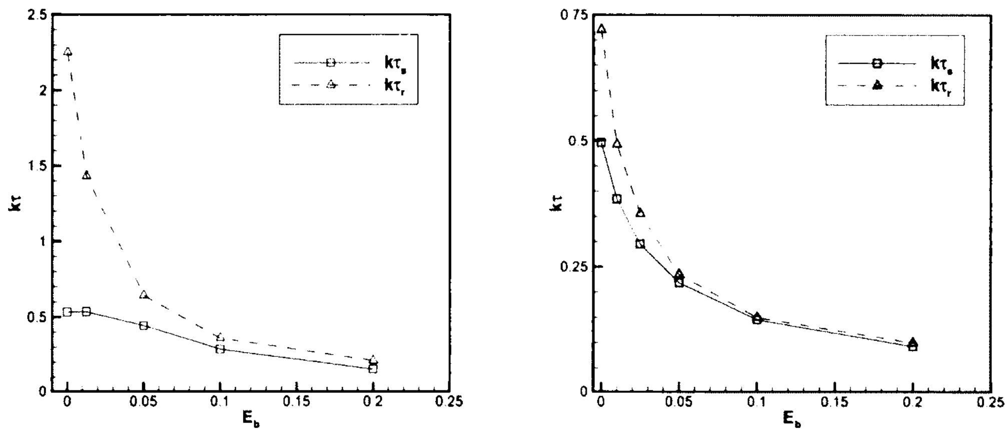

Figure 17. For circular (left) and spherical (right) capsules, response times τ_s (solid lines and rectangles) and recovery times τ_r (dotted lines and triangles) from simulations varying reduced bending stiffness moduli E_b. Unvaried parameters for circular capsules are Ca $= 0.04$, $V = 1$, and $\eta = 0$. Unvaried parameters for spherical capsules are Ca $= 0.05$, $V = 1$, and $\eta = 0$.

symmetric for response and recovery, while these processes are asymmetric in the two dimensional model. Interestingly, for larger E_b in both two and three dimensions, $k\tau_s \approx k\tau_r$, which suggests that for a sufficiently stiff capsule, the particular model of bending stiffness being used does not make a significant difference.

3.4 FLUID VISCOSITY RATIO

As the method for implementing a non-unity fluid viscosity ratio in Chapter 2 is identical for the two and three dimensional versions of the model, it would be natural that characteristic times have the same relationships with V for circular and spherical capsules. As may be seen in Figure 18, this is indeed the case. Both $k\tau_s$ and $k\tau_r$ have approximately linear relationships with V, with the time required for response and recovery increasing with the fluid viscosity ratio. Note that the steady-state deformation of a capsule with small V is, *ceteris paribus*, much larger than a capsule with a larger V (compare, for instance, a given Ca in Figures 7 and 9). As the response and recovery times shown here are independent of the extent of the deformation, taking into account the extent of the deformation means that the time

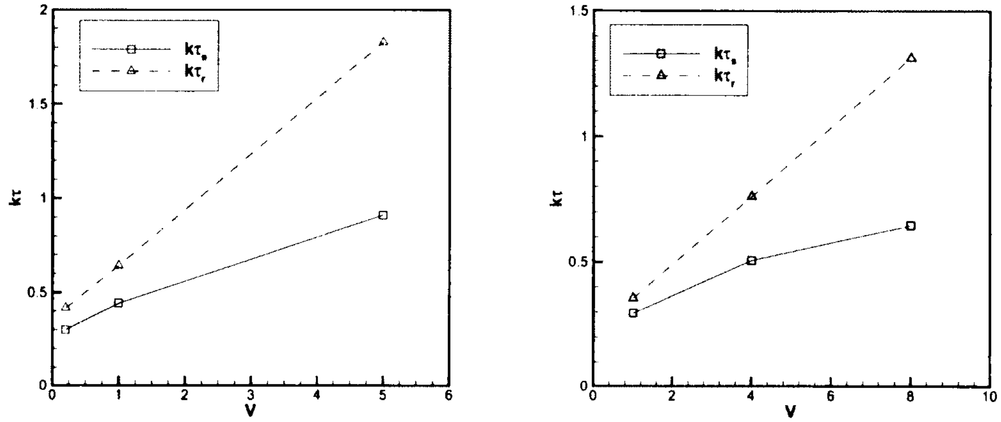

Figure 18. For circular (left) and spherical (right) capsules, response times τ_s (solid lines and rectangles) and recovery times τ_r (dotted lines and triangles) from simulations varying fluid viscosity ratio V. Unvaried parameters for circular capsules are $\mathrm{Ca} = 0.04$, $E_b = 0.05$, and $\eta = 0$. Unvaried parameters for spherical capsules are $\mathrm{Ca} = 0.05$, $E_b = 0.025$, and $\eta = 0$.

necessary for response or recovery seems to grow even more quickly with V.

As Ramanujan and Pozrikidis have noted, increasing V has the effect of decreasing the ratio of "deforming stresses to restoring tensions" [49]. The difference between how strongly the characteristic times depend on V is the same reason noted in the discussion of the capillary number, except from the opposite side of the coin: recovery is driven by the dissipation of finite amount of energy stored in the membrane, while deforming stress is supplied by the continual shear flow. Thus, the speed of the capsule's recovery process is more adversely impacted by a high fluid viscosity inside the capsule than is the capsule's response to deformation. As $V \to 0$, during which the capsule's response and recovery is (relatively) unimpeded by the fluid inside the capsule, the characteristic times tend toward $k\tau_r \approx k\tau_s$.

3.5 MEMBRANE VISCOSITY RATIO

Though a Kelvin-Voigt viscoelastic model is described in both the two and three dimensional simulations, the membrane viscosity ratio had very different relationships with the characteristic times in two and three dimensions. Seen on the left

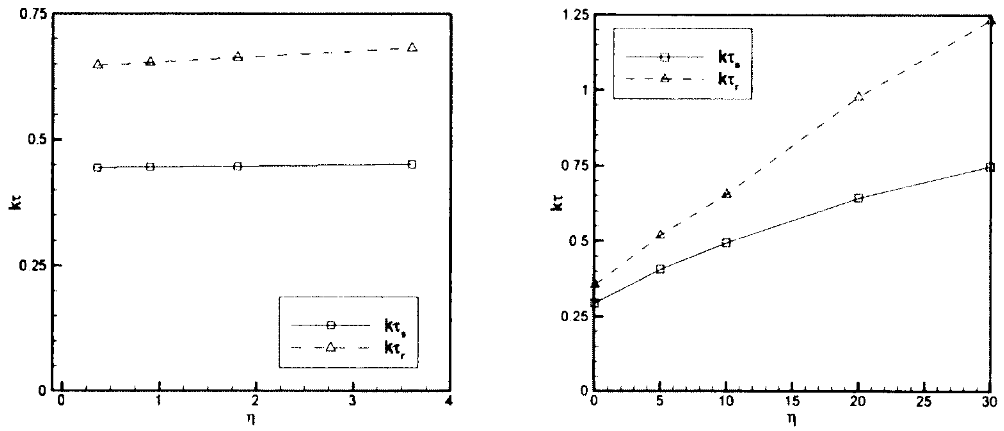

Figure 19. For circular (left) and spherical (right) capsules, response times τ_s (solid lines and rectangles) and recovery times τ_r (dotted lines and triangles) from simulations varying membrane viscosity ratio η. Unvaried parameters for circular capsules are Ca $= 0.04$, $E_b = 0.05$, and $V = 1$. Unvaried parameters for spherical capsules are Ca $= 0.05$, $E_b = 0.025$, and $V = 1$.

side of Figure 19, both $k\tau_s$ and $k\tau_r$ were virtually independent of the membrane viscosity ratio η for circular capsules; only the slightest of increases in $k\tau_s$ and $k\tau_r$ are observed. While the range of η considered was, admittedly, not large, the shapes of the capsules considered were also identical. Though the largest η value shown here does not represent an upper bound, meaningfully larger η led to instabilities in the two dimensional Kelvin-Voigt model.

On the other hand, in three dimensions, the characteristic times displayed a clear linear dependence on η, as on the right side of Figure 19. Here, the superior stability of the SLS implementation of Kelvin-Voigt allowed much larger η values to be considered. Still, even for $\eta \leq 4$, the difference between circular and spherical capsules is substantial. It is possible that the SLS implementation of Kelvin-Voigt is to blame for the difference, but it is not apparent how: Figure 12 shows that the model clearly approaches a shear elasticity modulus ratio G-independent approximation of Kelvin-Voigt. More likely, the difference is caused by the dimensions of the problem. Stress in Kelvin-Voigt is proportional to the derivative(s) of principal stretch(es) λ with respect to time. As a result, it may be that the two principal stretches in three

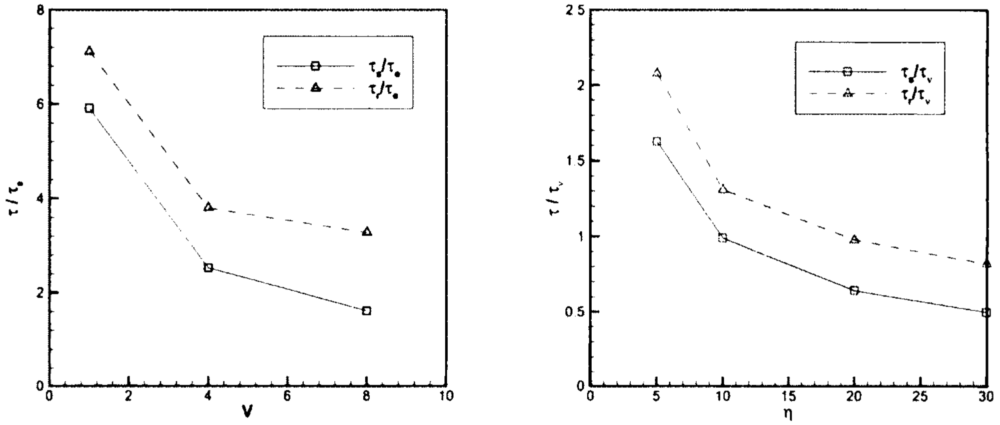

Figure 20. For spherical capsules, normalized response (solid lines and rectangles) and recovery times (dotted lines and triangles) from the simulations in Figures 18 (left) and 19 (right). Characteristic times are normalized by the shear timescale τ_e (left) and viscoelastic timescale τ_ν (right).

dimensions undergo significantly larger changes in time than the single principal stretch in two dimensions.

More interestingly, for spherical capsules, the relationships between the characteristic times and η display a striking qualitative similarity to the aforementioned relationships with V. Further, the similarity remains when each set of results is normalized in Figure 20 by its respective timescale: elastic timescale $\tau_e = \frac{V\mu_a a}{E_s}$ for the variation of V and viscoelastic timescale $\tau_\nu = \frac{\mu_s}{E_s}$ for the variation of η. The result is, perhaps, unprofound: whether solid or fluid, viscosity is the same basic physical quality and, as a result, ought to have comparable basic impacts on the fluid-structure interaction. Yet it is nonetheless promising: perhaps the model may be simplified by using a fluid viscosity ratio to approximate the effects of a membrane viscosity ratio, or vice versa. Alternately, perhaps the fluid and membrane viscosity models could be accurately incorporated into a single model. These suggestions will be revisited in Chapter 5.

CHAPTER 4

SHAPE RECOVERY OF BICONCAVE CAPSULES

4.1 TWO DIMENSIONS

A biconcave capsule in shear flow has several types of steady-state behaviour. Skotheim and Secomb's theoretical investigations of biconcave capsule dynamics suggest three distinct behaviours: (1) tumbling, (2) tank-treading with oscillations in the angles of inclination, and (3) intermittent tumbling and tank-treading [54]. In general, a tumbling capsule is characterized by flipping end-over-end, as if it were a rigid body. Consequently, while there is shape change during tumbling behaviour, a biconcave capsule remains largely biconcave. On the other hand, tank-treading involves the membrane rotating around the capsule. During tank-treading, the shape of the capsule and its angle of inclination may undergo periodic oscillations. In the event of significant angular oscillations, this may be denoted as a separate behaviour: 'swinging'. The intermittent behaviour has been further clarified by Yazdani and Bagchi, who have identified a new behaviour they call 'breathing' [64], in which the capsule undergoes significant shape changes without angular oscillations. Simulations have shown that the capillary number, bending stiffness, fluid viscosity ratio, and membrane viscosity ratio all play some role in determining a capsule's equilibrium behavior [40, 54, 56, 63, 64].

However, the terminology in this consideration will be restricted to tank-treading and tumbling. Beyond the obvious advantage of simplicity, there are two reasons for such a restriction. First, juxtaposing tank-treading and tumbling capsules provides an instructive comparison in itself, as these behaviours occupy relatively opposite positions in the parameter space. Each capsule parameter can be meaningfully varied, while maintaining the same sort of equilibrium behaviour. Second, the subtler modes explored in [64] are not accessible with a two dimensional model, due to both the simpler geometry and the important differences between bending stiffness in two and three dimensions.

For ensembles of biconcave capsules with both tank-treading and tumbling steady-state behaviours, the capsules are deformed in shear flow. After the capsules reach steady-state behaviour, the shear flow is abruptly stopped. For reasons that will be discussed later, shear flow is stopped when tumbling capsules have a reached a specified angle of inclination and when the membranes of tank-treading capsules are at a specific point in their rotation. The capsules subsequently undergo a relaxation process and, except for one case, recover their initial biconcave shapes. These recoveries are modeled and their dependence on simulation parameters is compared.

4.1.1 TANK-TREADING CAPSULES

A tank-treading two-dimensional biconcave capsule, deformed in shear flow, has an oblong, oval shape [56]. While the capsule membrane tank-treads in the clockwise direction in the equilibrium state, the Taylor deformation parameter and angle of inclination undergo small oscillations. Denote the time when shear flow is stopped as t_{stop} and let $\mathrm{D}_{\mathrm{stop}} = D_{xy}(t_{stop})$. After t_{stop}, it is observed that the Taylor deformation parameter briefly decreases from $\mathrm{D}_{\mathrm{stop}}$ to a minimum value $\mathrm{D}_{\mathrm{min}}$, at a time which is denoted t_{min}. Subsequently, D_{xy} undergoes a much slower and longer increase back to its undeformed value, $D_{xy} \approx 0.812$. Call this final value D_{∞} and the time at which it is achieved t_{∞}.

An example of the recovery is depicted in Figure 21, with $\mathrm{D}_{\mathrm{stop}}$, $\mathrm{D}_{\mathrm{min}}$, and D_{∞} being reached at times $A = t_{stop}$, $B = t_{min}$, and $C = t_{\infty}$, respectively. The corresponding capsule shapes at these times are shown in Figure 22. Note that, beyond the capsule shortening, little shape change occurs between A and B. Nor does tank-treading occur within this interval; the position of the capsule node denoted in Figure 22 is nearly identical at A and B. In contrast, the major curvature changes necessary to return to biconcavity occur almost entirely between B and C.

The only exception to this behaviour occurred for capsules with $E_b = 0$. In such cases, the initial behavior was similar to capsules with bending stiffness: after shear flow was stopped, D_{xy} declined modestly over a short interval, from a $\mathrm{D}_{\mathrm{stop}}$ to a $\mathrm{D}_{\mathrm{min}}$. However, upon reaching $\mathrm{D}_{\mathrm{min}}$, the capsule underwent no further significant change in shape; thus, $\mathrm{D}_{\mathrm{min}} \approx D_{\infty}$. Figures 23 and 24 display the Taylor deformation parameter after shear flow is stopped and the shapes corresponding to the denoted times, respectively. As before, designate $A = t_{stop}$, $B = t_{min}$, and $C = t_{\infty}$. With $E_b = 0$, the explicit curvature preference k_0 has no effect. Since an explicit curvature preference is the only aspect of the model related to the biconcave shape, this shape is not recovered.

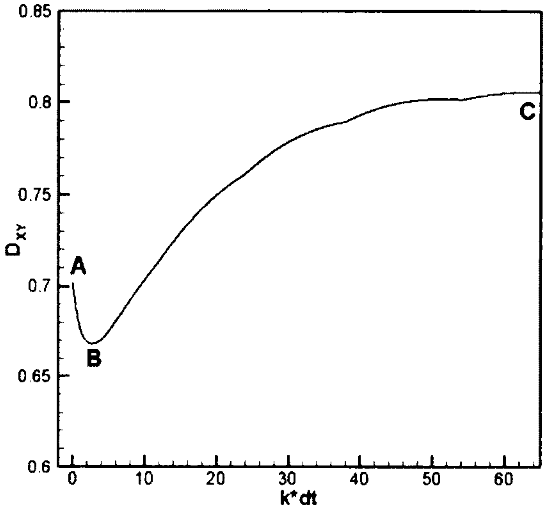

Figure 21. Shape recovery in terms of D_{xy} for a tank-treading capsule with bending stiffness. Capsule parameters are Ca = 0.067, $E_b = 0.0014$, $V = 1$, and $\eta = 6$.

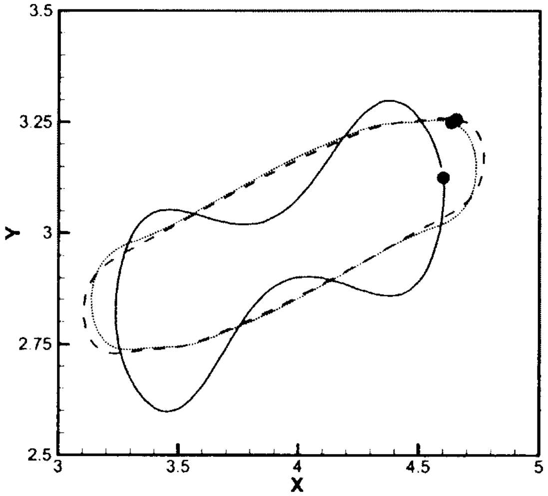

Figure 22. Shapes corresponding to times A (dashed), B (dotted), and C (solid) in Figure 21. Solid circles indicate the current position of an element initially located at the end of the undeformed capsule.

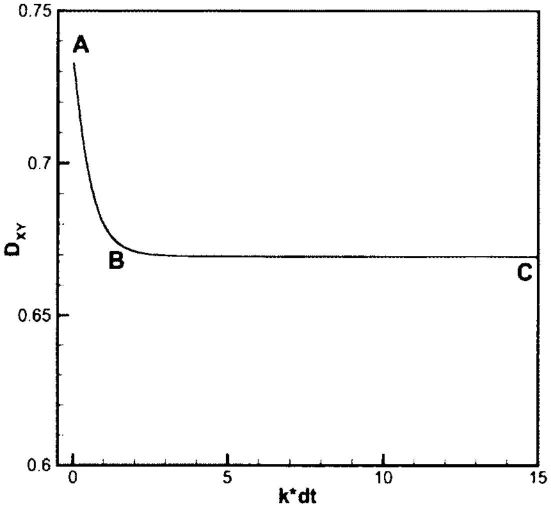

Figure 23. Shape change in terms of D_{xy} for a tank-treading capsule without bending stiffness. Capsule parameters are Ca = 0.135, $E_b = 0$, $V = 1$, and $\eta = 0$.

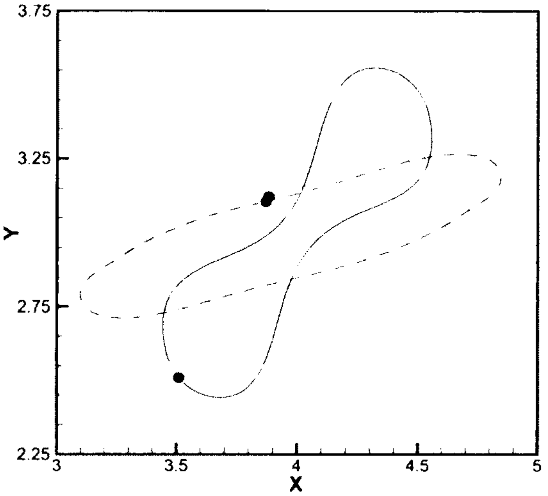

Figure 24. Shapes corresponding to times A (dashed), times B and C (dotted), and initial shape (solid) in Figure 23. Solid circles indicate the current position of an element located at the end of the undeformed capsule.

The non-monotonic recovery path in Figure 21 suggested that perhaps two distinct physical mechanisms were present: one acting over a brief timescale and accounting for the initial decline in D_{xy}, and another causing the shape recovery and operating over a longer period. To test this hypothesis, it seemed that modeling the recovery in two phases would be instructive. Exponential curves were fitted to the initial phase, from $\mathrm{D_{stop}}$ to $\mathrm{D_{min}}$, and the latter phase, from $\mathrm{D_{min}}$ to D_∞, and the values of $k\tau_R$ were compared. The resulting model equations, then, are

$$D_{xy}(t) = \mathrm{D_{min}} + \Big(\mathrm{D_{stop}} - \mathrm{D_{min}}\Big) e^{-t/(k\tau_{R1})} \tag{87}$$

$$D_{xy}(t) = D_\infty + \Big(\mathrm{D_{min}} - D_\infty\Big) e^{-t/(k\tau_{R2})} \tag{88}$$

over the time intervals $[t_{stop}, t_{min}]$ and $[t_{min}, t_\infty]$, respectively, with the beginning of each interval reset to $t = 0$. The same least-squares approach from Chapter 3 was used for the exponential fitting. Let $k\tau_{R1}$ and $k\tau_{R2}$ denote the recovery times which characterize the initial and latter phases, respectively. The fitted results had a coefficients of correlation $R^2 > 0.95$ and the majority of cases were in excess of 0.98. The poorest fits occurred for $k\tau_{R1}$ at small Ca, perhaps due to the same lingering flow observed at small Ca for circular capsules.

An ensemble of capsules with varied simulation parameters were considered, within the tank-treading parameter space, and the results are displayed in Figures 25 — 28. In each figure, a single parameter is varied, while all others remain constant. The fundamental difference between the recovery times which characterized the two phases was their duration: $k\tau_{R1}$ was generally $O(10^{-1})$ and $k\tau_{R2}$ was typically $O(10)$. Further, significant differences were observed between the roles of a given simulation parameter in the two phases. To facilitate such comparisons, the vertical axes in Figures 25 — 28 were scaled such that the right axis, for $k\tau_{R2}$, was 100 times $k\tau_{R1}$'s left axis.

The capillary number had the same role in both phases, as both $k\tau_{R1}$ and $k\tau_{R2}$ were nearly directly proportional with Ca in Figure 25. These relationships with the capillary number are thus quite similar to that of Ca and $k\tau_R$ for a circular capsule. In contrast, in Figure 26, it was found that $k\tau_{R2}$ was approximately inversely proportional with E_b. During the first phase, however, the recovery time $k\tau_{R1}$ decreased only slightly for larger bending stiffness. The fluid and membrane viscosity ratios had opposing roles over the two phases, as may be seen in Figures 27 and 28. It may be observed that $k\tau_{R2}$ was almost directly proportional with V, but there was

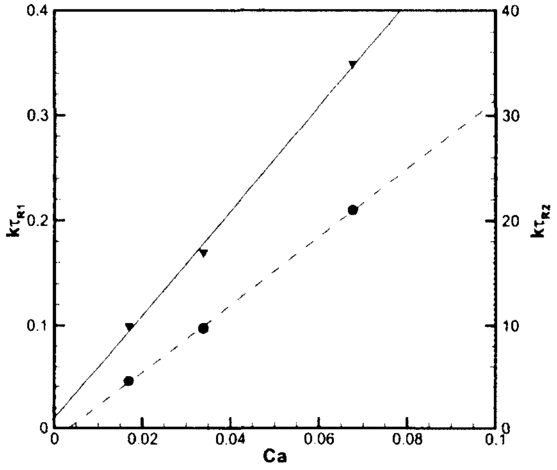

Figure 25. For a tank-treading capsule, $k\tau_{R1}$ (triangles, left axis) and $k\tau_{R2}$ values (squares, right axis) are compared for different Ca. The relationships between the parameter and the recovery times are approximated by solid ($k\tau_{R1}$) and dotted ($k\tau_{R2}$) lines. Unvaried parameters are $E_b = 0.0014$, $V = 1$, and $\eta = 0$.

a much weaker linear relationship between V and the initial recovery time $k\tau_{R1}$. On the other hand, while a significant linear relationship prevailed between $k\tau_{R1}$ and η, the latter recovery time $k\tau_{R2}$ was clearly independent of the membrane viscosity ratio.

In sum, the first phase of recovery is dominated by the capsule's viscoelastic character. Bending stiffness is irrelevant and the fluid viscosity ratio plays a secondary role. Indeed, for $\eta > 0$, one might make the approximation $k\tau_{R1} \sim Ca \cdot \eta$. This is significant because Ca$\cdot\eta \sim \frac{\mu_s}{E_s}$, the viscoelastic relaxation time used to characterize recovery from micropipette aspiration and optical tweezing with the Kelvin-Voigt model [13, 21, 28]. A comparable approximation of the second recovery phase would be $k\tau_{R2} \sim \frac{Ca \cdot V}{E_b}$. This phase focuses on the necessary changes for the capsule to return to its biconcave shape and for capsule elements to return to their initial positions. In general, the dependence of τ_{R2} on capsule parameters is very similar to the recovery times $k\tau_R$ of a circular capsule: direct proportionality with Ca, inverse proportionality with E_b, and a strong linear dependence on V.

Further, the two order of magnitude difference in scale is also consistent with

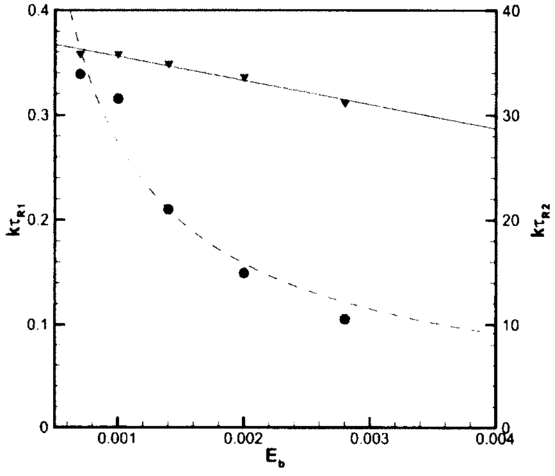

Figure 26. For a tank-treading capsule, $k\tau_{R1}$ (triangles, left axis) and $k\tau_{R2}$ values (squares, right axis) are compared for different E_b. The relationships between the parameter and the recovery times are approximated by solid ($k\tau_{R1}$) and dotted ($k\tau_{R2}$) lines. Unvaried parameters are $G = 0.067$, $V = 1$, and $\eta = 0$.

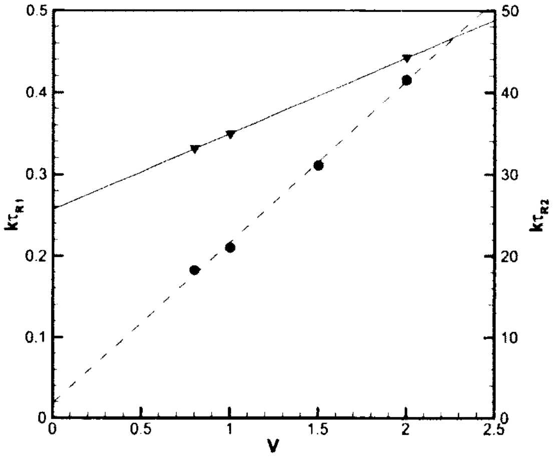

Figure 27. For a tank-treading capsule, $k\tau_{R1}$ (triangles, left axis) and $k\tau_{R2}$ values (squares, right axis) are compared for different V. The relationships between the parameter and the recovery times are approximated by solid ($k\tau_{R1}$) and dotted ($k\tau_{R2}$) lines. Unvaried parameters are $G = 0.067$, $E_b = 0.0014$, and $\eta = 0$.

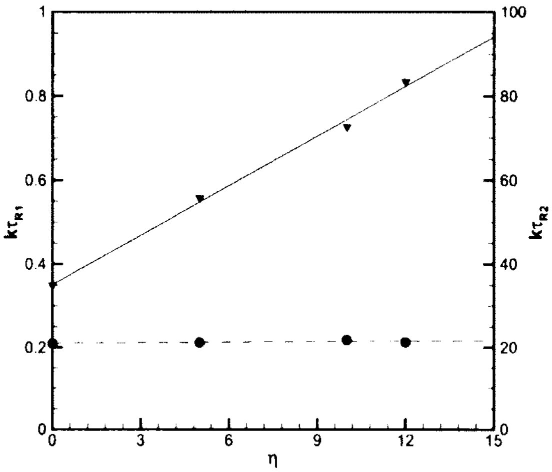

Figure 28. For a tank-treading capsule, $k\tau_{R1}$ (triangles, left axis) and $k\tau_{R2}$ values (squares, right axis) are compared for different η. The relationships between the parameter and the recovery times are approximated by solid ($k\tau_{R1}$) and dotted ($k\tau_{R2}$) lines. Unvaried parameters are $G = 0.067$, $E_b = 0.0014$, and $V = 1$.

experimental results. Evans and Hochmuth's measurements from micropipette aspiration measured $k\tau_R \approx 10^{-1}$ seconds [21]. On the other hand, Fischer reported measuring $10 - 30$ seconds for experiments of the shape recovery of red blood cells from tank-treading in shear flow [25]. One wonders if such a contrast may be explained by the two phases proposed here. Recovery from micropipette aspiration involves a small part of the membrane recovering from enormous viscoelastic stress, which is described by the first recovery phase. However, since micropipette aspiration does not involve the entire cell changing shape, the longer second recovery phase is absent. On the other hand, as seen here, recovery from tank-treading in shear flow necessitates both phases and consequently occurs over a much longer time.

An additional factor in the time course of shape recovery was the phase angle. Adopting the definition by Le [34], the position of an element membrane is quantified in terms of its phase angle β as

$$\beta(t) = \alpha(t) - \theta(t) - [\alpha(0) - \theta(0)], \tag{89}$$

in which $\alpha(t)$ and $\theta(t)$ are the current inclinations with respect to the flow field of a

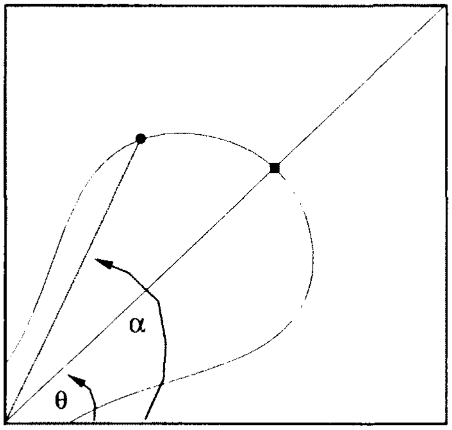

Figure 29. The angle of inclination θ of the capsule's major axis and the angle of inclination α of a membrane element (filled circle) are measured with respect to the x-axis, using the center of the capsule as the origin. Note that for a point at the end of the capsule (filled square), $\theta = \alpha$.

membrane element and capsule's major axis, respectively, and $\alpha(0)$ and $\theta(0)$ are the initial values of these angles. A depiction of θ and α is given in Figure 29. For a two dimensional simulation, the dependence of the recovery on the phase angle is due to membrane elements having a preferred curvature; consequently, a given element of the capsule returns to the same (or opposite, homologous) position it held prior to the deformation and where it was unstressed. If phase angle β is small, then the capsule will recover its shape more quickly than for a larger phase angle. Figure 30 compares the shear recovery of tank-treading capsules with phase angles β of 0.11 and 0.49 radians at the stop of flow for an element initially at the end of the capsule, but identical parameters otherwise. Note that this phase angle helps determine the capsule's angle of inclination after shape recovery. To control for the dependence of the recovery on the phase angle, the ensemble of above simulations were conducted with $\beta = 0.49$ radians for an element initially at the end of the capsule. Thus, two dimensional tank-treading capsules display shape memory, as a trivial consequence of the capsule's explicit preferred curvature.

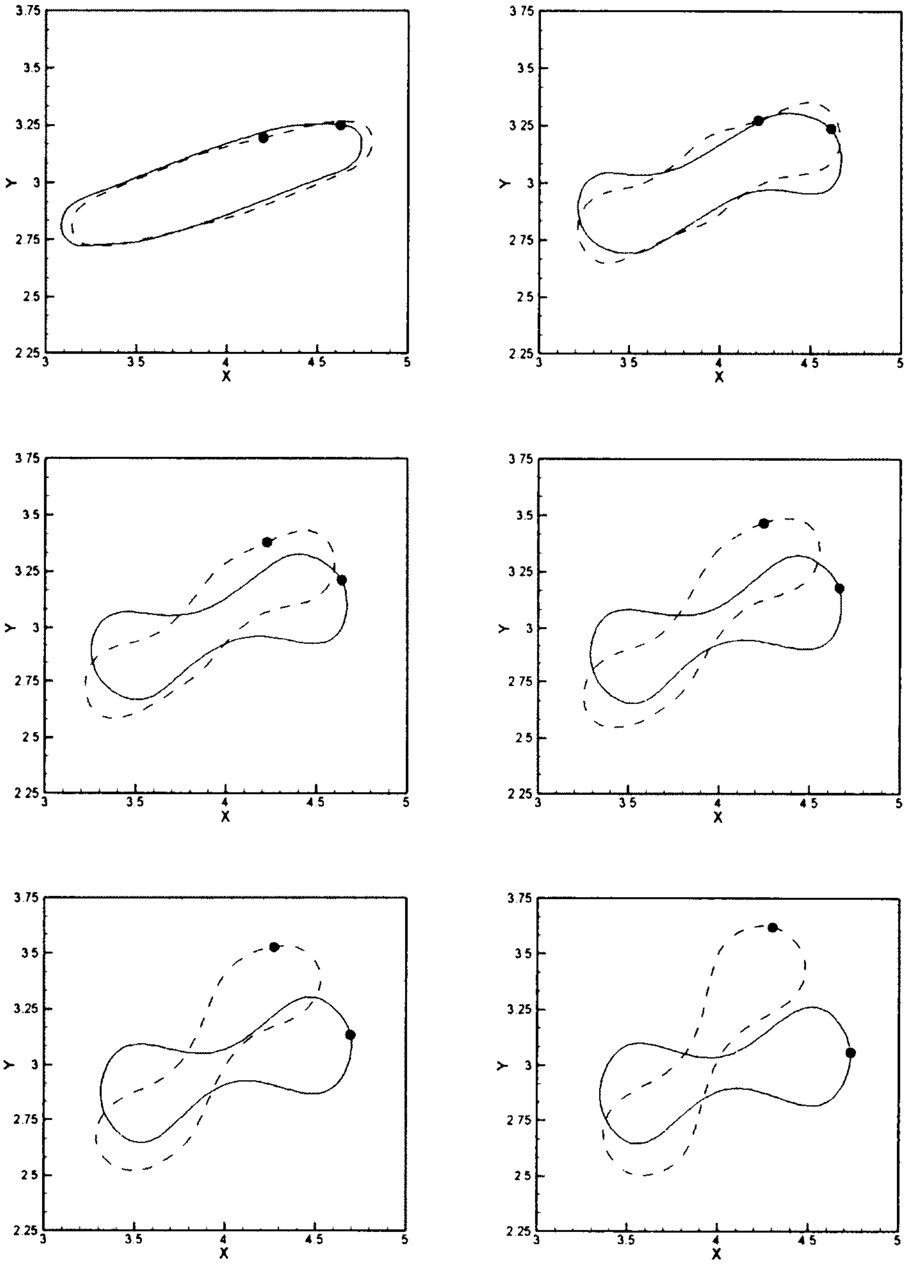

Figure 30. The shape recovery of capsules with phase differences of 0.11 (solid line) and 0.49 (dashed line) radians are compared at times $k^{*}dt = 0$, 12.5, 25, 37.5, 50, and 75 after shear flow is stopped. Circles are the current location of an element initially at the end of both capsules. Order of graphs in time is left-to-right, top-to-bottom.

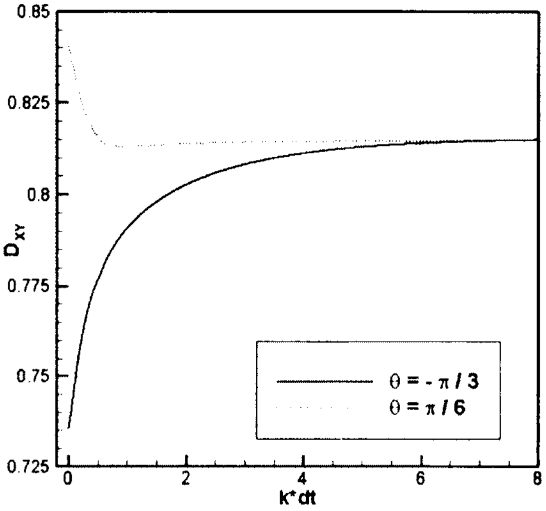

Figure 31. Shape recovery of capsules stopped at angle of inclination $-\frac{\pi}{3}$ (solid line) and $\frac{\pi}{6}$ (dotted line). Capsule parameters are otherwise identical.

4.1.2 TUMBLING CAPSULES

For biconcave capsules whose parameters are such that their steady-state behavior is tumbling, a different course of shape recovery is observed. After shear flow is stopped, the course of shape recovery was such that the Taylor deformation parameter essentially increased or decreased monotonically from $\mathrm{D_{stop}}$ to its initial value, D_∞. Whether decreasing or increasing occurs is determined by the angle of inclination θ of the capsule's major axis when the shear flow is stopped. In Figure 31, the solid and dashed lines depict the capsule's recovery for angles $-\frac{\pi}{3}$ and $\frac{\pi}{6}$, respectively, with identical simulation parameters otherwise. The corresponding capsule shapes are shown in Figure 32. To facilitate comparisons, all following simulations for tumbling capsules were conducted with an angle of $-\frac{\pi}{3}$ when the shear flow is stopped.

Nonetheless, when attempting to describe this recovery by fitting an exponential curve to D_{xy}, it was found that a single exponential decay function failed to adequately describe this recovery. In contrast to tank-treading capsules, in which a qualitative change naturally suggested separating the recovery into two distinct phases, no such intrinsic division was present for a tumbling capsule. Even so, a

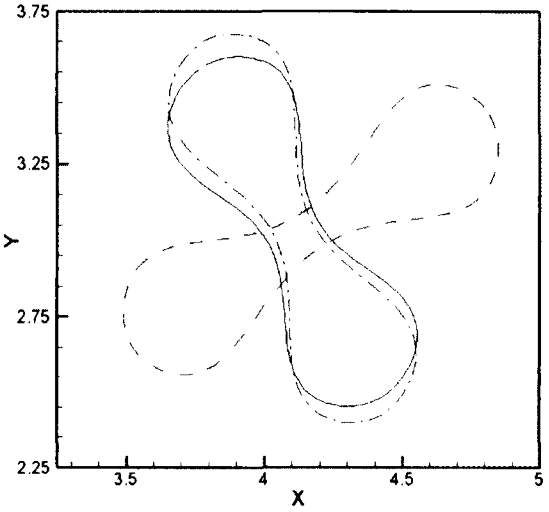

Figure 32. Deformed shapes for $-\frac{\pi}{3}$ and $\frac{\pi}{6}$ at $t = 0$ (solid and dashed lines, respectively) and recovered shapes at $t = 7.5$ (dash-dot and dotted lines, respectively).

quantitative difference between the early and late portions of the shape recovery suggested that modeling the recovery as two phases would be instructive. As a result, a pair of exponential curves are fitted to the recovery of D_{xy}, as

$$D_{xy}(t) = D_{\infty} + \frac{1}{2}\left(\mathrm{D}_{\mathrm{stop}} - D_{\infty}\right)\left(e^{-t/(k\tau_{R1})} + e^{-t/(k\tau_{R2})}\right) \tag{90}$$

over the time interval $[t_{stop}, t_{\infty}]$, with the beginning of the interval reset to $t = 0$. For the range of parameters considered, this model fit the results with a coefficient of correlation $R^2 > 0.97$. In general, the two recovery times differed by one order of magnitude: $k\tau_{R1}$ was $O(10^{-1})$ and $k\tau_{R2}$ was $O(1)$.

The dependence of these recovery times on simulation parameters is considered in Figures 33 — 36. To reflect the aforementioned difference in order of magnitude, recovery times are plotted on differently scaled axes, as with the tank-treading capsules. Most of the relationships noted for a tank-treading capsule remained applicable to tumbling capsules. As with circular and tank-treading biconcave capsules, both recovery times were almost directly proportional to Ca. Similarly, bending stiffness and the fluid viscosity ratio had fairly negligible impacts on $k\tau_{R1}$, but $k\tau_{R2}$ varied directly with V and inversely with E_b. Finally, for the membrane viscosity ratio, both

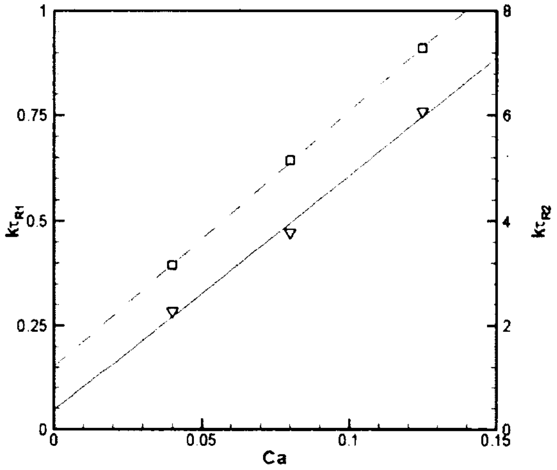

Figure 33. As Ca is varied, data points for $k\tau_{R1}$ and $k\tau_{R2}$ are denoted by gradients (left axis) and circles (right axis), respectively. The approximate parameter relationships with $k\tau_{R1}$ and $k\tau_{R2}$ are represented by solid and dotted lines, respectively. Unvaried parameters are $E_b = 0.05$, $V = 5$, and $\eta = 0$.

recovery times increased modestly with η for the tumbling capsule, though $k\tau_{R1}$ still had a higher dependence on η. With that caveat about the membrane viscosity ratio, the approximations made for tank-treading capsules remain, on a basic level, applicable here: $k\tau_{R1} \sim Ca \cdot \eta$ and $k\tau_{R2} \sim \frac{Ca \cdot V}{E_b}$.

4.1.3 COMPARISON

The courses of shape recovery for tank-treading and tumbling capsules are, ostensibly, quite different. Despite this, there are two obvious parallels in the descriptions of their recovery. First, there seem to be two distinct aspects of the recovery, operating on different timescales. Second, despite the differences in the capsules and in the models, the recovery times for these two phases display very similar dependence on the simulation parameters.

Another lens through which these recoveries may be compared is the decay of membrane tension τ and bending moments m. Figures 37 and 38 compare tension and bending moments during the recovery of tank-treading and tumbling capsules. Both the tension and bending moments are normalized by their values when shear

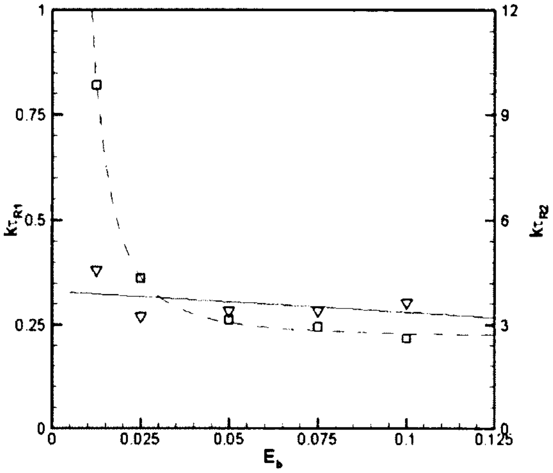

Figure 34. As E_b is varied, data points for $k\tau_{R1}$ and $k\tau_{R2}$ are denoted by gradients (left axis) and circles (right axis), respectively. The approximate parameter relationships with $k\tau_{R1}$ and $k\tau_{R2}$ are represented by solid and dotted lines, respectively. Unvaried parameters are Ca $= 0.4$, $V = 5$, and $\eta = 0$.

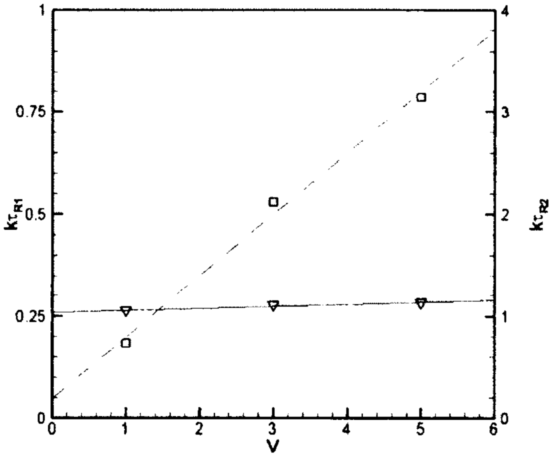

Figure 35. As V is varied, data points for $k\tau_{R1}$ and $k\tau_{R2}$ are denoted by gradients (left axis) and circles (right axis), respectively. The approximate parameter relationships with $k\tau_{R1}$ and $k\tau_{R2}$ are represented by solid and dotted lines, respectively. Unvaried parameters are Ca $= 0.4$, $E_b = 0.05$, and $\eta = 0$.

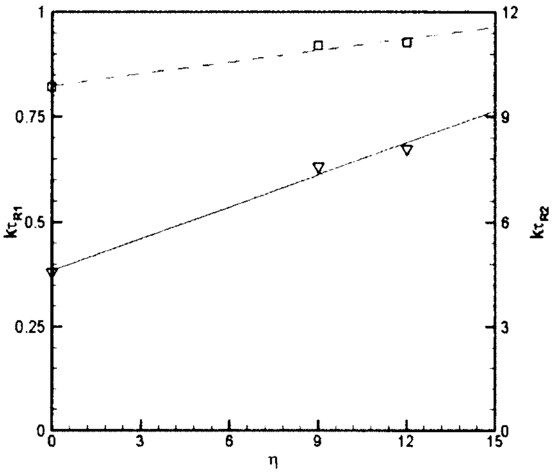

Figure 36. As η is varied, data points for $k\tau_{R1}$ and $k\tau_{R2}$ are denoted by gradients (left axis) and circles (right axis), respectively. The approximate parameter relationships with $k\tau_{R1}$ and $k\tau_{R2}$ are represented by solid and dotted lines, respectively. Unvaried parameters are Ca $= 0.4$, $E_b = 0.0125$, and $V = 5$.

flow is stopped, and plotted against D_{xy}. As the undeformed shape is free of tension and bending moments, so also are capsules that have completed shape recovery.

In Figure 37, for a tank-treading capsule, one may observe that during the initial phase of recovery — when D_{xy} is decreasing — tension τ decreases very rapidly. Indeed, the time periods in which D_{xy} decreases and τ sharply declines end nearly simultaneously. As tension is the result of the membrane's viscoelasticity, it is unsurprising that the viscoelastic parameters determine the characteristic time of the initial recovery phase. The remaining tension, however, is dissipated very slowly during the second phase of recovery. In contrast, bending moment m decreases at a modest rate through both recovery phases. As a result, the dependence on bending stiffness is seen primarily in the longer, latter recovery phase.

For the tumbling capsule considered in Figure 38, there is a similar sharp initial decrease in $k\tau$, which ends near $t = 1$. This matches nicely with the capsule's first recover time, $\tau_{R1} = 0.283$, since the duration of the phase ought to be approximately $3\tau_{R1}$ (since $e^{-3} \approx 0.05$). As with the tank-treading capsule, it is followed by a much slower decline in tension. Further, the bending moment also decreases by nearly

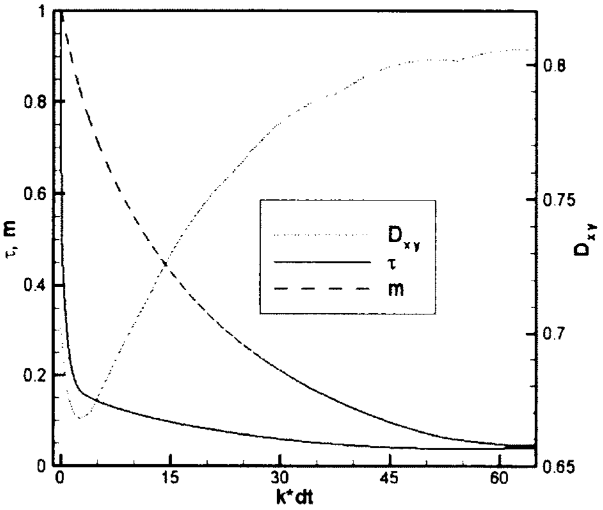

Figure 37. Viscoelastic tension and bending moments during recovery of a tank-treading capsule. Parameters are Ca = 0.067, $E_b = 0.0014$, $V = 1$, and $\eta = 12$.

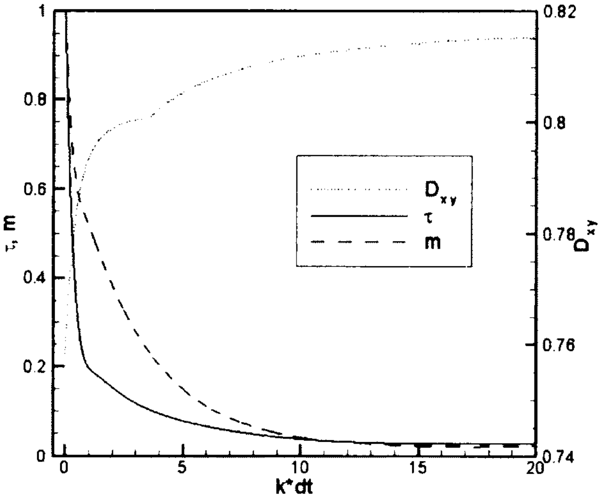

Figure 38. Viscoelastic tension and bending moments during recovery of a tumbling capsule. Parameters are Ca = 0.4, $E_b = 0.05$, $V = 5$, and $\eta = 0$.

50% during this initial phase, before entering a slower decline. The initial rate of the decline in the bending moment m was higher than for tank-treading, which is reasonable since the shape recovery is more rapid as well.

Thus, for both tank-treading and tumbling capsules, the recovery in the Taylor deformation parameter may be described by two phases. The first phase, dominated by viscoelastic dissipation, is brief and does not necessarily involve the capsule becoming more biconcave. The second phase, on the other hand, consists primarily of shape recovery and, along the way, dissipating the remaining stress. This second process is dominated by the capsule's bending stiffness and, indeed, does not occur without it. Nonetheless, the capillary number and fluid viscosity ratio play major roles in determining the time course of the second phase.

4.2 THREE DIMENSIONS

A three dimensional study of biconcave capsule shape recovery is a necessary complement to a two dimensional consideration. Certain matters of interest, such as the roles of simulation parameters in determining the length of the recovery, may be efficiently investigated in two dimensions. However, two important differences between the two and three dimensional models prevent a two dimensional simulation from contributing to the study of a red blood cell's biconcave shape and shape memory. First, as is clear in the earlier part of this chapter, a biconcave capsule in two dimensions will recover its shape and display shape memory if the preferred curvature κ_0 is set to be the initial curvature. In three dimensions, however, Pozrikidis has clearly delineated how a constant curvature preference may lead to a biconcave shape [47]. Second, the three dimensional network of elastic springs is potentially able to support a biconcave shape or cause biconcave shape memory, neither of which are theoretically possible in two dimensions.

The instability of three dimensional capsules in shear flow has been a major issue in previous studies, especially for biconcave shapes, and this problem remains in this work. Without even considering the membrane buckling caused by membrane viscosity [63], an elastic capsule without bending stiffness encounters non-physical buckling in many current models [36, 63, 64, 55]. The clear exception would seem to be Le's thin shell model, which is capable of simulating an elastic capsule without bending stiffness for long times ($k^{*}dt = 60$) [34]. Even with the stabilizing influence of bending stiffness, Yazdani and Bagchi's algorithm was not necessarily stable for more than one period of a biconcave capsule dynamics and deformation [64]. As shape recovery from tank-treading, by necessity, requires long simulations, capsules without bending stiffness are not considered. Specific instances of instability in subsequent simulations are discussed when encountered.

4.2.1 SETUP

Introduced by Helfrich, the spontaneous curvature c_0 is a phenomenological parameter which describes the internal/external asymmetry of the lipid bilayer, as opposed to a specific curvature preference [15]. A bilayer which has inside/outside symmetry has $c_0 = 0$, while positive and negative c_0 indicate spontaneous curvature in the same direction and opposite, respectively, of the mean curvature of a sphere. Analysis of experimental data with Helfrich's model has indicted that the red blood cell shape is consistent with a constant spontaneous curvature $c_0 < 0$ [16]. More recently, Pozrikidis' analysis has suggested that $c_0 \approx -2$ would be most advantageous for causing the sort of biconcavity observed in red blood cells [47]. Yazdani and Bagchi selected $c_0 = -2.09$ in their simulations of biconcave capsules and, in order to avoid needless multiplication of entities, the same value will be considered below [63].

While Deuling and Helfrich suggest that spontaneous curvature may depend on capsule deformation [16], there does not appear to be any biophysical basis for a spatially dependent spontaneous curvature — that is, a spontaneous curvature analogous to the explicit curvature preference in the two dimensional model. Nevertheless, a spatial dependent spontaneous curvature is an intriguing characteristic, as $c_0 = 2\kappa$ would minimize the bending energy functional in Equation (71) (albeit not the force density in Equation (72)).

In Pozrikidis' theory of the undeformed shape of red blood cells, the cytoskeleton is assumed to be unstressed or, at least, nearly unstressed in its undeformed state [47]. Seemingly all computational investigations to date have modeled an unstressed cytoskeleton; that is, the undeformed biconcave elastic configuration is the preferred elastic configuration and, recalling Fischer's terminology from the introduction, the reference shear deformation is non-uniform [25]. The role of the reference shear deformation may be tested by comparing capsules with this non-uniform reference shear deformation to capsules with a uniform reference shear deformation. The uniform reference shear deformation is based on a uniform spherical mesh, with the

Table 1. Ensemble of three dimensional capsule descriptions in terms of reference shear deformation and spontaneous curvature

Description	Reference Shear Deformation	Spontaneous curvature
A	Non-uniform: Biconcave	$c_0 = -2.09$, -1, and 0
B	Non-uniform: Biconcave	$c_0 = 2\kappa$
C	Uniform: Spherical	$c_0 = -2.09$

same surface area as the initial biconcave shape. Additionally, the uniformity of the reference shear deformation means that the capsule will have elastic stress in the initial biconcave shape.

With these thoughts in mind, three possible descriptions of the undeformed biconcave shape of red blood cells are considered. Tabulated in Table 1, they describe whether or how the cytoskeleton or bilayer are stressed in the undeformed configuration. In case A, which aims to describe Pozrikidis' theory, the cytoskeleton has a non-uniform reference shear deformation, but a constant spontaneous curvature c_0 stresses the bilayer. Case B also includes a non-uniform reference shear deformation, but paired with a non-constant spontaneous curvature which minimizes the bending energy functional. Finally, case C considers a negative and constant spontaneous curvature, along with a uniform reference shear deformation.

For each of the three cases, the biconcave capsule is deformed in shear flow. After the capsule reaches steady-state behaviour, the flow is stopped at $t = 15$ and the capsule is allowed to relax. The choice of $t = 15$ as the stop time is determined by two competing factors. The stop time must be late enough for all capsules to have clearly reached steady-state, while still early enough that sufficient time remains for relaxation before numerical instability and mesh degradation adversely affect the results. When considering the relaxation process, two questions are of interest: to what extent does the capsule recover its undeformed shape and, if recovery is observed, do elements of the capsule return to their initial positions? A brief description as to how these two questions are to be answered follows:

Two factors will be necessary to judge whether, or to what extent, a capsule has recovered its undeformed shape. The mapping of Taylor deformation parameters values to the shapes that D_{xy} describes is onto, not one-to-one. Consequently, to determine whether or not the capsule has recovered its shape, a qualitative comparison between initial and current shapes will be made, in addition to tracking whether the Taylor deformation parameter recovers the value for an undeformed capsule, $D_{xy} \approx 0.51$.

Whether capsule elements return to their original positions — and, therefore, the capsule displays shape memory — will be quantified in terms of the phase angles β of the elements of the capsule. Referenced in Equation (89), a more complex definition is necessary in three dimensions. As seen on the left side of Figure 39, the current position of a capsule element Γ is defined by

$$\Gamma = \alpha_{xy} - \theta_{xy} \tag{91}$$

in which α is the inclination angle of the capsule element and θ is the inclination angle of the capsule's major axis, with both of these angles measured with respect to the x-axis and in a plane parallel to the xy-plane. With this definition of capsule position, define the phase angle β of a capsule element as

$$\beta(t) = \Gamma(t) - \Gamma(0) \tag{92}$$

Capsule elements do not undergo significant changes in the z-direction, and so it is sufficient to consider phase angles parallel to the xy-plane. Thus, since $\beta = 0$ for all elements of an undeformed capsule, shape memory requires $\beta \to 0$ for all elements during shape recovery. In the subsequent simulations, the phase angles for five initial positions $\Gamma(0)$ are considered, as depicted on the right side of Figure 39. Since the capsule is symmetric with respect to the origin, a given $\Gamma(0)$ actually has two initial 'positions' on the capsule and, consequently, $\beta \to 0$ if it were to return to either position.

4.2.2 CASE A: NON-UNIFORM REFERENCE SHEAR DEFORMATION & CONSTANT SPONTANEOUS CURVATURE

A capsule with a constant spontaneous curvature and an elastic configuration unstressed in the undeformed biconcave shape is the standard description of a capsule in computational studies. Capsules with spontaneous curvature $c = -2.09$ and bending stiffnesses $E_b = 0.025$ and 0.05 are considered in Figure 40. After shear flow is stopped at $t = 15$, the Taylor deformation parameter declines sharply toward the undeformed value of $D_{xy} \approx 0.51$. However, this decline stops suddenly nearly

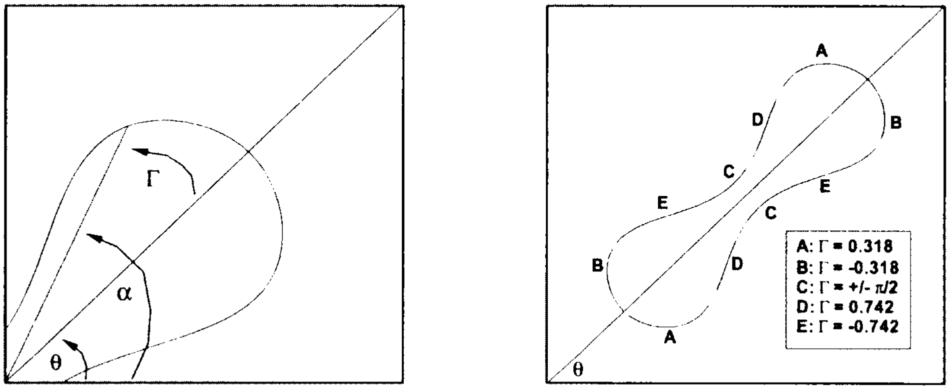

Figure 39. At left, the current position Γ of a capsule element is defined by the difference between the inclination α of the capsule element and inclination θ of the capsule, with these inclinations measured with respect to the x-axis. At right, a range of initial capsule positions Γ are depicted, for an undeformed capsule.

t = 18-19, after which negligible change in $D_{xy} \approx 0.545$ is observed through $t = 40$. Subsequently, numerical instability disrupts the results and no further recovery in D_{xy} is observed.

Considering the capsule shapes themselves helps to demonstrate the limited nature of the recovery observed here. To control for the capsules' time-dependent angles of inclination θ, the capsules are mapped to $\theta = 0$ and the central slices of the capsule parallel to the xy- and yz-planes are extracted. The results are displayed in Figures 41 and 42 for $E_b = 0.05$ and 0.025, respectively. In both cases, it may be observed that the capsule regains its biconcavity during the interval between $t = 15$ and $t = 20$, during which the significant decrease in D_{xy} occurs. In the time that follows, the capsule becomes somewhat more 'biconcave', but not nearly to the extent of the undeformed shape. Thus, while a meaningful change in the Taylor deformation parameter does not occur after $t = 20$, the capsule is still recovering its shape, however slow this process may be. A slight left-to-right asymmetry is also clear, in the slices parallel to the xy-plane: the concavity is skewed to the top right and bottom left of the capsule. This suggests that further tank-treading of the membrane is necessary for a complete shape recovery. On the other hand, in the yz-plane, the

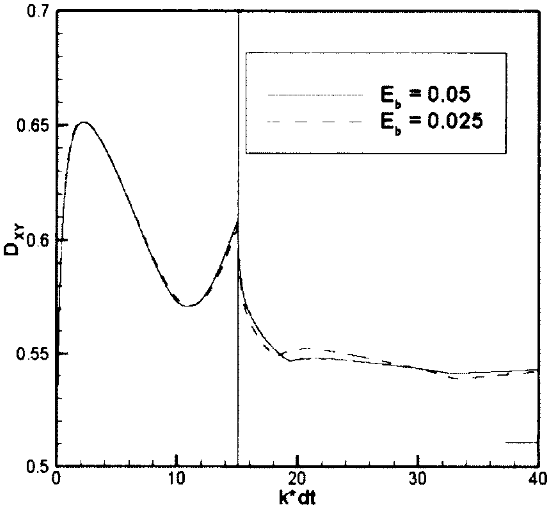

Figure 40. D_{xy} during deformation and recovery for $c_0 = -2.09$. Additional capsule parameters are Ca $= 0.5$, $V = 2$, and $\eta = 0$. Vertical line in this and subsequent Figures indicates the stop of shear flow at $t = 15$.

membrane does have left-to-right symmetry, since the change in the z-direction of capsule elements is minimal during both deformation and recovery.

The incompleteness of the tank-treading process is confirmed by Figure 43, which considers the phase angle β for several elements Γ of each capsule during the recovery process. Observe that for one segment of the membrane, which includes the interval $\Gamma(0) = [-0.742, 0.318]$, the phase angle when shear flow stops is small, with $\beta < 0.5$. The complement of this segment, which includes $\Gamma(0) = [0.742, \pm\frac{\pi}{2}]$, has a much larger phase angle, however. During the recovery process depicted, each phase angle decreases by approximately $40 - 70\%$, though the phase angles for $\Gamma(0) = 0.742$ and $\pm\frac{\pi}{2}$ are still quite large. Recalling the right side of Figure 39, it may be observed that the interval of the membrane containing $\Gamma(0) = 0.742$ and $\pm\frac{\pi}{2}$ is the same section skewed in Figures 41 and 42. Thus, at least part of the incompleteness of the shape recovery may be ascribed to incompleteness of the tank-treading process, which nonetheless is ongoing when the simulation was concluded.

To consider the extent to which the results observed are dependent on the spontaneous curvature $c_0 = -2.09$, simulations with identical parameters and $E_b = 0.05$ are

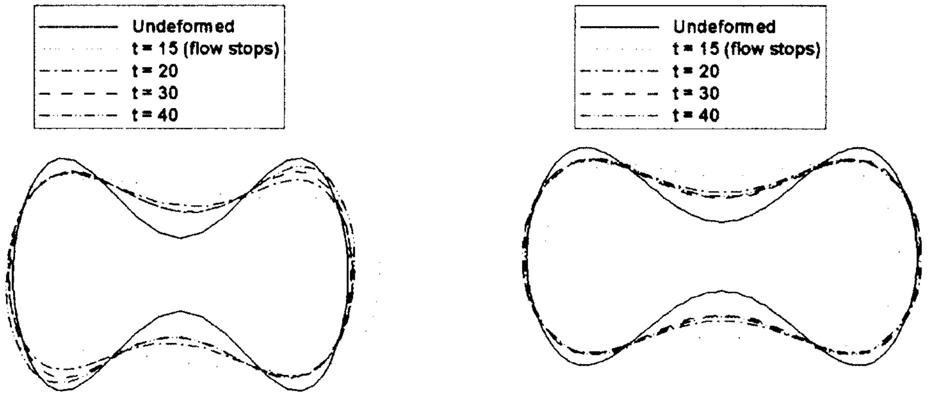

Figure 41. Shape change in xy-plane for $E_b = 0.05$, as shown in Figure 40

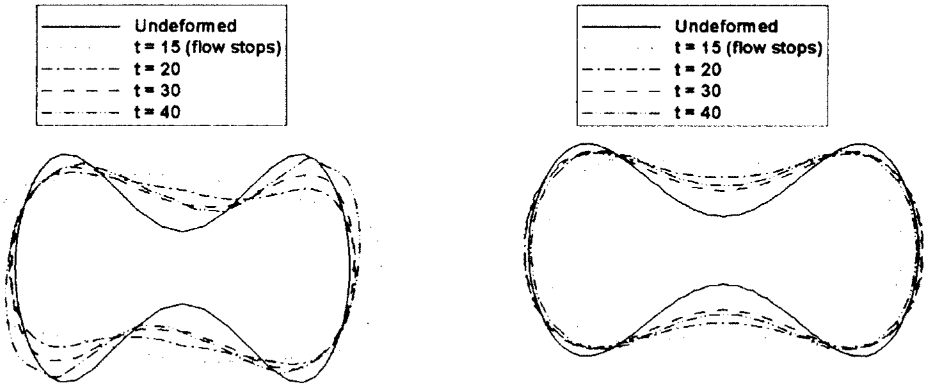

Figure 42. Shape change in xy-plane (left) and yz-plane (right) for $E_b = 0.025$, as shown in Figure 40

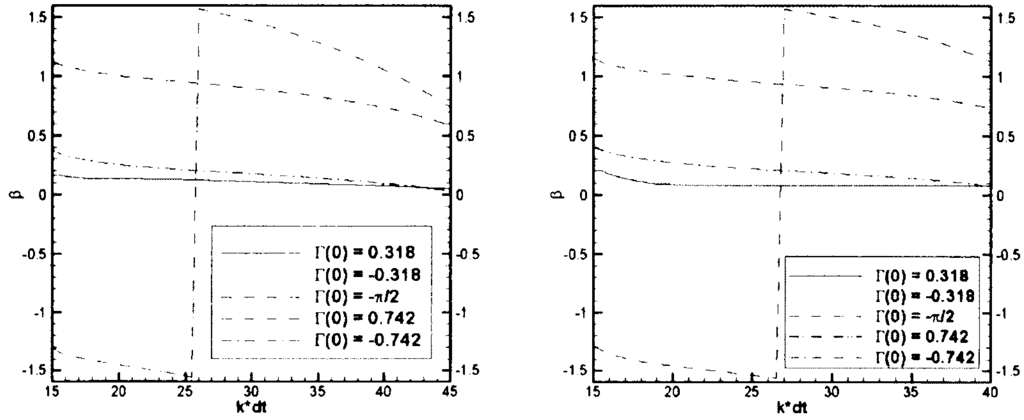

Figure 43. Phase angle β during recovery for $c_0 = -2.09$, for $E_b = 0.05$ (left) and $E_b = 0.025$ (right).

conducted for capsules with $c_0 = 0$ and -1. In Pozrikidis' analysis, such spontaneous curvatures are consistent with an undeformed biconcave shape, but not as felicitous as $c_0 \approx -2$. The shape change for these spontaneous curvatures in terms of D_{xy} is displayed in Figure 44. Both the dynamics in shear flow and the relaxation process after flow stops are nearly identical to $c_0 = -2.09$. D_{xy} decreases to 0.545 by $t =$ 19-20, but does not recover further. Instead, during the period after $t = 20$, the capsule becomes more biconcave, as seen in Figures 45 and 46, but still clearly differs from the undeformed shape. As with $c_0 = -2.09$, numerical instability disrupts results for larger times. Further, the phase angles β depicted in Figure 47 behave similarly to those for $c_0 = -2.09$: all phase angles decline significantly during the period of recovery, but still have some elements with $\beta > 0.5$ at the end of the simulation.

Therefore, it may be concluded that a clear, if incomplete, recovery of the initial biconcave shape has occurred. While much the qualitative character of the initial shape is recovered, the capsules at the end of these simulations are insufficiently biconcave. This insufficient biconcavity is, in turn, the reason that D_{xy} does not attain its initial value since, *ceteris paribus*, a more biconcave capsule will have a lower Taylor deformation parameter. Still, the incomplete recovery in shape is accompanied by a similarly clear movement of capsule elements toward their initial positions, consistent with the capsule displaying shape memory.

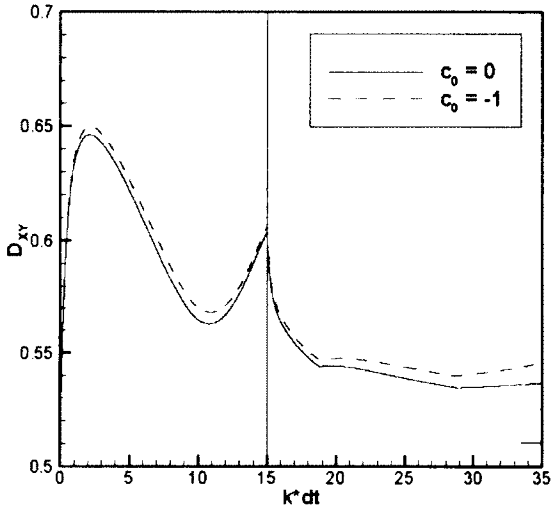

Figure 44. D_{xy} during deformation and recovery for $c_0 = 0$ and $c_0 = -1$.

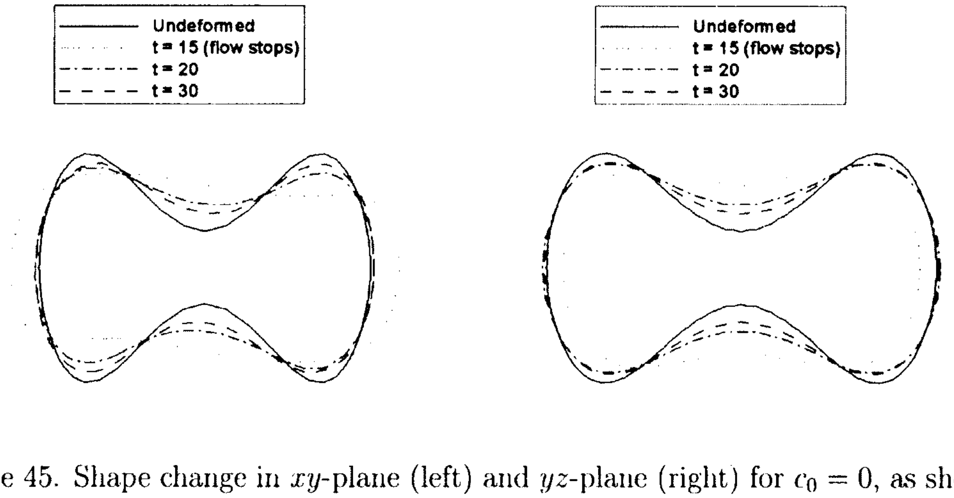

Figure 45. Shape change in xy-plane (left) and yz-plane (right) for $c_0 = 0$, as shown in Figure 44

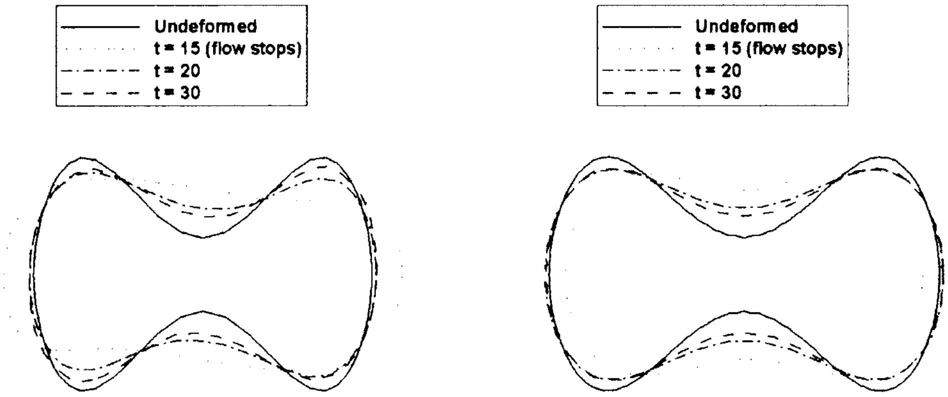

Figure 46. Shape change in xy-plane (left) and yz-plane (right) for $c_0 = -1$, as shown in Figure 44

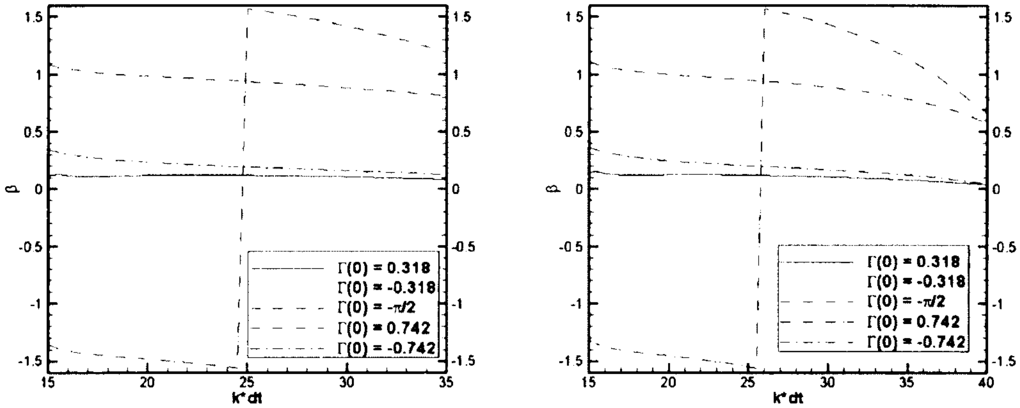

Figure 47. Phase angle β during recovery for $c_0 = 0$ (left) and $c_0 = -1$ (right).

Several causes for the incompleteness of the recovery observed here may be posited. First, and perhaps most obviously, the numerical stability necessary for very long simulations is lacking here. Either or both the fluid grid and the structural mesh may be too coarse, leading to the unphysical numerical instability observed and consequently preventing complete shape recovery. Since the decline of the phase angles $\beta \rightarrow 0$ is ongoing at the end of these simulations, longer stable simulations would presumably lead to more complete shape recovery. Second, other aspects of the numerical implementation may be to blame. For instance, both the local surface area of the capsule and the capsule volume are nearly conserved, varying less than $2-3\%$ from their undeformed values. This may, nonetheless, be too large a deviation and inhibit the subtle shape recovery process. Third, the three dimensional model of the red blood cell may be incomplete, or incorrect. In particular, the membrane viscosity of the capsule was not included in any of these simulations (as the viscoelastic model described in Chapter 3 was restricted to neo-Hookean constitutive laws) and the inclusion of this dissipative mechanism may be necessary for shape recovery. Alternatively, other aspects of the model, such as the bending energy, may not be sufficiently accurate: recall Dueling and Helfrich mentioned that spontaneous curvature may be deformation-dependent [16].

In any event, for the three constant spontaneous curvatures considered, a significant but incomplete shape recovery process occurred. Clear biconcavity was observed, but not to the extent of the undeformed capsule shape. Furthermore, since β decreased in each simulation, each capsule seemed to display the effects of a shape memory. Since the constant spontaneous curvature seems an unlikely cause for membrane elements 'remembering' their initial positions, the capsule's non-uniform reference shear deformation would seem to be the impetus for the shape memory displayed here. To test this hypothesis, it is necessary to compare these results with those for a capsule with a uniform reference shear deformation. This capsule description is considered in Case C.

4.2.3 CASE B: NON-UNIFORM REFERENCE SHEAR DEFORMATION & MINIMIZED BENDING ENERGY

Though lacking a biological basis, minimizing the bending energy by setting $c_0 = 2\kappa$ is an intriguing proposition. Paired with a preferred elastic configuration which is unstressed in the undeformed biconcave shape, it suggests an ideal model. In

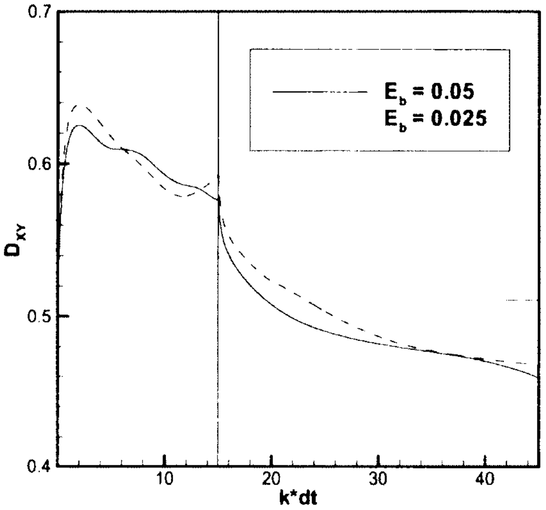

Figure 48. D_{xy} during deformation and recovery for $c_0 = 2\kappa$ with $E_b = 0.05$ and 0.025.

contrast to the case of a constant spontaneous curvature, both the shear elasticity and bending stiffness aspects of the capsule model have the same explicit preferred configuration. One could imagine such a model leading to a fast, clean, and simple shape recovery.

The deformation and relaxation of capsules with $c_0 = 2\kappa$ in terms of D_{xy} is displayed in Figure 48, for $E_b = 0.05$ and 0.025. While the deformation and dynamics in shear flow are not dissimilar from capsules with constant c_0, the relaxation process differs significantly. After flow stops at $t = 15$, D_{xy} declines monotonically, well past the value $D_{xy} \approx 0.51$ for an undeformed capsule. In doing so, the capsule becomes slightly more 'biconcave' than its undeformed shape. The decline of D_{xy} is, initially, somewhat slower for $E_b = 0.025$ than $E_b = 0.05$, but the general trend is quite similar. As with a non-positive constant c_0, the simulation becomes unstable after $t = 42.5$ and further recovery cannot be observed.

During the recovery, particularly for $E_b = 0.05$, the capsule comes very close to recovering its initial shape, as may be observed in Figures 49 and 50. In the capsule slices parallel to the xy-plane, it is clear that the capsule continues to become more

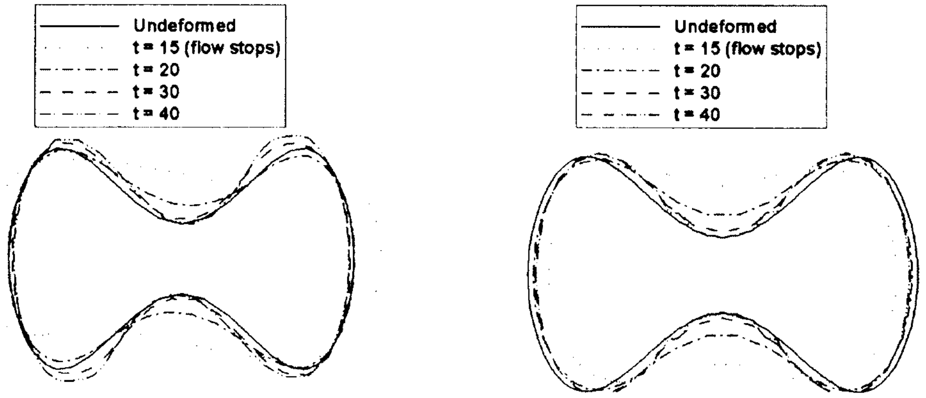

Figure 49. Shape change in xy-plane (left) and yz-plane (right) for $c_0 = 2\kappa$ with $E_b = 0.05$, shown in Figure 48

biconcave, tending away from the undeformed shape. While the bending force density Equation (72) is admittedly not zero in the undeformed biconcave shape for $c_0 = 2\kappa$, it appears that this initial shape is not a stable equilibrium at all.

Further, the capsule displays no indication of shape memory — a surprising result, inasmuch as both elastic and bending energy are minimized by capsule elements being in their initial positions in the initial biconcave shape. As described in Figure 51, the phase angles do change slightly during the recovery, but not significantly enough to indicate any sort of shape memory. Thus, introducing this non-constant spontaneous curvature has the effect of canceling out the shape memory that was observed in Case A, although shape memory in the absence of shape recovery is a somewhat meaningless notion. If nothing else, a constant non-positive spontaneous curvature is seen to be more consistent with both shape memory and shape recovery than is this particular non-constant spontaneous curvature.

4.2.4 CASE C: UNIFORM REFERENCE SHEAR DEFORMATION & CONSTANT SPONTANEOUS CURVATURE

In addition to being interesting in itself (as it does not appear to have been done before), considering a uniform reference shear deformation in concert with a constant

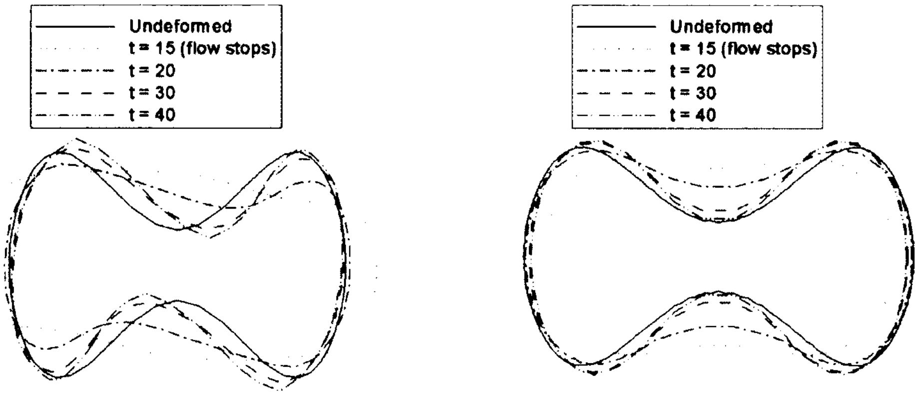

Figure 50. Shape change in xy-plane (left) and yz-plane (right) for $c_0 = 2\kappa$ with $E_b = 0.025$, shown in Figure 48

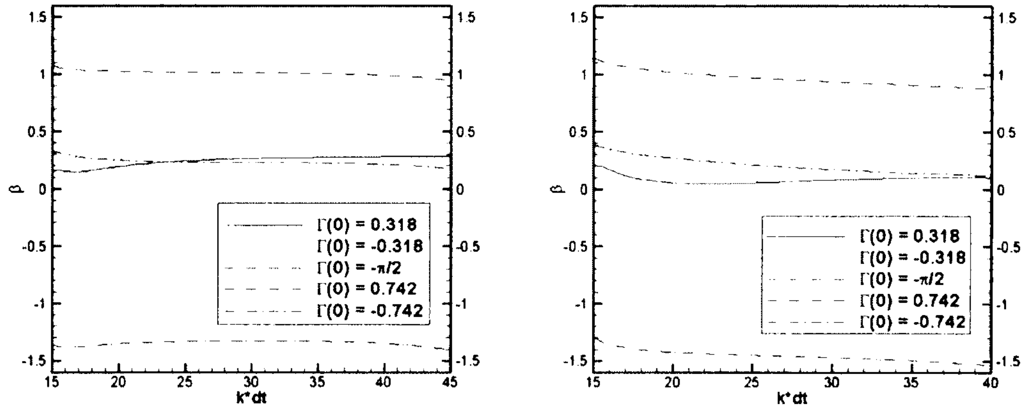

Figure 51. Phase angles β during recovery for $c_0 = 2\kappa$ with $E_b = 0.05$ (left) and 0.025 (right).

spontaneous curvature allows an enlightening comparison with Case A, in which the reference shear deformation was non-uniform. In particular, did the shear elasticity or bending stiffness cause the shape recovery that was observed, and is the preferred elastic configuration solely responsible for the shape memory that was displayed? For the preferred elastic configuration, a spherical elastic configuration is used. This allows for a very uniform reference shear deformation that leads to significant elastic stress in the undeformed biconcave shape. The spherical configuration used has the same surface area as the undeformed biconcave configuration it replaces.

Keeping the same parameters as in Figure 40, with $E_b = 0.05$ and $c_0 = -2.09$, the shape change in terms of D_{xy} is considered in Figure 52. Note that during the deformation in shear flow ($t \leq 15$), the capsule seems to lack the characteristic periodic behaviour typical of three dimensional biconcave capsules in shear flow [34]. This is a predictable result, in that neither the shear elasticity or bending stiffness models have any sort of anisotropic character. Similarly, one would expect comparable behaviour during relaxation: without an anisotropic preference, minimal tank-treading should occur. As a result, one would expect shape recovery to occur as a single process, rather than the two parts observed in Case A.

Indeed, this is largely what the results show: D_{xy} decays monotonically toward the undeformed value and, indeed, gets closer to recovering its initial shape than any capsule in Case A. Further, the capsule slices in Figure 53 do not display the significant left-to-right asymmetry observed for Case A. Instead, the slices of the capsule parallel to the xy- and yz-planes both recovered their biconcavity and continued to approach the initial biconcave shape during the duration of the simulation. While the recovery remains incomplete, the capsule nonetheless has a more complete recovery, despite the additional elastic stress in the initial biconcave shape.

With a uniform reference shear deformation, the capsule's isotropic character implies that a capsule element may take any position on the membrane of the recovered biconcave shape. As a result, there is no need for tank-treading during the recovery process and the phase angles of capsule elements should remain constant. Figure 54 shows that is, indeed, the case: β values for the range of initial capsule positions $\Gamma(0)$ remained basically constant. While some changes are observed, these are consistent with the sort of small changes in inclination angle that occur during the recovery of an triangular element.

These results, when compared with Case A, indicate several broad conclusions.

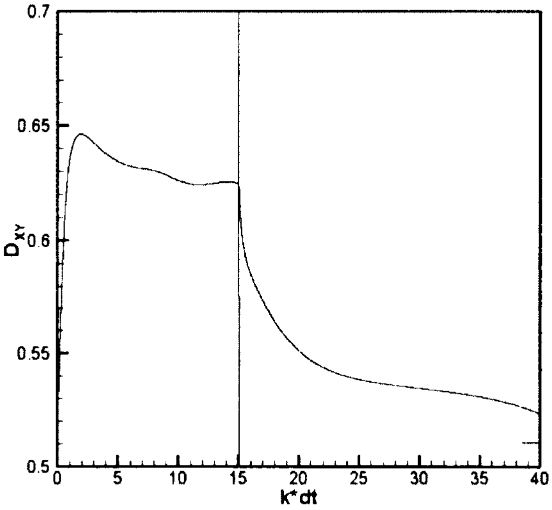

Figure 52. D_{xy} during deformation and recovery for a uniform reference shear deformation and $c_0 = -2.09$

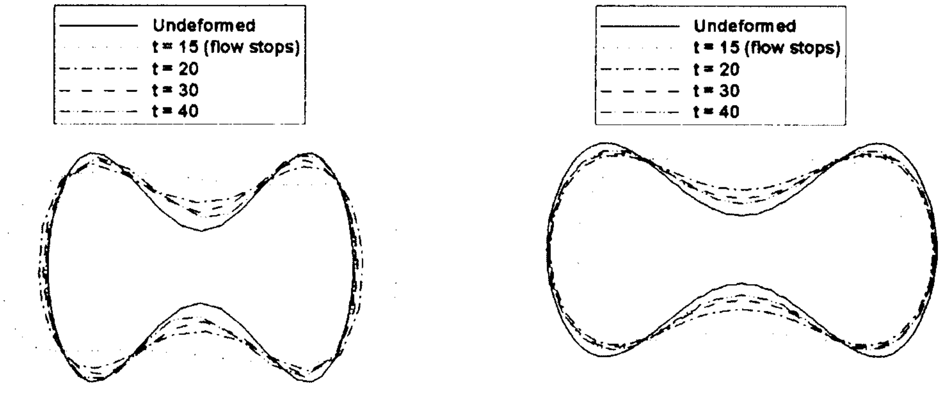

Figure 53. Shape change in xy-plane (left) and yz-plane (right) for a uniform reference shear deformation and $c_0 = -2.09$, as shown in Figure 52

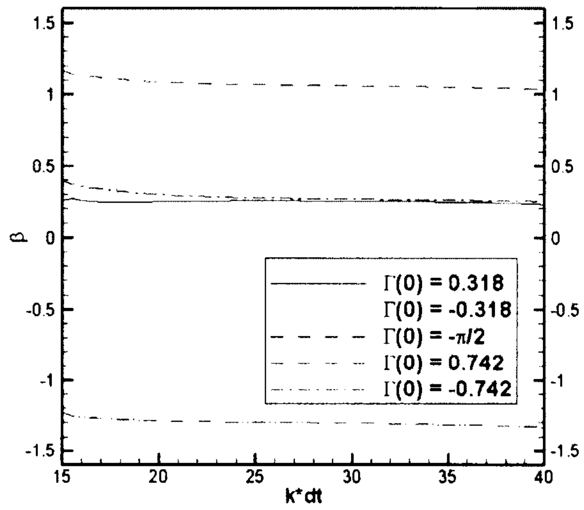

Figure 54. Phase angle β during recovery for a uniform reference shear deformation and $c_0 = -2.09$

First, in this model, the capsule's reference shear deformation looks to be the source of the capsule's shape memory. It may not be necessary that the elastic configuration be unstressed in the resting position, but there must be some non-uniformity in the reference shear deformation. Second, a constant non-positive spontaneous curvature in the range considered would seem to be a sufficient condition for a capsule to recover (at least most of) its undeformed biconcave shape: whether paired with a stressed or unstressed preferred elastic configuration, substantial shape recovery occurred.

Stepping back from the mathematical model to the biological entity on which it is based, one may now speculate about the biomechanical causes of the biconcavity and shape memory of red blood cells. The shape memory which is displayed in the above simulations would seem to have been caused by the capsule's preferred elastic configuration, the biophysical analogue of which is the red blood cell's cytoskeleton. Fischer reached the same conclusion for the cause of shape memory, as he argued that other aspects of the red blood cell membrane simply lack the anisotropy necessary for shape memory [25]. The issue of whether the cytoskeleton or lipid bilayer (or, perhaps, some combination of the two) causes the biconcavity of red blood cells is somewhat murkier, and this consideration makes no pretense of settling the question. What has been established is that a constant negative spontaneous curvature (reflecting the asymmetric character of the lipid bilayer) is sufficient for a capsule to recover biconcavity after tank-treading. This result is, of course, limited by a variety of factors, of which the most significant is the incompleteness of the recovery observed here. However, this result matches a long-standing theory, stretching from Deuling and Helfrich in the 1970s to Pozrikidis in recent years, based on analytical investigations of the resting shapes of red blood cells. Whether this precludes or suggests a role for the cytoskeleton in maintaining the biconcave shape is not altogether clear, and further investigation will be necessary.

4.3 TWO AND THREE DIMENSIONAL COMPARISON

Several important differences prevailed between the shape recovery of biconcave capsules in two and three dimensions. In two dimensions, a clear two-part recovery process was observed for tank-treading capsules. Studying the recovery times showed that two similar phases described the shape recovery of tumbling capsules in two dimensions as well. In the three dimensional simulations, only capsules with tank-treading steady-state behaviour were considered. For these capsules, the incompleteness of the shape recovery observed precludes any conjecture about whether a single or multiple phase(s) are necessary to describe the recovery process. Longer simulations and a more stable methodology will be necessary whether a single or multiple recovery process(es) occur. Further, membrane viscosity ought to be included, in order to determine whether it provides a necessary dissipative mechanism in three dimensional shape recovery.

More clear, however, are the basic mechanisms active in the shape recovery process. In two dimensions, the explicit curvature preference enforced by the bending stiffness accounts for the shape recovery; without an explicit curvature preference, the capsule did not recovery biconcavity. As a one-dimensional elastic (or viscoelastic) mesh in two dimensions does not have any shape preference, the only role played by the viscoelastic configuration in shape recovery was dissipative. Similarly, the shape recovery observed in three dimensions seems to be the consequence of bending stiffness as well. For a constant spontaneous curvature, this is substantiated by the considerable shape recovery observed in Case C, despite the elastic configuration being significantly stressed in the biconcave shape. On the other hand, the supposed analogue of the two dimensional explicit curvature preference — with $c_0 = 2\kappa$ — did not seem to lead to a stable shape, much less the initial biconcave shape.

Conversely, the causes of the shape memory and related tank-treading during shape recovery have different causes in two and three dimensions. In two dimensions, the explicit curvature preference of bending stiffness drives capsule elements to their original positions via tank-treading. The limited shape memory observed in three dimensions, however, was caused by the preferred elastic configuration, at least when paired with a constant spontaneous curvature. Thus, clear differences in the two and three dimensional models have been observed for curvature parameters k_0 and c_0 that lead to shape recovery, and for the bending stiffness and elastic mechanisms responsible for shape memory.

CHAPTER 5

ALTERNATE MODELS OF MEMBRANE VISCOSITY

The results of Puig-de-Morales-Marinkovic *et al.* have caused a paradigm shift in how researchers view the membrane viscosity of red blood cells. Using optical magnetic twisting cytometry to apply a time-dependent (oscillatory) load to the red blood cell membrane, they measured the elastic and frictional moduli at different oscillation frequencies. While the elastic modulus was nearly constant, the frictional modulus increased with the frequency, according to a power law with exponent $n \approx 0.64$. Noting the inconsistency of this observation with solid viscoelastic theory, the lipid bilayer and its viscous character were considered to be the likely mechanism, although the authors suggested other possibilities. Puig-de-Morales-Marinkovic *et al.* conclude that "a power law fluid taken in parallel with a Hookean [elastic] stiffness is an appropriate phenomenological model to describe the dynamic responses of the [red blood cell] in the linear range" [48].

The observed power law response has been rapidly confirmed by subsequent experiments [67, 66, 2, 62] and threatens to invalidate long-standing aspects of red blood cell models. For instance, Puig-de-Morales-Marinkov *et al.* note that the entire concept of measuring characteristic times, a practice begun by Evans and Hochmuth [21] and continued here, becomes meaningless in a power law scheme [48]. Beyond the work of Fedosov *et al.*, however, computational research has lagged behind this development and a deterministic computational power law model does not yet appear to exist. This is perhaps unsurprising, as stable and comprehensive three dimensional viscoelastic models are themselves quite recent: Yazdani and Bagchi's study [63] was only published in 2013.

Instead, since a fluid model has been posited to describe the effects of membrane viscosity, perhaps membrane viscosity could be modeled as a fluid viscosity. The basic idea is not new: Keller and Skalak proposed incorporating the effects of membrane viscosity into their model by artificially altering the fluid viscosity ratio, thereby replacing the viscosity of the membrane with extra fluid viscosity inside of the capsule [30]. The basic plausibility of such an idea has been shown by subsequent computational work: The effects of the fluid and membrane viscosity ratios on the response and recovery times of spherical capsules in Chapter 3 were qualitatively similar. Similarities in the dynamics and deformation caused by these ratios have also been noted in previous studies, for both shear and elongational flows [19, 63]. In all three cases, the solid Kelvin-Voigt model (or an approximation thereof) was used for the membrane viscosity. Even without reference to the power law model, the idea of using an artificial fluid viscosity ratio to simulate membrane viscosity is attractive, given the comparative ease with which non-unity fluid viscosity ratios may be implemented in current computational schemes.

5.1 ARTIFICIAL VISCOSITY MODEL

One way to begin evaluating the equivalence of fluid and membrane viscosity ratios would be to consider the characteristic times of a spherical capsule. In Chapter 3, there seemed to be a natural similarity between them, but whether or not such a comparison is merely superficial is not immediately evident. For instance, an artificial fluid viscosity ratio changes the nature of the fluid, while the forces caused by a solid viscoelastic law alter the velocity of the flow: these are very different aspects of the fluid-structure interaction. To address the depth of this relationship, a few questions suggest themselves: Are these roles of the fluid and membrane viscosity ratios even independent? If so, can a simple relationship be established between them? Finally, could such a relationship be used to establish an efficient computational scheme?

5.1.1 BILINEAR MODEL

The independent roles of the fluid and membrane viscosity ratios in determining response times of a spherical capsule have been noted for elongational flow. Diaz *et al.* found that a bilinear model in η and V sufficed to describe $k\tau_s$, as

$$k\tau_s = a_s(Ca)\eta + b_s(Ca)V + c_s(Ca). \tag{93}$$

with coefficients a_s, b_s, c_s depending on Ca [19]. In particular, for large Ca, they found $a_s \approx b_s$. Diaz *et al.* use these coefficients to posit an artificial fluid viscosity ratio,

$$V^* = V + \frac{a_s}{b_s}\eta, \tag{94}$$

for which an elastic capsule would have the same response time as a viscoelastic capsule. Using such a model, one could theoretically simulate the deformation of

$k\tau$	$a(Ca, E_b)$	$b(Ca, E_b)$	$c(Ca, E_b)$
$k\tau_s(Ca = 0.05, E_b = 0)$	0.0208 ± 0.0039	0.0590 ± 0.0149	0.4158 ± 0.0638
$k\tau_r(Ca = 0.05, E_b = 0)$	0.0534 ± 0.0028	0.2711 ± 0.0109	0.3986 ± 0.0466
$k\tau_s(Ca = 0.05, E_b = 0.025)$	0.0157 ± 0.0039	0.0550 ± 0.0158	0.2567 ± 0.0638
$k\tau_r(Ca = 0.05, E_b = 0.025)$	0.0299 ± 0.0018	0.1380 ± 0.0075	0.2209 ± 0.0303
$k\tau_s(Ca = 0.2, E_b = 0)$	0.0417 ± 0.0110	0.1464 ± 0.0410	0.685 ± 0.1402
$k\tau_r(Ca = 0.2, E_b = 0)$	0.2438 ± 0.0128	1.0120 ± 0.0477	1.614 ± 0.162

Table 2. Coefficients from fitting response and recovery times for a range of viscoelastic capsules using Eqs. (95) and (96). The adjacent ranges are the bounds of a 95% confidence interval.

a capsule with fluid viscosity ratio V and membrane viscosity ratio η by simply simulating a capsule with fluid viscosity ratio V^*.

It would be interesting if a comparable pair of bilinear equations were adequate for both the response and recovery times in shear flow. As this model also incorporates bending stiffness, the coefficients of the bilinear model depend on both the capillary number and bending stiffness. Using the same notation, whether the two models

$$k\tau_s = a_s(Ca, E_b)\eta + b_s(Ca, E_b)V + c_s(Ca, E_b). \tag{95}$$

$$k\tau_r = a_r(Ca, E_b)\eta + b_r(Ca, E_b)V + c_r(Ca, E_b). \tag{96}$$

might fit the data is considered. A successful fit would show the independence of the fluid and membrane viscosity ratios and suggest possible relationships between the two viscosity ratios.

Capsules with Ca = 0.05 and 0.2 are simulated, for a range of η and V using the viscoelastic model, and the characteristic times are calculated. Plausible fits for ensembles with and without bending stiffness are observed, which are charted in Table 2. The model fit very well for $k\tau_r$, with a correlation coefficient $R^2 > 0.99$ for all three cases. The model fit more poorly for $k\tau_s$, with $R^2 \approx 0.91$ for Ca = 0.05 and $E_b = 0$, $R^2 \approx 0.96$ for Ca = 0.05 and $E_b = 0.025$, and $R^2 \approx 0.95$ for Ca = 0.2 and $E_b = 0$. As a result, the accuracy of the coefficients for $k\tau_s$ does not approach that of Diaz *et al.*. Given that they reflect the error from the exponential model fittings being compounded with the bilinear model fitting, these seemed to be acceptable levels of error. A few instructive inferences are apparent from the data:

The coefficients a_s and b_s for $k\tau_s$ and both ensembles with Ca = 0.05 are surprisingly similar, suggesting that their dependence on E_b may be small. More interesting, however, are the ratios $\frac{b_s}{a_s}$ and $\frac{b_r}{a_r}$. Starting from the base ensemble for Ca = 0.05 and $E_b = 0$ with $\frac{b_s}{a_s} \approx 2.8$, the ratio of response coefficients increases to $\frac{b_s}{a_s} \approx 3.5$ with the both addition of bending stiffness $E_b = 0.025$ and the higher capillary number Ca = 0.2. Conversely, the ratio $\frac{b_r}{a_r} \approx 5$ for the base ensemble decreases to $\frac{b_r}{a_r} \approx 4.6$ with the inclusion of bending stiffness $E_b = 0.025$ and falls to $\frac{b_r}{a_r} \approx 4.1$ at the higher capillary number Ca = 0.2. These ratios for the response coefficients do not align with Diaz *et al.*, who observed $\frac{b_s}{a_s} \approx 2$ for Ca = 0.005 and $\frac{b_s}{a_s} \approx 1$ for Ca = 0.05 in elongational flow. Thus, while Diaz *et al.* observe a decrease in the ratio $\frac{b_s}{a_s}$ as Ca becomes larger in elongational flow, a modest increase is observed in shear flow.

5.1.2 ARTIFICIAL V AND η

Such a model may be used in two ways. First, an artificial fluid viscosity ratio V^*, in excess of the actual fluid viscosity ratio V, may be used to simulate the effects of membrane viscosity ratio η. This is accomplished by rearranging Diaz *et al.*'s model, as

$$\eta = \frac{b}{a}(V^* - V). \tag{97}$$

Presuming that the fraction $\frac{b}{a}$ is known *a priori* for the desired Ca and E_b, one can determine an artificial fluid viscosity by which the effects of having a membrane viscosity ratio η may be included. Alternately, an artificial membrane viscosity ratio η may be used to simulate the effects of a fluid viscosity ratio V^* in excess of the actual fluid viscosity ratio V, as

$$V^* = V + \frac{a}{b}\eta, \tag{98}$$

with knowledge of the reciprocal fraction $\frac{a}{b}$. In either case, the upshot is that one may simulate both a particular fluid ratio and a particular membrane viscosity ratio with a single algorithm. Either a membrane viscosity method or a method for non-unity fluid viscosity ratios would be necessary to do this, but one would not need both.

To consider whether these models fit sufficiently well to satisfy and extend Diaz *et al.*'s hypothesis, a comparison is made between the response and recovery times of the Kelvin-Voigt viscoelasticity model and the artificial fluid viscosity ratio model.

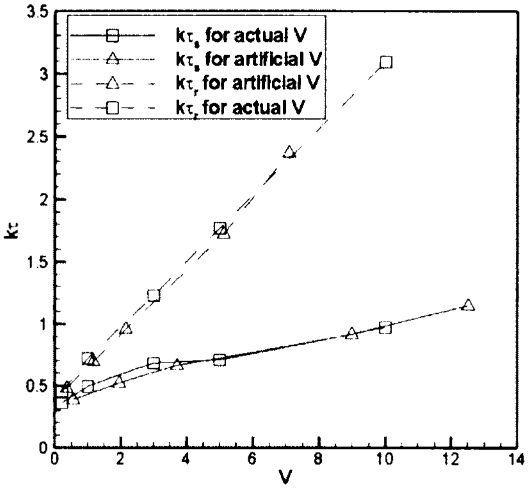

Figure 55. For a spherical capsule without bending stiffness, characteristic times $k\tau_s$ (solid lines) and $k\tau_r$ (dotted lines) for actual fluid viscosity ratios (squares) and artificially calculated fluid viscosity ratios (triangles). The capillary number is Ca = 0.05.

First, an artificial membrane viscosity ratio η is used to simulate the effects of a different fluid viscosity ratio V^*, as in Equation (98). In Figure 55, square data points depict the characteristic times of capsules with Ca = 0.05, $E_b = 0$, and $\eta = 0$, plotted against their different fluid viscosity ratios V. In contrast, the triangular data points are the characteristic times of capsules with identical Ca and E_b, but with $V = 0.2$ and various η. The x-axis values for these triangular data points are V^* in Equation (98), derived by plugging in $V = 0.2$ and the particular value of η. The same methodology is used in Figure 56, in which square data points represent characteristic times for Ca = 0.05, $E_b = 0.025$, and $\eta = 0$, with various fluid viscosity ratios. On the other hand, the triangular data comes from the characteristic times of capsules with the same Ca and E_b, but $V = 1$ and different values of η. In both cases, the derived relationship between V and τ_r matches very well. The results for τ_s are still acceptable, but noticeably poorer. This is unsurprising, given the exponential fittings for τ_s, particularly at large V and η, were much poorer than for τ_r.

Second, the same results may also be viewed through the lens of the membrane

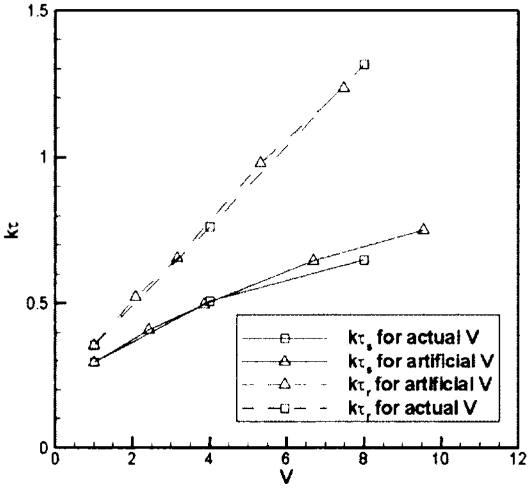

Figure 56. For a spherical capsule with bending stiffness, characteristic times $k\tau_s$ (solid lines) and $k\tau_r$ (dotted lines) for actual fluid viscosity ratios (squares) and artificially calculated fluid viscosity ratios (triangles). The capillary number is Ca = 0.05.

viscosity ratio. In Figures 57 and 58, square data points are characteristic times of capsules plotted against their membrane viscosity ratios η. In Figure 57, the constant parameters are Ca = 0.05, $E_b = 0$, and $V = 0.2$, while the unvaried parameters are Ca = 0.05, $E_b = 0.025$, and $V = 1$ for Figure 58. Triangular data points, on the other hand, originate in capsules with the same Ca and E_b values, but have $\eta = 0$ and various fluid viscosity ratios V^*. In these cases, the "extra" fluid viscosity $V^* - V$ is used to determine the artificial membrane viscosity η, using Equation (97), which provides their x-axis values.

5.1.3 MODEL VIABILITY

Of course, several major caveats to the artificial viscosity model proposed here are evident. First, the methodology is only useful *a posteriori*. One needs to know the coefficients a and b *a priori*. As these coefficients vary with E_b and Ca, this is a substantial requirement. Second, and more importantly, the ratio of the a and b coefficients differs for τ_s and τ_r. As a result, one could not accurately simulate

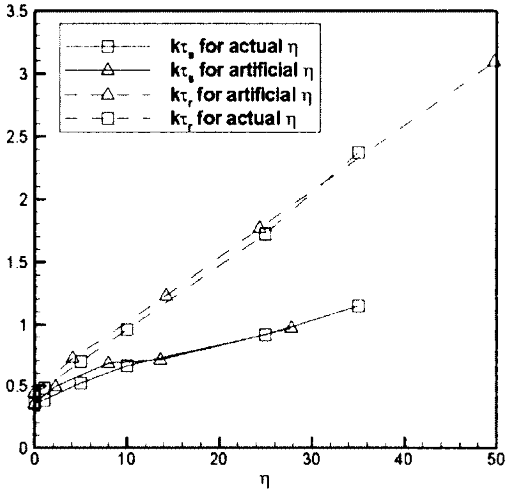

Figure 57. For a capsule without bending stiffness, characteristic times $k\tau_s$ (solid lines) and $k\tau_r$ (dotted lines) for actual membrane viscosity ratios (squares) and artificially calculated membrane viscosity ratios (triangles). The capillary number is Ca = 0.05.

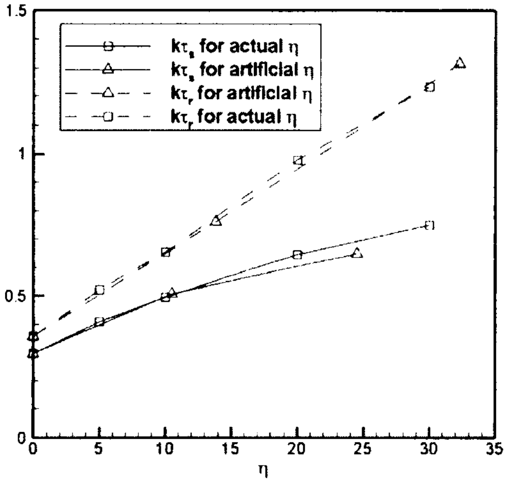

Figure 58. For a capsule with bending stiffness, characteristic times $k\tau_s$ (solid lines) and $k\tau_r$ (dotted lines) for actual membrane viscosity ratios (squares) and artificially calculated membrane viscosity ratios (triangles). The capillary number is Ca = 0.05.

both response and recovery phases with the same ratio in one model. Third, while the effective fluid and membrane viscosity ratios may ensure that the characteristic times are sufficiently accurate, this does not imply that local or global aspects of capsule deformation (much less capsule dynamics) are equal. Indeed, Diaz *et al.* show that, even in elongational flow, local stretching of elements of the capsule will differ somewhat for two different configurations with the same τ_s [19].

Interestingly, Yazdani and Bagchi have suggested a comparable model for simulating membrane viscosity as an artificial viscosity ratio. In their formulation, $V^* = V + \phi$, in which ϕ is the ratio of dissipation in the membrane to the dissipation inside the capsule [63]. Yazdani and Bagchi show that this approach is effective in recovering a spherical capsule's tank-treading frequency. Their result is particularly promising, in that it deals more with capsule dynamics than the capsule shape changes considered here. Ideally, a model for replacing membrane viscosity with an artificial fluid viscosity ratio would reasonably describe both dynamics and shape changes.

In conclusion, the influence of the fluid and membrane viscosity ratios on a capsule's characteristic times are effectively independent, as they fit a basic bilinear model. Further, a sufficiently exact relationship may be defined that an artificial fluid viscosity ratio may be used to simulate membrane viscosity and vice versa. These results serve as proof-of-concept for the notion that membrane viscosity may be reinterpreted as fluid viscosity, while still maintaining the essential aspects of its role in the shape change of a capsule. However, basing a methodology for implementing membrane viscosity using an artificial viscosity method would require compromise between $\frac{b_s}{a_s}$ and $\frac{b_r}{a_r}$, in addition to a prohibitive amount of *a priori* data. On the other hand, in a multiscale framework or a large simulation of many capsules, it may be sufficient to simply take membrane viscosity into account and an artificial fluid viscosity ratio may be an efficient avenue for doing this.

5.2 POWER LAW MODEL

With the viability of using fluid viscosity to simulate the viscosity of the membrane having been shown, a more accurate and extensible methodology based on this idea may be designed. Rather than relying on an unchanging alteration of the fluid viscosity ratio, the viscosity of each element of the zero-thickness membrane is calculated at each timestep using a power law fluid model. Such a model is capable of either Newtonian independence of, or non-Newtonian dependence on, the local rate of deformation tensor (also denoted as the strain rate tensor). The viscosity on each element of the membrane may then be distributed to nearby fluid nodes by using the immersed boundary method and added to the actual fluid viscosity at those nodes. In this way, the viscosity of the membrane is translated into additional fluid viscosity in the nearby nodes, but with the necessary temporal and spatial dependence that is lacking in the artificial viscosity model.

A power law model for membrane viscosity, interpreting membrane viscosity as a fluid viscosity, has several potential advantages over conventional solid viscoelastic models. First, using a power law improves the modeling framework's fidelity to the current understanding of red blood cell membranes. Whatever the power law model's other drawbacks, it presents an opportunity not available to solid viscoelastic models. Second, membrane viscosity described by a solid viscoelastic model has been shown to cause buckling and wrinkling during capsule deformation, particularly in capsules without bending stiffness [63]. It is not yet certain that a biological basis for this particular buckling and wrinkling exists. However, a power law model transfers this instability in the membrane to the robustly stable lattice Boltzmann method. Third, a power law model is governed by two parameters — the flow consistency index, describing the membrane's viscosity independent of space and time, and flow behaviour index, which determines the non-Newtonian character (or lack thereof) of the viscosity. As opposed to the single membrane viscosity coefficient in the Kelvin-Voigt model, this enhances the flexibility of the model.

The implementation of this approach is as follows: first, the velocity gradient $\nabla \mathbf{u}$ of the fluid is calculated in the region containing the capsule, using a second order centered difference method. Second, using the discrete delta function, the velocity gradient $\nabla \mathbf{U}$ is determined at each node $\mathbf{X}_c$ on the capsule, as

$$\nabla \mathbf{U}(\mathbf{X}_c) = \sum_j \delta_h(\mathbf{X}_c - \mathbf{x}_j) \nabla \mathbf{u}(\mathbf{x}_j) h^3. \tag{99}$$

Subsequently, the rate of deformation tensor $\mathbb{D}$ is derived as the symmetric part of $\nabla \mathbf{U}$ in the plane of the interface, as

$$\mathbb{D} = \frac{1}{2} \mathbf{P}_{\text{surf}} \Big(\nabla \mathbf{U} + (\nabla \mathbf{U})^T \Big) \mathbf{P}_{\text{surf}} \tag{100}$$

with projection matrix $\mathbf{P}_{\text{surf}} = \mathbf{I} - \mathbf{nn}$, where $\hat{\mathbf{n}}$ is the outward normal vector [6]. For simplicity's sake, the dependence of membrane viscosity on surface area dilation is ignored, although the method could be extended to include it. Then, the shear rate is

$$\gamma = \sqrt{2\,\mathrm{tr}(\mathbb{D}^2)} \tag{101}$$

and the membrane viscosity μ_{mem} of the capsule element is given by the power law

$$\mu_{\text{mem}} = K\gamma^{n-1}, \tag{102}$$

for flow consistency index K and flow behaviour index n [17]. For a Newtonian fluid, $n = 1$ and K is simply the dynamic viscosity. Values of $n > 1$ and $n < 1$ correspond to non-Newtonian shear-thickening and shear-thinning (pseudoplastic) fluids, respectively. The membrane's viscosity is distributed to nearby fluid nodes by again using the discrete delta function, as

$$\mu_{\text{mem}}(\mathbf{x}_j) = \sum_c \delta_h(\mathbf{X}_c - \mathbf{x}_j)\,\mu_{\text{mem}}(\mathbf{X}_c)\frac{\mathrm{a}_{\text{vor}}}{h}, \tag{103}$$

using the Voronoi area a_{vor} about $\mathbf{X}_c$ and scaling by spatial step h. Then, at each fluid node, the fluid and membrane viscosities are added:

$$\mu(\mathbf{x}) = \mu_{fluid}(\mathbf{x}) + \mu_{\text{mem}}(\mathbf{x}). \tag{104}$$

Based on μ, the relaxation parameters $\mathbf{s}$ at $\mathbf{x}$ may be appropriately updated, according to Section 2.1. A convergence analysis in Figure 59 shows this power law method for incorporating membrane viscosity is independent of the Lagrangian grid, with the accuracy of the coarser grid only suffering as the capsule arrives at the equilibrium deformation.

Among the drawbacks of a power law model, it does increase computational cost somewhat, at least in the following implementation, due largely to the calculation of the velocity gradient. Another potential additional cost — updating the viscosity and relaxation parameters at fluid nodes near the interface — does not present a problem in this implementation, as such an update is already being made (see Section 2.2).

5.2.1 SHEAR FLOW

Of immediate interest is whether the deformation in shear flow of a spherical capsule with membrane viscosity described by the power law model is qualitatively similar to capsules with Kelvin-Voigt viscoelasticity. Selecting a small flow consistency index $K = 0.01\mu_a$, the flow behaviour index n is varied in Figures 60 and 61.

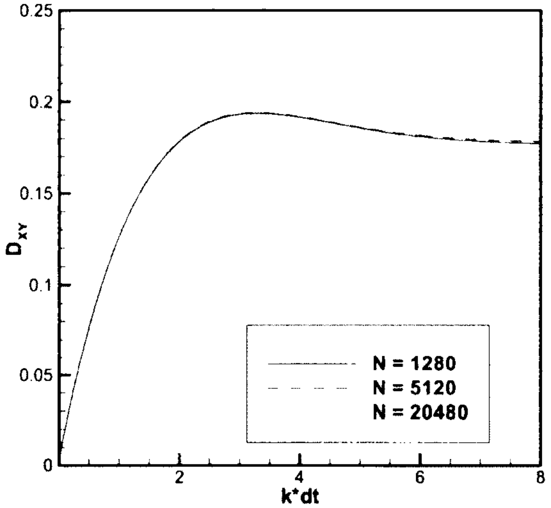

Figure 59. Convergence analysis of the power law model with capsule meshes having $N = 1280$, 5120, and 20480 triangles. Capsule parameters are Ca = 0.05, $E_b = 0$, $V = 1$, $K = 0.1\mu_a$, and $n = 0.64$.

Perhaps surprisingly, the results are simple and intuitive. The spherical capsule is deformed to an (eventually) stable ellipsoidal shape, described by an approximately constant D_{xy}. As n decreases from one toward zero, the membrane viscosity increases and capsule deformation is restricted. Additionally, decreasing n changes the capsule's behaviour from stationary tank-treading to undergoing damped oscillations prior to tank-treading. For these cases with small n, the Taylor deformation parameter oscillates before reaching equilibrium and these oscillations decay more slowly for smaller values of n. All three of these observations agree with those made by Yazdani and Bagchi using Kelvin-Voigt viscoelasticity [63]. Thus, it seems that the dependence of the membrane viscosity on the shear rate γ in the power law model does not appear to produce significant qualitative alterations in the deformation or behaviour of a spherical capsule.

If the two models have qualitatively similar results, how do they compare quantitatively? Capsules with Kelvin-Voigt viscoelasticity are shown in Figures 62 and 63 for $\mu_s = 10$, 20, and 50 times ambient fluid viscosity μ_a. Alongside are shown capsules with membrane viscosity described by the power law model, for $K = 0.01$, 0.02,

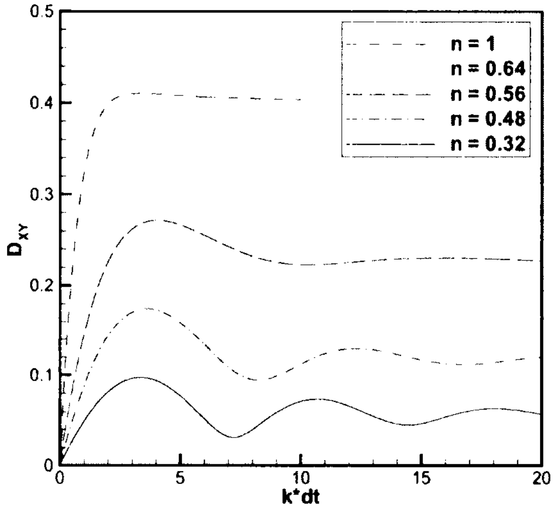

Figure 60. Taylor deformation parameter D_{xy} for $K = 0.01\mu_a$, with $n = 1$ (dashed), $n = 0.64$ (dotted), $n = 0.56$ (long dash), $n = 0.48$ (dash-dot), and $n = 0.32$ (solid). Other capsule parameters are $\mathrm{Ca} = 0.1$, $E_b = 0$, and $V = 1$.

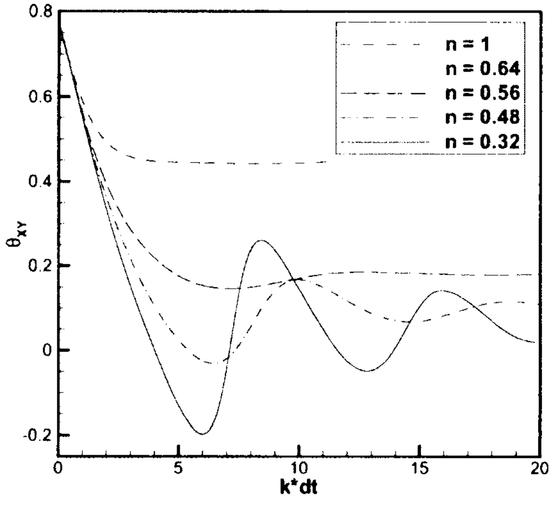

Figure 61. Angle of inclination θ in the xy-plane for $K = 0.01\mu_a$, with $n = 1$ (dashed), $n = 0.64$ (dotted), $n = 0.56$ (long dash), $n = 0.48$ (dash-dot), and $n = 0.32$ (solid).

and 0.05 times μ_a, and all having $n = 0.64$. All other parameters in the two models — Ca = 0.05, $E_b = 0$, and $V = 1$ — are identical. This particular comparison is instructive because the membrane viscosity parameters selected are comparable with those of a red blood cell. For the power law, Puig-de-Morales-Marinkovic *et al.* found $n = 0.64$ in their experiments [48]. Estimates of μ_s vary substantially, as they typically involve assuming that a Kelvin-Voigt model describes a particular phenomena and deriving μ_s from their results [21]. In any event, $\mu_s = 10\mu_a$ (i.e., $\eta = 10$) is considered an approximate value [63].

For each pair with $\mu_s = 1000K$, the initial deformation measured by D_{xy} is nearly identical. For larger times, both D_{xy} and angle of inclination θ diverge somewhat as they approach steady-state. In all three cases, the power law model leads to slightly smaller deformations and smaller angles of inclinations than does Kelvin-Voigt. This divergence at steady-state is reasonable. As the capsule approaches equilibrium, viscous stress in the Kelvin-Voigt model becomes negligible. In contrast, since $n < 1$, the viscous effects created by the power law rise as γ becomes small and remain as it stays small. Consequently, there is a decrease in D_{xy} as the capsule arrives at its steady-state deformation. However, the general dynamic behaviour between the models remains strikingly similar, with both models transitioning from tank-treading to damped oscillations for larger μ_s and K.

This agreement between Kelvin-Voigt and power law models suggests that, frankly, the time-dependence of the power law viscosity has little effect on deformation in shear flow. One might have anticipated that $n \neq 1$ might amplify the time-dependence of γ, leading to qualitatively different, non-linear changes than varying K. Yet, as can be seen in Figure 64, the range of γ values on the capsule changes little, whether during deformation or after achieving steady-state. This lack of substantial variability on the part of γ has a further effect: changes to n and K have qualitatively similar results. As seen in Figure 65, increasing K produces the same results for Newtonian ($n = 1$) membrane viscosity in the power law model as are observed for $K = 0.01\mu_a$ and the non-Newtonian $n = 0.64$. Thus, similar equivalent deformations are observed, with and without dependence on γ. Since the power law model is, therefore, acting like a linear Newtonian model in shear flow, it is unsurprising that it should agree well with the linear Kelvin-Voigt model for small deformations.

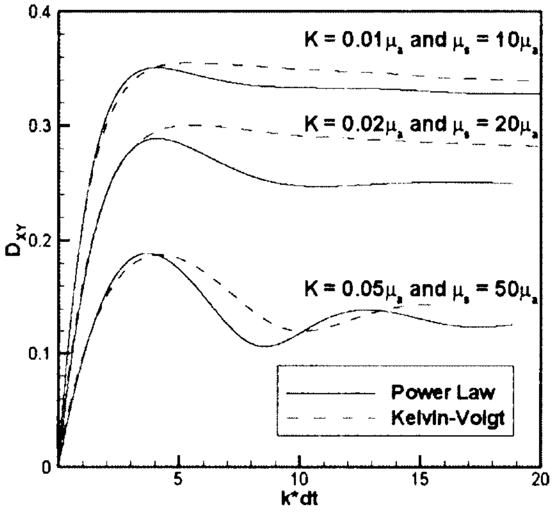

Figure 62. Taylor deformation parameter D_{xy} for μ_s = 10, 20, and 50 times μ_a (dotted lines) and K = 0.01, 0.02, and 0.05 times μ_a (solid lines). Other capsule parameters are Ca = 0.1, $E_b = 0$, and $V = 1$.

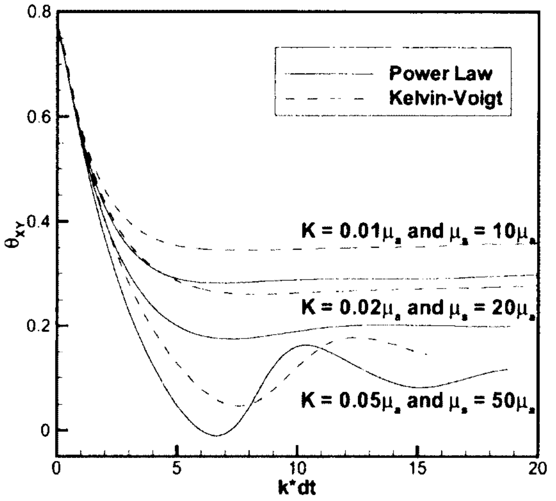

Figure 63. Angle of inclination θ in the xy-plane for μ_s = 10, 20, and 50 times μ_a (dotted lines) and $K = 0.01$, 0.02, and 0.05 times μ_a (solid lines).

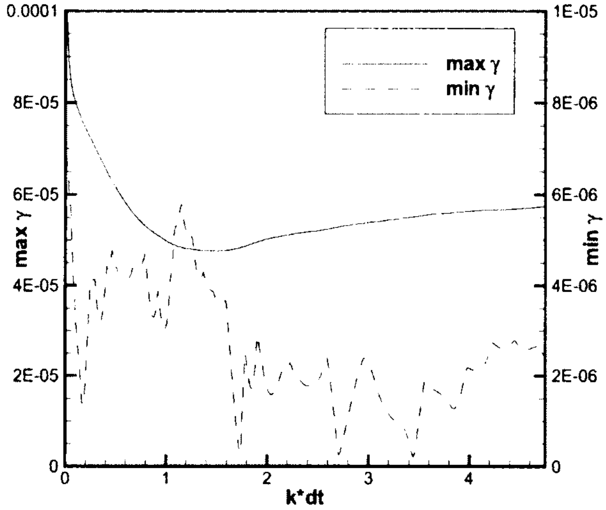

Figure 64. Maximum and minimum values of γ on sphere in the power law model. Parameters are Ca $= 0.1$, $E_b = 0$, $V = 1$, $K = 0.1\mu_a$, and $n = 0.64$.

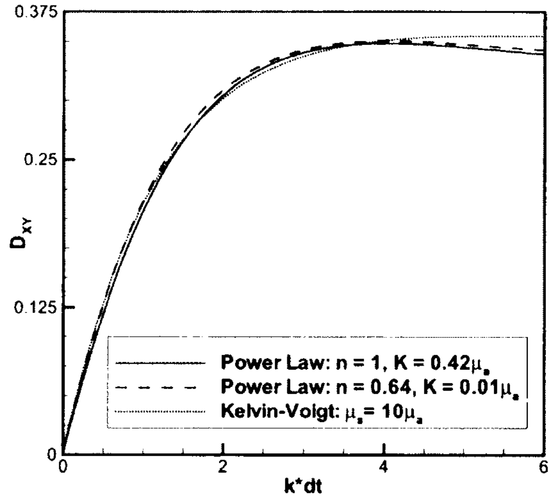

Figure 65. Relative effects of n and K on the capsule deformation. Other parameters are Ca $= 0.1$, $E_b = 0$, and $V = 1$.

5.2.2 OSCILLATORY SHEAR FLOW

Puig-de-Morales-Marinkovic *et al.*'s experimental observations which necessitated a power law model for red blood cells occur in an oscillatory magnetic field, the frequency of which was varied by several orders of magnitude. While the inclusion of electric or magnetic fields is beyond the scope of this consideration, an oscillatory flow is not. Thus, if γ for shear flow is too well-behaved for non-linear effects to occur, one wonders if oscillatory shear flow might be an appropriate venue for such observations. The deformation and dynamics of elastic capsules in an oscillatory shear flow has been explored computationally by Zhao and Bagchi, but their results did not take into account membrane viscosity [70]. In the same experimental setup as with shear flow, capsules with membrane viscosity described by the Kelvin-Voigt and power law models are placed in the center of an oscillatory shear flow. For a simulation domain of $[0, H]^3$, we defined the velocity at $y = 0$ and $y = H$ as $u = \pm\frac{H}{2}k\sin\left(\frac{\pi t}{T}\right)$, for period T.

The same trio of capsules which led to roughly equivalent initial deformations in shear flow are considered here: the Kelvin-Voigt model with $\mu_s = 10\mu_a$, the power law model with $n = 1$ and $K = 0.42\mu_a$, and the power law model with $n = 0.64$ and $K = 0.01\mu_a$. The oscillation has period $T = 4$ and the first three periods are shown in Figure 66. Once again, the initial deformation measured by the Taylor deformation parameter agrees very well for all three capsules. However, since the steady-state behaviour involves continual shape change, this general agreement remains for the duration of the simulation, in contrast to the results in shear flow. Indeed, the only differences appear when the direction of flow changes, as the power law model with $n = 1$ is consistently less deformed than its counterparts, which continue to agree astonishingly well.

On a qualitative level, all three methods have equal responses to flows in both directions, after reaching equilibrium. Further, the three models stay approximately within phase. These general results are consistent with the findings of Zhao and Bagchi for spherical capsules without membrane viscosity [70]: the deformation of the capsule is periodic with the flow and the response to flow from either direction is equal after the capsule reaches equilibrium behaviour. Figure 67 displays the maximum shear rate observed on the sphere. as a function of the fluid velocity $u(t)$ at $y = H$, for a single period after the capsule has reached steady-state behaviour. At this modest oscillation frequency, γ changes by a factor of $6 - 8$ over a period,

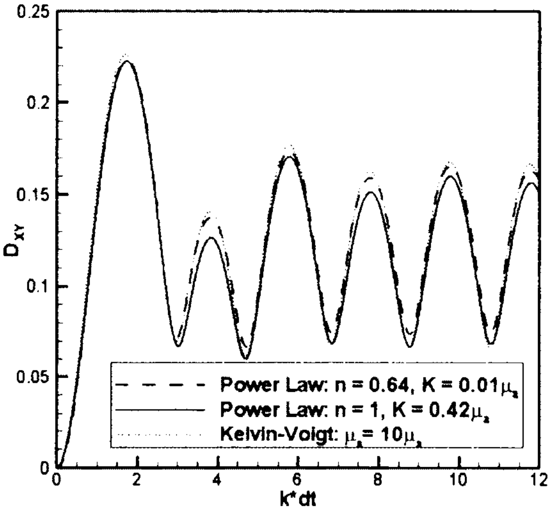

Figure 66. Deformation measured by D_{xy} for ensemble of capsules with membrane viscosity from Kelvin-Voigt and power law models in an oscillatory shear flow. Other parameters are $\mathrm{Ca} = 0.1$, $E_b = 0$, and $V = 1$.

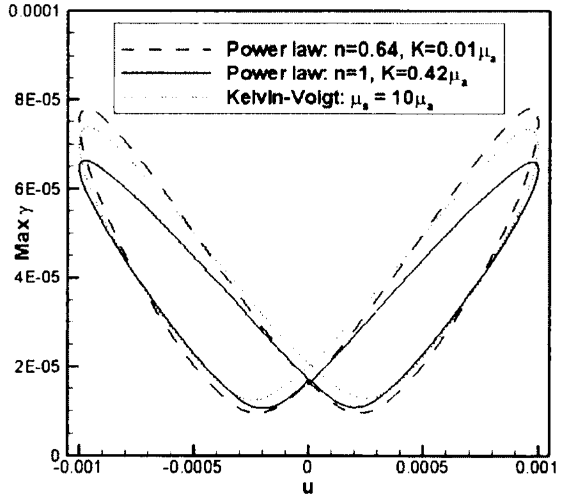

Figure 67. Maximum values of γ over one period of an oscillatory shear flow, for the capsules considered in Figure 66. The x-axis is the flow velocity $\mathbf{u}(t)$ at the top of the simulation domain, $y = H$.

which is clearly not sufficient to observe the sort of effects found by Puig-de-Morales-Marinkovic *et al.* and Fedosov *et al.*.

The results shown over the last several pages may be interpreted as a negative result: a method for simulating membrane viscosity using a power law fluid model does not produce substantially different results than the Kelvin-Voigt model in standard venues like shear or oscillatory shear flow. Yet a negative result here is also useful, in terms of understanding how Puig-de-Morales-Marinkovic *et al.*'s result impacts previous computational studies and analysis based on solid viscoelastic models. For a spherical capsule in the ubiquitous shear flow setting, the models are nearly equivalent for small deformations and are, at worst, qualitatively similar at larger deformations. As a result, it seems that the results of previous computational work with solid viscoelastic model are not significantly challenged by Puig-de-Morales-Marinkovic *et al.*'s finding. Further analysis will be necessary to determine whether this similarity between the power law and Kelvin-Voigt extends to biconcave capsules in shear flow; published data about the latter case does not yet appear to exist.

Similarly, Puig-de-Morales-Marinkovic *et al.* [48] question the meaning of exponential recovery models, like those used for micropipette aspiration [21] and optical tweezing [13], being based on the Kevlin-Voigt viscoelastic model. Happily, this concern is less relevant to the sort of data analysis developed by Diaz and coworkers [20] and performed in Chapters 3 and 4. In these computational studies, exponential curves were fitted over the entire recovery process and, as a result, are not susceptible to the artifactual interpretations resulting from fitting curves over intervals of arbitrary duration. Further, shape response and recovery in a fluid-structure interaction setting is not purely viscoelastic anyway and, consequently, the distinction between power law and exponential viscoelastic recovery is less relevant.

CHAPTER 6

CONCLUSIONS

Despite the significant attention that computational researchers have shown to red blood cells in recent years, substantial holes remain in the current understanding. Computational researchers focused on a deformable capsule's response to deformation, while experimentalists considered the shape recovery of red blood cells. This leads to a certain disconnect between the theories, with little clarity as to how a theory in one realm is applicable to the other. As a result, a computational study of shape recovery is of interest. Further, recent developments by experimentalists seem to have invalidated the popular Kelvin-Voigt viscoelastic model's applicability to the membrane viscosity of red blood cells. It has not been clear how the proposed power law model, from the domain of complex fluids, may be included in a computational model or how it compares to Kelvin-Voigt in typical simulation settings.

In order to begin addressing these topics, comprehensive two and three dimensional models for the fluid-structure interaction of a deformable capsule in an ambient flow have been presented. The model is centered around the immersed boundary method, using lattice Boltzmann and finite element methods for the fluid and structural components. When considered with respect to existing methods for deformation in shear flow, the model is demonstrated to be sufficiently accurate.

Building on the work of Diaz and colleagues [20, 19], exponential models are proposed for the response and recovery of circular and spherical capsules, in terms of the Taylor deformation parameter. These models generally fit the data from the simulations conducted very well. Considering the roles of the capillary number, bending stiffness, and fluid and membrane viscosity ratios separately, the differences between response and recovery become apparent, along with the differences between the two and three dimensional versions of the model. While the effects of these four parameters on the steady-state deformation of circular and spherical capsules are well known, these results demonstrate how these parameters influence the speed with which a capsule reaches a steady-state deformation or recovers the undeformed shape.

The recovery model is extended to two dimensional biconcave capsules, with ensembles of tumbling and tank-treading capsules being considered separately. For both equilibrium behaviours, a two-phase recovery process is observed, a phenomenon for which experiments may provide some biophysical basis. The first recovery phase centered on viscoelastic dissipation, and parallels nicely with models for the shape recovery of red blood cells from micropipette aspiration. On the other hand, the second recovery phase was found to contain the actual shape recovery and was consistent with results for circular capsules. This two-phase model helps to clarify how the capsule's undeformed biconcave shape influences the shape recovery process.

In simulations of three dimensional biconcave capsules, the roles of the capsule's reference shear deformation and spontaneous curvature were considered, as these aspects are not included in two dimensional models. Partial, but incomplete, shape recovery was observed for capsules with constant spontaneous curvature, whether the capsule had a uniform (stressed) or non-uniform (unstressed) reference shear deformation. On the other hand, tank-treading behaviour consistent with shape memory during recovery was displayed by capsules with a non-uniform reference shear deformation, but not with a uniform reference shear deformation. These admittedly limited results are consistent with theories that attribute the red blood cell's biconcave shape to the bending stiffness of the lipid bilayer and propose the non-uniform reference shear deformation of the cytoskeleton as the impetus for red blood cell shape memory.

Finally, the notion of using additional fluid viscosity to simulate the effects of membrane viscosity was tested for spherical capsules and Kelvin-Voigt viscoelasticity. The basic notion was validated, though the naive approach does not lead to a particularly useful computational model. Instead, the model is extended to the power law model proposed by Puig-de-Morales-Marinkovic *et al.*, whereby membrane viscosity is calculated on the capsule surface and distributed by the immersed boundary method to nearby fluid nodes as an additional fluid viscosity. This method is shown to approximate Kelvin-Voigt for the initial deformation in shear flow and the potentially non-Newtonian effects are considered.

Future work will be necessary to resolve the causes of numerical instability encountered and discussed in Chapter 4, and clarify the extent to which they have a physical basis. Subsequently, further investigations of the shape recovery of biconcave capsules will be carried out, to test whether the incomplete shape recovery observed here becomes complete. Additionally, future work will involve applying both Yazdani and Bagchi's viscoelasticity method and the power law model to biconcave capsules.

REFERENCES

[1] B. ALBERTS ET AL., *Molecular biology of the cell*, vol. 1, Garland Science, New York, NY, 2002.

[2] M. S. AMIN, Y. PARK, N. LUE, R. R. DASARI, K. BADIZADEGAN, M. S. FELD, AND G. POPESCU, *Microrheology of red blood cell membranes using dynamic scattering microscopy*, Opt. Express, 15 (2007), pp. 17001–17009.

[3] E. ANDERSON, Z. BAI, C. BISCHOF, S. BLACKFORD, J. DEMMEL, J. DONGARRA, J. DU CROZ, A. GREENBAUM, S. HAMMERLING, A. MCKENNEY, ET AL., *LAPACK Users' Guide*, vol. 9, SIAM, Philadelphia, PA, 1999.

[4] P. BAGCHI, *Multiscale modeling in large-scale simulation of blood flow in microcirculation*, in Multiscale Modeling of Particle Interactions: Applications in Biology and Nanotechnology, M. King and D. Gee, eds., Wiley, New York, NY, 2010.

[5] D. BARTHES-BIESEL, A. DIAZ, AND E. DHENIN, *Effect of constitutive laws for two-dimensional membranes on flow-induced capsule deformation*, J. Fluid Mech, 460 (2002), pp. 211–222.

[6] D. BARTHES-BIESEL AND H. SGAIER, *Role of membrane viscosity in the orientation and deformation of a spherical capsule suspended in shear flow*, J. Fluid Mech, 160 (1985), pp. 119–35.

[7] O. K. BASKURT AND H. J. MEISELMAN, *Determination of red blood cell shape recovery time constant in a couette system by the analysis of light reflectance and ektacytometry*, Biorheology, 33 (1996), pp. 489–503.

[8] K. CHANG AND W. OLBRICHT, *Experimental studies of the deformation and breakup of a synthetic capsule in steady and unsteady simple shear flow*, J. Fluid Mech, 250 (1993), pp. 609–633.

[9] J. CHARRIER, S. SHRIVASTAVA, AND R. WU, *Free and constrained inflation of elastic membranes in relation to thermoforming - non-axisymmetric problems*, J. Strain Anal. Eng. Des., 24 (1989), pp. 55–74.

[10] S. CHIEN, *Red cell deformability and its relevance to blood flow*, Annu. Rev. Physiol., 49 (1987), pp. 177–192.

[11] R. CHRISTENSEN, *A nonlinear theory of viscoelasticity for application to elastomers*, J. Appl. Mech., 47 (1980), pp. 762–768.

[12] J. R. CLAUSEN AND C. K. AIDUN, *Capsule dynamics and rheology in shear flow: Particle pressure and normal stress*, Phys. Fluids, 22 (2010), p. 123302.

[13] M. DAO, C. LIM, AND S. SURESH, *Mechanics of the human red blood cell deformed by optical tweezers*, J. Mech. Phys. Solids, 51 (2003), pp. 2259–2280.

[14] DASSAULT SYSTÉMES SIMULIA, *ABAQUS Theory Manual*, 2009.

[15] H. DEULING AND W. HELFRICH, *The curvature elasticity of fluid membranes: a catalogue of vesicle shapes*, J. Phys.-Paris, 37 (1976), pp. 1335–1345.

[16] ——, *Red blood cell shapes as explained on the basis of curvature elasticity*, Biophys. J., 16 (1976), pp. 861–868.

[17] M. O. DEVILLE AND T. B. GATSKI, *Mathematical modeling for complex fluids and flows*, Springer, New York, NY, 2012.

[18] D. D'HUMIÈRES, I. GINZBURG, M. KRAFCZYK, P. LALLEMAND, AND L.-S. LUO, *Multiple-relaxation-time lattice Boltzmann models in three dimensions*, Phil. Trans. R. Soc. A, 360 (2002), pp. 437–451.

[19] A. DIAZ, D. BARTHÈS-BIESEL, AND N. PELEKASIS, *Effect of membrane viscosity on the dynamic response of an axisymmetric capsule*, Phys. Fluids, 13 (2001), pp. 3835–3838.

[20] A. DIAZ, N. PELEKASIS, AND D. BARTHES-BIESEL, *Transient response of a capsule subjected to varying flow conditions: Effect of internal fluid viscosity and membrane elasticity*, Phys. Fluids, 12 (2000), pp. 948–957.

[21] E. EVANS AND R. HOCHMUTH, *Membrane viscoelasticity*, Biophys. J., 16 (1976), pp. 1–11.

[22] E. A. EVANS, *Structure and deformation properties of red blood cells: Concepts and quantitative methods*, Meth. Enzymol., 173 (1989), pp. 3–35.

[23] E. A. Evans and R. Skalak, *Mechanics and thermodynamics of biomembranes*, CRC, Boca Raton, FL, 1980.

[24] D. A. Fedosov, B. Caswell, and G. E. Karniadakis, *A multiscale red blood cell model with accurate mechanics, rheology, and dynamics*, Biophys. J., 98 (2010), pp. 2215–2225.

[25] T. M. Fischer, *Shape memory of human red blood cells*, Biophys. J., 86 (2004), pp. 3304–3313.

[26] R. V. Garimella and B. K. Swartz, *Curvature estimation for unstructured triangulations of surfaces*, Tech. Report Tech. Rep. LA-UR-03-8240, Los Alamos National Laboratory, 2003.

[27] W. Helfrich, *Elastic properties of lipid bilayers: theory and possible experiments*, Z. Naturforsch. C Bio. Sci., 28 (1973), pp. 693–703.

[28] R. Hochmuth, P. Worthy, and E. Evans, *Red cell extensional recovery and the determination of membrane viscosity*, Biophys. J., 26 (1979), pp. 101–114.

[29] G. Hou, J. Wang, and A. Layton, *Numerical methods for fluid–structure interactiona review*, Commun. Comput. Phys., 12 (2012), pp. 337–377.

[30] S. R. Keller and R. Skalak, *Motion of a tank-treading ellipsoidal particle in a shear flow*, J. Fluid Mech., 120 (1982), pp. 27–47.

[31] P. Lallemand and L.-S. Luo, *Theory of the lattice Boltzmann method: Dispersion, dissipation, isotropy, Galilean invariance, and stability*, Phys. Rev. E, 61 (2000), p. 6546.

[32] ——, *Theory of the lattice Boltzmann method: Acoustic and thermal properties in two and three dimensions*, Phys. Rev. E, 68 (2003), p. 036706.

[33] P. Lallemand, L.-S. Luo, and Y. Peng, *A lattice Boltzmann front-tracking method for interface dynamics with surface tension in two dimensions*, J. Comput. Phys, 226 (2007), pp. 1367–1384.

[34] D. V. Le, *Effect of bending stiffness on the deformation of liquid capsules enclosed by thin shells in shear flow*, Phys. Rev. E, 82 (2010), p. 016318.

[35] H. LI, H. YI, X. SHAN, AND H. FANG, *Shape changes and motion of a vesicle in a fluid using a lattice Boltzmann model*, Europhys. Lett., 81 (2008), p. 54002.

[36] X. LI AND K. SARKAR, *Front tracking simulation of deformation and buckling instability of a liquid capsule enclosed by an elastic membrane*, J. Comput. Phys, 227 (2008), pp. 4998–5018.

[37] M. MEYER, M. DESBRUN, P. SCHRÖDER, AND A. H. BARR, *Discrete differential-geometry operators for triangulated 2-manifolds*, in Visualization and Mathematics III, Springer, 2003, pp. 35–57.

[38] N. MOHANDAS AND E. EVANS, *Mechanical properties of the red cell membrane in relation to molecular structure and genetic defects*, Annu. Rev. Biophys. Biomol. Struct., 23 (1994), pp. 787–818.

[39] N. NDRI, W. SHYY, AND R. TRAN-SON-TAY, *Computational modeling of cell adhesion and movement using a continuum-kinetics approach*, Biophys. J., 85 (2003), pp. 2273–2286.

[40] H. NOGUCHI AND G. GOMPPER, *Dynamics of fluid vesicles in shear flow: Effect of membrane viscosity and thermal fluctuations*, Phys. Rev. E, 72 (2005), p. 011901.

[41] Z.-C. OU-YANG AND W. HELFRICH, *Bending energy of vesicle membranes: General expressions for the first, second, and third variation of the shape energy and applications to spheres and cylinders*, Phys. Rev. A, 39 (1989), p. 5280.

[42] Y. PENG AND L.-S. LUO, *A comparative study of immersed-boundary and interpolated bounce-back methods in LBE*, Progr. Comput. Fluid Dynam. Int. J., 8 (2008), pp. 156–167.

[43] C. S. PESKIN, *The immersed boundary method*, Acta Numer., 11 (2002), pp. 479–517.

[44] U. PINKALL AND K. POLTHIER, *Computing discrete minimal surfaces and their conjugates*, Exper. Math., 2 (1993), pp. 15–36.

[45] C. POZRIKIDIS, *Effect of membrane bending stiffness on the deformation of capsules in simple shear flow*, J. Fluid Mech., 440 (2001), pp. 269–291.

[46] ——, *Numerical simulation of the flow-induced deformation of red blood cells*, Ann. Biomed. Eng., 31 (2003), pp. 1194–1205.

[47] ——, *Resting shape and spontaneous membrane curvature of red blood cells*, Math Med. Biol., 22 (2005), pp. 34–52.

[48] M. Puig-de Morales-Marinkovic, K. T. Turner, J. P. Butler, J. J. Fredberg, and S. Suresh, *Viscoelasticity of the human red blood cell*, Am. J. Physiol. Cell Physiol., 293 (2007), pp. C597–C605.

[49] S. Ramanujan and C. Pozrikidis, *Deformation of liquid capsules enclosed by elastic membranes in simple shear flow: large deformations and the effect of fluid viscosities*, J. Fluid Mech., 361 (1998), pp. 117–143.

[50] M. Reuter, S. Biasotti, D. Giorgi, G. Patanè, and M. Spagnuolo, *Discrete laplace-beltrami operators for shape analysis and segmentation*, Comput. Gr., 33 (2009), pp. 381-390.

[51] T. Secomb, N. Ozkaya, R. Skalak, and J. Gross, *Flow of axisymmetric red blood cells in narrow capillaries*, J. Fluid Mech., 163 (1986), pp. 405–23.

[52] S. Shrivastava and J. Tang, *Large deformation finite element analysis of non-linear viscoelastic membranes with reference to thermoforming*, J. Strain Anal. Eng. Des., 28 (1993), pp. 31–51.

[53] R. Skalak, A. Tozeren, R. Zarda, and S. Chien, *Strain energy function of red blood cell membranes*, Biophys. J., 13 (1973), pp. 245–264.

[54] J. Skotheim and T. Secomb, *Red blood cells and other nonspherical capsules in shear flow: oscillatory dynamics and the tank-treading-to-tumbling transition*, Phys. Rev. Lett., 98 (2007), p. 078301.

[55] Y. Sui, *A Numerical Study on the Deformation of Liquid-Filled Capsules with Elastic Membranes in Simple Shear Flow*, PhD thesis, National University of Singapore, 2008.

[56] Y. Sui, Y. Chew, P. Roy, X. Chen, and H. Low, *Transient deformation of elastic capsules in shear flow: Effect of membrane bending stiffness*, Phys. Rev. E, 75 (2007), p. 066301.

[57] Y. Sui, H. Low, Y. Chew, and P. Roy, *A front-tracking lattice Boltzmann method to study flow-induced deformation of three-dimensional capsules*, Comput. Fluids, 39 (2010), pp. 499–511.

[58] S. Sutera, E. Mueller, and G. Zahalak, *Extensional recovery of an intact erythrocyte from a tank-treading motion.*, J. Biomech. Eng., 112 (1990), pp. 250–256.

[59] K. Svoboda, C. Schmidt, D. Branton, and S. Block, *Conformation and elasticity of the isolated red blood cell membrane skeleton*, Biophys. J., 63 (1992), pp. 784–793.

[60] G. Tryggvason, B. Bunner, A. Esmaeeli, D. Juric, N. Al-Rawahi, W. Tauber, J. Han, S. Nas, and Y.-J. Jan, *A front-tracking method for the computations of multiphase flow*, J. Comput. Phys, 169 (2001), pp. 708–759.

[61] S. Usami, S. Chien, P. M. Scholtz, and J. F. Bertles, *Effect of deoxygenation on blood rheology in sickle cell disease*, Microvasc. Res., 9 (1975), pp. 324–334.

[62] R. Wang, H. Ding, M. Mir, K. Tangella, and G. Popescu, *Effective 3d viscoelasticity of red blood cells measured by diffraction phase microscopy*, Biomed. Opt. Express, 2 (2011), p. 485.

[63] A. Yazdani and P. Bagchi, *Influence of membrane viscosity on capsule dynamics in shear flow*, J. Fluid Mech., 718 (2013), pp. 569–595.

[64] A. Z. Yazdani and P. Bagchi, *Phase diagram and breathing dynamics of a single red blood cell and a biconcave capsule in dilute shear flow*, Phys. Rev. E, 84 (2011), p. 026314.

[65] A. Z. K. Yazdani, *Dynamics of Erythrocytes, Vesicles and Capsules in Shear Flow: The Role of Membrane Bending Stiffness and Membrane Viscosity*, PhD thesis, Rutgers, The State University of New Jersey, 2012.

[66] Y. Z. Yoon, J. Kotar, A. T. Brown, and P. Cicuta, *Red blood cell dynamics: from spontaneous fluctuations to non-linear response*, Soft Matter, 7 (2011), pp. 2042–2051.

[67] Y.-Z. YOON, J. KOTAR, G. YOON, AND P. CICUTA, *The nonlinear mechanical response of the red blood cell*, Phys. Biol., 5 (2008), p. 036007.

[68] J. ZHANG, P. C. JOHNSON, AND A. S. POPEL, *An immersed boundary lattice Boltzmann approach to simulate deformable liquid capsules and its application to microscopic blood flows*, Phys. Biol., 4 (2007), p. 285.

[69] ——, *Red blood cell aggregation and dissociation in shear flows simulated by lattice Boltzmann method*, J. Biomech., 41 (2008), pp. 47–55.

[70] M. ZHAO AND P. BAGCHI, *Dynamics of microcapsules in oscillating shear flow*, Phys. Fluids, 23 (2011), pp. 111901–111901.

VITA

John Gounley
Department of Computational and Applied Mathematics
Old Dominion University
Norfolk, VA 23529

EDUCATION

Ph.D. Computational and Applied Mathematics, Old Dominion University, Norfolk, VA. (2014)

M.S. Computational and Applied Mathematics, Old Dominion University, Norfolk, VA. (2011)

Certificate in Modeling and Simulation, Old Dominion University, Norfolk, VA. (2011)

B.A. Liberal Arts, Thomas Aquinas College, Santa Paula, CA. (2008)

PUBLICATIONS

J. Gounley and Y. Peng, *Shape recovery of elastic capsules from shear flow induced deformation*, Communications in Computations Physics, 2014. In press.

J. Gounley and Y. Peng, *Response and recovery times of elastic and viscoelastic capsules in shear flow.* In revision.

J. Gounley and Y. Peng, *Computational modeling of membrane viscosity of red blood cells.* In revision.

Typeset using LaTeX.